

Luleå Tekniska Universitet

Master Thesis, Space Engineering, Specialisation Spacecraft and Instrumentation
P7004R

The Meridian Imaging Svalbard Spectrograph 2: Enhancing Auroral Tracking Capacities

Author:

Nicolas Martinez nicmar-9@student.ltu.se

Supervisor:

Fred Sigernes FredS@UNIS.no

Examiner:

Stefanus Schröder stefanus.schroder@ltu.se



Department of Computer Science, Electrical and Space Engineering of LTU
Department of Arctic Geophysics of UNIS

December 9, 2024

Abstract

The first Meridian Imaging Svalbard Spectrograph (MISS 1) prototype was developed at the University Centre in Svalbard (UNIS) in 2018-2019 and has been operational at the Kjell Henriksen Observatory (KHO) since. It was designed to track auroral emissions along the geomagnetic meridian using a tunable air-spaced transmission grating and prism (TGRISM). The need for a hyperspectral imager with enhanced capacities using a similar TGRISM dispersing element, based on the existing MISS 1 design, led to the development of MISS 2.

The MISS project aims to develop an alternative to the Meridian Scanning Photometer (MSP), accomplishing the same task with improved spectral capabilities and without moving pieces.

The practical aspect of this project focused on two main objectives. Firstly, developing software which enables remote control of the spectrograph and supports continuous data-acquisition. Secondly, it encompasses the assembly, adjustment and calibration of all components to create a fully functional instrument.

The aim of this thesis is to document and present the design process of a fully operational MISS instrument to ensure its fabrication, further development and future use.

Throughout this project, the instrument was successfully assembled and calibrated. The software was effectively developed to allow its continuous remote operation. The instrument is fully ready for testing at KHO, which is planned for winter 2024/25.

Sammanfattning

Den första MISS-prototypen utvecklades 2018-2019 vid UNIS och har varit i drift på KHO sedan dess. Prototypen är utformad för att spåra norrsken längs den geomagnetiska meridianen och använder ett justerbart transmissionsgitter med luftgap samt prisma-element (TGRISM). Behovet av en hyperspektral kamera med förbättrade funktioner, baserad på den MISS 1-designen, ledde till utvecklingen av MISS 2.

MISS-projektet syftar till att utveckla ett alternativ till Meridian Scanning Photometer (MSP), med samma funktionalitet men förbättrade spektrala förmågor och utan rörliga delar.

Det praktiska arbetet i detta projekt har fokuserat på två huvudsakliga mål. För det första att utveckla programvara som möjliggör fjärrstyrning av spektrografen och kontinuerlig dataregistrering. För det andra omfattade arbetet montering, justering och kalibrering av alla komponenter för att skapa ett fullt fungerande instrument.

Målet med denna masteruppsats är att dokumentera och presentera designprocessen för ett fullt fungerande MISS-instrument. Genom en noggrann dokumentation av hela processen syftar uppsatsen till att säkerställa dess tillverkning, vidareutveckling och framtida användning.

Instrumentet har framgångsrikt monterats och kalibrerats. Programvaran har utvecklats för att möjliggöra kontinuerlig fjärrstyrd drift av instrumentet. Instrumentet är nu fullt redo för testning vid KHO, som planeras äga rum vintern 2024/25.

Acknowledgement

I would like to thank Fred Sigernes for giving me the opportunity to contribute to the MISS project. His expert help and guidance have been invaluable throughout my entire participation, including his thorough review of this document. I am also very grateful to Mikko Syrjäsuo, whose insights and recommendations were instrumental in the design of the instrument's software and important stages of its assembly. Lastly, special thanks to my colleagues at Funken Lodge, who helped make my time in the world's northernmost village a far less solitary experience than one might expect.

Table of Contents

Acronyms	vii
1 Introduction	1
1.1 Background	1
1.2 MISS 1	2
1.3 From MISS 1 to MISS 2	4
1.4 Project Objectives	5
2 Theory of Optical Imaging	6
2.1 Fundamentals of Spectroscopy	6
2.2 Geometrical Optics	7
2.2.1 Refraction and Snell-Descartes Law	7
2.2.2 Wavelength Dependence of the Refractive Index	9
2.3 Refraction Prism	11
2.3.1 Optimal incident angle	11
2.3.2 Dispersion angle	12
2.4 Wave Optics	12
2.4.1 Wave Equation	12
2.4.2 Interference and Diffraction	14
2.4.3 Overlapping Orders and Non-Linear Dispersion	21
2.5 Diffraction Grating	21
2.5.1 Grating Types and Characteristics	21
2.5.2 Grating Equation	23
2.5.3 Blazed Wavelength	23
2.5.4 Grating Efficiency for MISS	24
2.6 Dispersive Element of MISS	25
2.6.1 GRISM Equation	25
2.6.2 Tilt Angle and TGRISM Equation	26
3 Instrument Design	30
3.1 Optical Design of MISS	30
3.1.1 All-sky Lens	31
3.1.2 Entrance Slit	31
3.1.3 Field Lens	32
3.1.4 Collimating Lens	32
3.1.5 Dispersive Element	33

3.1.6	Focusing Lens	34
3.1.7	Sensor	34
3.2	Spectral Resolution	35
3.2.1	Expression of the Passband	35
3.2.2	Application for MISS 2	38
3.3	Spatial Resolution	39
3.3.1	Spatial Resolution of a Hyperspectral Imager	39
3.3.2	Application for MISS 2	40
3.4	Angular Resolution	43
3.5	Slit Length and Width Magnification	44
3.6	Transmission Efficiency	44
4	Components and Assembly	47
4.1	Optical Component Specifications	48
4.1.1	Transmitting Grating	48
4.1.2	Littrow Prism	48
4.1.3	Lenses	49
4.1.4	Sensor Specifications	51
4.1.5	Front Lens Protection Shutter Specifications	51
4.2	Mechanical Structure	52
4.2.1	Assembly Protocol	53
4.2.2	Front-Lens Mechanical Shutter Integration	54
4.2.3	Fine-Tuning Stages	55
4.3	Imager Fully Assembled	58
5	Software Design	59
5.1	MISS 2.0: Purpose and Functionalities	59
5.2	Configuration Parameters	60
5.3	Automated Aurora Tracking	61
5.3.1	MISS Controller (Main script)	61
5.3.2	Atik Controller	62
5.3.3	SunShield Controller	63
5.3.4	Darkness Condition	63
5.4	Real-Time Data Processing	64
5.4.1	Summary of the Program Workflow	64
5.4.2	Real-Time Data Processor (Main Script)	65
5.4.3	Average Spectrogram Maker	66
5.4.4	RGB Column Maker	67

5.4.5	Keogram Maker	68
5.4.6	Spectrogram Processor	69
5.4.7	KHO Website Data Feed	70
5.4.8	Routine Eraser	71
5.5	Real-Time Website Data Output	72
5.6	Past Keogram Maker	73
5.6.1	Simulated Keogram without Analysis Plots	73
5.6.2	Simulated Keogram with Analysis Plots	73
5.6.3	Diagram of the Workflow of Past Keogram Maker	74
6	Calibration	75
6.1	Spectral Calibration	75
6.1.1	Calibration Protocol	76
6.1.2	Results	76
6.1.3	Wavelength Mapping	77
6.1.4	Spectral Fitting Coefficients for MISS 2.0	78
6.1.5	Estimation of the FWHM	78
6.1.6	Spectral Calibration and Estimated FWHM for MISS 1	79
6.2	Radiometric Calibration	80
6.2.1	Calibration Protocol	80
6.2.2	Results	81
6.2.3	Radiance mapping	84
6.2.4	Calibration Coefficient K Fitting Coefficients	84
6.2.5	Linearity Test	84
6.2.6	Radiometric calibration and Linearity Test for MISS 1	86
7	Results	88
8	Conclusion	90
	Appendix A: Component List for MISS 2 Spectrograph	
	Appendix B: Views of MISS 2 Spectrograph	
	Appendix C: Calibration Certificate for Keo Alcor-RC LBS s/n 10113	

Acronyms

ADC Analogue to Digital Converter 51

AVIRIS Airborne Visible/Infrared Imaging Spectrometer 1

CAD Computer-Aided Design 52

CCD Charge-Coupled Device 6, 26, 34, 40, 44, 46, 51, 54, 56

FOV Field Of View 3, 31, 32, 40, 42, 49, 58, 60, 67, 69, 76, 77, 80, 82

FWHM Full-Width Half Maximum vi, 36, 39, 78, 79

GRISM Grating and Prism iv, 25, 26, 28, 36, 52–54

KHO Kjell Henriksen Observatory i, ii, vi, 2–4, 47, 59, 61, 63–65, 70, 88, 89

LEO Low Earth Orbit 2

Massimal Mapping of Algae and Seagrass Using Spectral Imaging and MACHine Learning 2

MISS Meridian Imaging Svalbard Spectrograph i, ii, iv–vi, , 2–7, 11, 12, 22, 24–36, 38–45, 47, 52–55, 58–66, 68, 72, 73, 75, 76, 78–80, 83, 86, 88–90

MLAT Magnetic Latitude 4

MSP Meridian Scanning Photometer i, ii, 2–4, 88, 89

NASA National Aeronautics and Space Administration 1

OPL Optical Path Length 7, 8

OTA Optical Tube Assembly 52, 53

SDK Software Development Kit 62

SNR Signal-to-noise ratio 31, 34

TGRISM Tunable air-spaced Transmission Grating and Prism i, ii, iv, 4, 6, 25–30, 33, 34, 44, 48

UNIS University Centre In Svalbard i, ii, 2, 4, 5, 47, 59, 60, 75, 80, 90

VIS Visible Spectrum 6, 11, 24, 26, 29, 48, 57

1 Introduction

1.1 Background

Imaging spectroscopy, often referred to as *hyperspectral imaging*, has its roots in early spectroscopic measurements, beginning with Anders J. Ångström's groundbreaking work in the 19th century. His identification of auroral emission lines laid the foundation for modern techniques like imaging spectroscopy. His study of the auroral spectrum, using a diffraction grating spectrograph allowed for the first determination of the bright green auroral line of emission (5567 Å, as presented in *Recherches sur le Spectre Solaire*[1], 1868). Eventually fixed at 5577 Å it was attributed to a radiative transition of atomic oxygen ($O(^1S_0) \rightarrow O(^1D_2) + h\nu$) over 50 years later.[2]

Subsequently, other main observable auroral lines in the visible spectrum were identified. This includes the auroral reds (6300 Å ($O(^1D_2) \rightarrow O(^3P_2) + h\nu$) and 6364 Å ($O(^1D_2) \rightarrow O(^3P_1) + h\nu$), resulting from two closely related radiative transitions of atomic oxygen in the upper thermosphere ([3] Chamberlain (1958); [4] Vallance Jones et al. (1974)).

Some of the main lines in the subtle auroral blue-violet range, between 4278 Å and 4340 Å, were also identified. These lines result from a wider variety of transitions involving atomic oxygen, molecular nitrogen (N_2), and molecular nitrogen ions (N_2^+).[5, 6] Other chemical compounds are also involved, via complex processes that are not yet fully understood.

Using the acquired knowledge of the nature and origin of the different types of auroral emissions and eventually, of the grandly complex physical processes and mechanisms that lead to the manifestation of aurora, the development of imaging spectroscopy represented a significant advancement to the study of aurora. Initiated in the late 1970s by the NASA Jet Propulsion Laboratory, it eventually led to the launch in 1993 of AVIRIS (Airborne Visible/Infrared Imaging Spectrometer), the first full range imaging spectrometer, which was used for Earth monitoring [7], which opened the way to a revolutionary imaging tool. It offered a revolutionary tool to study the northern lights by providing not only a convenient way of tracking them spatially over time, but also a whole spectrum of emission of the object, with a spectrum consisting of hundreds of bands provided per spatial unit.

Images collected by an imaging spectrograph present spectral data as a function of space, making them a three-dimensional dataset. Hence the widely used term *datacube* to qualify such a multi-layered image. This method of imaging has gained a wide range of applications, especially in machine learning applications. These

include agricultural and environmental monitoring (crop monitoring [8], forest health [9], Arctic sea-ice monitoring [10], etc.), detection and mapping of resources (oil and gas prospecting [11], mineralogical mapping [12, 13]), biological imaging [14], marine vegetation monitoring [15, 16] and even in defense (e.g. monitoring borders, identifying chemical substances [17]).

Yet, such an imaging method applied on an object in two spatial dimensions and one spectral dimension (*snapshot hyperspectral imaging*) has limitations which make it difficult to apply in certain specific applications. For instance, high-resolution imaging of large areas, such as a rainforest [18] or the entire stretched coastline of Norway (e.g., the [Massimal](#) project [19]), requires the use of instruments mounted on aircraft or satellites in Low Earth Orbit (LEO). The spatial resolution must align with the desired image quality, and the temporal resolution must meet the needs of the specific application (for example, weather monitoring may demand both high spatial and temporal resolutions). In such cases, push-broom imaging is the most effective technique to ensure comprehensive, high-resolution imaging of the target region. Instead of collecting two space-dimensional data, a push-broom imager captures mono-dimensional images of the object. Sets of images can then be computed into one single, coherent image considering a significant set of parameters such as the altitude and velocity of the aircraft or satellite and the time at which each image was captured. Showing the dataset (mono-dimensional images) as a function of time, in this case with all required corrections, allows a direct visualisation of the zone of interest, with the limitations induced by the swath width (i.e. width of the area covered by the aircraft or satellite in one pass). The result is a datacube of similar nature as previously described.

1.2 MISS 1

The Meridian Imaging Svalbard Spectroscope version 1 (MISS 1) [20] is an application prototype of push-broom imaging with the specific task of monitoring and tracking auroral activity along the magnetic meridian line, designed, developed, tested and operational at the Kjell Henriksen Observatory (KHO) near Longyearbyen on Svalbard and operated by the University Centre in Svalbard (UNIS).

It was developed as a potential candidate to replace the Meridian-Scanning Photometer (MSP) [21], which is currently serving at KHO for tracking auroral activity along the magnetic meridian. It is a photometer which uses four fixed detectors that measure

light emission at 4 auroral emission lines: 6300 Å, 4278 Å, 5577 Å and 8446 Å with the help of narrow-band optical filters. Its complexity and high maintenance requirements highlight the need for a more reliable alternative, whereas the older technology it uses calls for a modernisation of the technology used. As of 2024, both MISS 1 and the MSP are operational at KHO, fulfilling the same task, to allow extensive comparison of respective data as well as instrument redundancy.

As is the case for the MSP, the focus of MISS 1 is on a thin section of the entire geomagnetic meridian portion of the sky and as such, it is to be static relatively to the surface of the Earth and monitor that specific portion of the sky. However, it has to be considered that it completes a full revolution every 24 hours relatively to the Sun, which implies that it can track and monitor auroral activity within the time limits of astronomical twilight. And, especially considering its favoured location is on latitudes greater than that of the geographic polar circle (66°33'N), that tracking is made possible without any interruption during the entire polar night, sharing in that regard a great similarity with a satellite in orbit over the region of interest.

Similarly to a satellite, a land-based instrument of observation of the sky is limited by its swath width, which in the case of an all-sky observation instrument such as the MISS 1 prototype, is bound to the limits of the horizon, having a field of view (FOV) of 180°, from geomagnetic South to geomagnetic North and importantly, the distance between the object (the aurora) and the surface of the Earth: the higher the altitude of the auroral event, the further away it will be observable from the ground. In other terms, in this configuration our land-based push-broom imager, and by extension, the Observatory in which it is located, is the 'satellite' and the aurora is the object being monitored using the Earth's rotation around its own axis in lieu of an actual satellite's orbit around the Earth. A rough estimate of the lower and upper limits of the observability of northern lights can easily be obtained knowing the range of altitudes at which they may occur (between about 100 km and 400 km) using the Pythagorean theorem: over 1000 km for the low altitude northern lights and over 2000 km for the high altitude northern lights, which when taken along a magnetic North-South axis represent a range of roughly 12°-20° of latitude.

Arguably, these distances should not only be considered rough estimates. They are also absolute upper limits which are evidently impossible to get close due to the combined effects of atmospheric conditions (light scattering, meteorological conditions, etc.), obstruction of the line of horizon or simply a too low elevation angle relatively to the observer. The nightside auroral oval is usually centered around 67°-70° magnetic latitudes (MLAT) or higher. For instance, during the daytime within the polar night

period, monitoring auroral activity from a location within this range (or less than 10-12 degrees higher) is particularly pertinent.

And that is true even in low auroral activity conditions. In that regard, **KHO** located at about 78°N 18°E, i.e. between 74° and 75° (**MLAT**), is well within range for such a task. Importantly, it also presents the advantage of being located at a very high geographic latitude where polar night lasts 10 weeks, allowing the constant tracking of both *dayside* and *nightside* auroral activity during this entire period, which makes it an ideal location for uninterrupted monitoring. Conversely, an observatory located well within the centre of the auroral oval but at a significantly lower geographical latitude, would on the other hand not offer such an uninterrupted monitoring.

1.3 From **MISS 1** to **MISS 2**

Built during the years 2019-2020, **MISS 1** has been collecting promising data, tracking auroral activity since it became operational at the Kjell Henriksen Observatory, where it is active among the 31 active optical and 16 radio instruments, as of winter 2023-2024.[22]

Its straight-forward design, using optics and a tunable air spaced transmission grating and prism (**TGRISM**) dispersing element which do not require any moving parts or mirror allows for the collection of data of good quality and with limited optical aberrations. It also fully qualifies it for operations in an unmanned observatory such as **KHO**, as it is less likely to require maintenance and can easily be taken back to **UNIS**, for example for routine check or calibration in an optical laboratory. The implications are that **MISS 2** can be merely regarded as an improvement using a very similar, sturdier hardware with the same optical configuration, based off a promising first prototype, with an improved, rethought software.

The development of the **MISS** prototypes aims to provide a reliable and consistent replacement for the **MSP**, offering superior imaging capacities. **MISS 1** is expected to fulfill this role effectively and replace the **MSP** altogether at **KHO**, whereas **MISS 2** will adapt this technology and be operational at the Ny-Ålesund Research Station, allowing both instruments to operate in close geographical proximity. The synergy between these two instruments has the potential to improve data quality by providing spatial correlation and provide more comprehensive monitoring of auroral activity over Svalbard, while also ensuring necessary instrument redundancy once the **MSP** is retired from operation.

1.4 Project Objectives

The main objective of the project I undertook was to document the hardware and software of [MISS 2](#), in order to provide an exhaustive description of the instrument, along with all the necessary tools for its fabrication. The importance of such a task can be regarded as not only a way to ensure that the instrument is made available for replication by other research teams, but also to give a verifiable scientific validity to the data collected by the [MISS](#) prototypes. It shall therefore be as extensive as expected for such a level of rigor and backed with relevant theory whenever necessary.

Notable is also my involvement in the [MISS 2](#) development project itself, taking part in the stages of assembly, tuning, and calibration of the new prototype at [UNIS](#), as well as the design of a full software suite, eventually made available in a dedicated repository on the official *Github* account of the University Centre in Svalbard (*UNISvalbard*). That involvement proved instrumental in getting a deeper understanding of all factors involved during all key stages of the development of the instrument, which helped greatly with the main objective at hand. It also allowed me to get the opportunity to formally introduce the [MISS](#) instruments during the *21st EISCAT Symposium 2024 and 48th Annual European Meeting on Atmospheric Studies by Optical Methods* in Tromsø as a novel instrumentation for the study of northern lights.

This thesis aims at first introducing all theoretical notions necessary for the description of all optical and mathematical concepts involved in the project, before dealing with the full description of the hardware and the software of [MISS 2](#) and discussing the potential of [MISS](#) as a new key tool for auroral emission tracking. Lecture notes about *Basic hyperspectral imaging* by F. Sigernes [23] represents an important source for this thesis, from which some essential concepts and mathematical calculations derive. Another one is *Fundamentals of Photonics* by Saleeh B. and Teich C. [24], which provides a comprehensive foundation in optics (and photonics) that is helpful for a better understanding of the theories applied in this project.

Own figures and photographs unless otherwise stated.

2 Theory of Optical Imaging

The **MISS** spectrographs use a tunable air spaced transmission grating and prism (**TGRISM**) as their refractive and diffractive element. This choice of dispersing element is made to keep the light parallel to the straight-through optical axis. As such, the light reaching the **CCD** (Charge-Coupled Device) sensor has not been reflected and its overall dispersion has been balanced spatially by the coupled prism-grating. Its path can therefore be considered quasi-linear, with no horizontal (axis of the entrance slit) deviation and minimal vertical deviation, which implies limited aberrations and intensity loss.

The purpose of this Chapter is to explicate the main optical principles at play in a spectrograph such as the **MISS** spectrographs. It will first approach the fundamental notions of diffraction by transmission grating and refraction of light by a prism, in order to then present the theoretical characteristics of the **MISS** spectrographs in general and of **MISS 2** in particular. Whenever a numerical application is made, characteristic values for **MISS 2** are used, which is emphasised with light blue markings next to each such occurrence.

2.1 Fundamentals of Spectroscopy

Spectroscopy is a method of imaging using the properties of light interacting with matter to extract information about its composition. More specifically, a grating surface is used to diffract the light of the source, efficiently separating the incident light into the wavelengths of which it is composed. In the case of the **MISS** spectrographs, a transmission grating is used, which means that the incident light is diffracted as it is transmitted through the grating surface. A prism is also used ahead of the grating surface, its refracting properties are instrumental in offering a more coherent dispersion of light prior to its passage through the transmission grating. This allows clearer separation of different wavelengths and emphasizes higher wavelengths. The refraction effects of a prism on light are non-linear and described by Cauchy's equation, with a refracted angle that can be approximated as a function of $1/\lambda^2$, whereas the diffraction angle of light by a grating surface is best approximated as an inverse sinusoidal equation. In the case of the **MISS** spectrographs, the entire visible spectrum (**VIS**, about 400 nm - 700 nm) is of interest, with a particular need for a clear separation of the colours in the blue-violet range, which contains a significant amount of auroral emission lines.

For the study of the emission spectrum of a light source, the end-product by such a spectrometer is an image of the full visible spectrum of the incoming light, i.e.

spectrogram, which can be captured by its sensor, saved and analysed.

2.2 Geometrical Optics

Geometrical optics is a field of optics that allows the simplified representation of the propagation of light through an optical system by representing light as rays. Connecting their originating point directly (*Source S*) and their destination (The observer's eye, a screen, a sensor...) via optical components that are significantly greater in dimension than the wavelength of the light in question. As such, it can be used to describe the setup of a spectrograph easily. In this section, all tools necessary to interpret and design an optical diagram for a spectrograph in general and MISS 2 in particular will be presented.

2.2.1 Refraction and Snell-Descartes Law

According to Fermat's principle, *light travels from a point A to a point B using the path of least time.*[24] True, albeit trivial in the case of light propagating in a vacuum, which indeed can be represented as a straight ray connecting A to B, that principle becomes essential when it comes to determining the optical path of a beam of light as it is *reflected* by a mirror or *refracted/entirely reflected* at the interface between two media.

- **Optical path length**

A ray of light propagating between A and B through a medium other than a vacuum will have its apparent speed reduced from c to $v = c/n$, with $n(\geq 1)$, the refractive index of the medium, which is an important parameter characterising a medium. It is the necessary coefficient which accounts for that speed variation, used in the expression of the optical path length (OPL), which represents the distance light would travel in a vacuum in the same amount of time:

$$OPL = n \cdot AB \tag{2.1}$$

- **Propagation between two media**

Let us consider a ray propagating from $A(x_A, y_A)$ located in medium 1 (n_1), to $B(x_B, y_B)$ located in medium 2 (n_2) via $P(x, 0)$, the point at the interface between medium 1 and medium 2 at $y = 0$ as shown in [Figure 2.1](#). The expression for the OPL as a function of the x-component of P becomes:

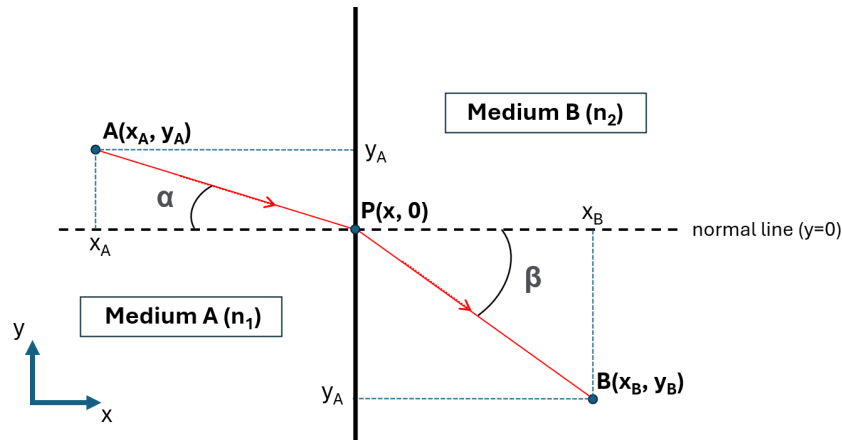


Figure 2.1: Propagation between two media from A to B via P

$$OPL(x) = n_1 \sqrt{(x - x_A)^2 + (y_A)^2} + n_2 \sqrt{(x_B - x)^2 + (y_B)^2}$$

The expression of the OPL follows Fermat's Principle, which means that we must have $\frac{d}{dx}(OPL) = 0$:

$$\begin{aligned} \frac{d}{dx}(OPL) &= \frac{d}{dx} \left(n_1 \sqrt{(x - x_A)^2 + (y_A)^2} + n_2 \sqrt{(x_B - x)^2 + (y_B)^2} \right) = 0 \\ \Rightarrow \frac{d}{dx} \left(n_1 \sqrt{(x - x_A)^2 + (y_A)^2} \right) &= \frac{d}{dx} \left(n_2 \sqrt{(x_B - x)^2 + (y_B)^2} \right) \\ \Rightarrow n_1 \frac{x - x_A}{\sqrt{(x - x_A)^2 + (y_A)^2}} &= n_2 \frac{x - x_B}{\sqrt{(x_B - x)^2 + (y_B)^2}} \end{aligned}$$

Identifying the ratio $\frac{\text{opposite}}{\text{hypotenuse}} = \sin \theta$, we get:

$$n_1 \cdot \sin \alpha = n_2 \cdot \sin \beta \quad (\text{Snell-Descartes Law})$$

The Snell-Descartes law is the direct application of Fermat's principle and indicates what the angle of refraction between two contiguous media is, knowing the direction of the incident light.

- **Total internal reflection**

The Snell-Descartes law shows that if $n_1 > n_2$, we have $\sin \beta > \sin \alpha \iff \beta > \alpha$. In this scenario, and in this scenario only, α is bound by a critical value α_C beyond which $\beta > 90^\circ$, which implies that the entirety of the incident ray is refracted by the interface between the two media and remains in the first media.

Logically, that critical value is obtained when $\beta = 90^\circ$, so we obtain:

$$n_1 \cdot \sin(\alpha_C) = n_2 \cdot \sin(90^\circ) \rightarrow \alpha_C = \arcsin\left(\frac{n_2}{n_1}\right) = \arcsin\left(\frac{v_1}{v_2}\right)$$

And thus, the incident ray will need to have an angle α between 0° and α_C for it to be refracted into the second medium.

2.2.2 Wavelength Dependence of the Refractive Index

A light ray with a wavelength λ_0 in a vacuum and frequency f propagating in a medium with a refractive index $n > 1$, its speed will be $v = c/n(\lambda_0)$. Its wavelength is related to its speed via the expression:

$$\lambda = v/f \tag{2.3}$$

Hence, we can write:

$$\lambda = \frac{c/n}{f} = \frac{1}{n} \cdot \frac{c}{f} = \frac{\lambda_0}{n} \Rightarrow n = \frac{\lambda_0}{\lambda} = \frac{c}{v}$$

Measurements of the wavelength or speed of light in a specific medium allows to find the value of n , and it has led to the use of the empiric use of Cauchy's equation. The expression of n as a function of λ becomes:

$$n(\lambda) = A + \frac{B}{\lambda^2} + \frac{C}{\lambda^4} + \dots \quad (\text{Cauchy's Equation for } n(\lambda))$$

Where A, B, C... are medium/material-specific constants, which have to be determined for each given medium. Considering that the term C/λ^4 is negligible in most cases, we can approximate with the following relation of proportionality:

$$n(\lambda) \propto 1/\lambda^2$$

From which we deduce that the refractive index increases as the wavelength of light decreases.

- **Air-Glass BK7 refraction of visible light**

We now consider a white light ray composed of the entire visible spectrum (400 - 700 nm) incident at an angle α and propagating from air towards a specific medium (glass BK7). Knowing the parametric coefficients of Cauchy's equation for $n(\lambda)$, we can write:

$$n_{BK7}(\lambda) = 1.5046 + \frac{4200 \text{ nm}^2}{\lambda^2}$$

Each wavelength within this range will be refracted at a specific angle β , calculating the 2 limits of the range will help us to make an estimation of the entire refraction range for visible light:

- $n_{BK7}(\lambda = 400 \text{ nm}) \approx 1.53$
- $n_{BK7}(\lambda = 700 \text{ nm}) \approx 1.51$

If we now assume an angle of incidence $\alpha = 30^\circ$, we deduce respective angles of refraction:

- $\beta_{1-2}(\lambda = 400 \text{ nm}) \approx \arcsin\left(\frac{n_{air}}{1.53} \cdot \sin \alpha\right) = 19.07^\circ$
- $\beta_{1-2}(\lambda = 700 \text{ nm}) \approx \arcsin\left(\frac{n_{air}}{1.51} \cdot \sin \alpha\right) = 19.34^\circ$

The dispersion angle $\Delta\beta = 0.27^\circ$ between the two wavelengths is minor, and forms an arc within which all wavelengths between 400 nm and 700 nm will be dispersed.

- **Glass BK7-Air refraction of visible light**

This time, we consider a similar white light ray, propagating from a glass BK7 medium to air at the same angle of incidence $\alpha = 30^\circ$ (Apex of the prism used for the MISS spectrographs). Using the same values for respective refraction indices in glass BK7, we get the new angles of refraction:

- $\beta_{2-1}(\lambda = 400 \text{ nm}) = 49.91^\circ$
- $\beta_{2-1}(\lambda = 700 \text{ nm}) = 49.03^\circ$

With the same incident angle $\alpha = 30^\circ$, we can see that this refraction allows for a more significant angular separation between the respective wavelengths (about 0.88° for BK7 glass - air compared to 0.27° for air - BK7 glass). The fact that a transition from medium 1 to medium 2 with respective refraction indices n_1 and n_2 such that $n_1 > n_2$ allows such a better dispersion explains why a prism can be used for that purpose.

2.3 Refraction Prism

2.3.1 Optimal incident angle

MISS's BK7 glass prism with apex $A = 30^\circ$ placed along the axis of propagation of an incident beam of light represents the two medium-transitions presented previously. We call α , the angle of the incident light relative to the first interface (first face of the prism), β the first angle of refraction, $(A - \beta)$ the angle relative to the second interface (second face of the prism) and γ , the second angle of refraction.

Using the Snell-Descartes law, we get:

$$n_{air} \cdot \sin \alpha = n_{BK7} \cdot \sin \beta \quad (\text{First Interface})$$

$$n_{BK7} \cdot \sin(A - \beta) = n_{air} \cdot \sin \gamma \quad (\text{Second Interface})$$

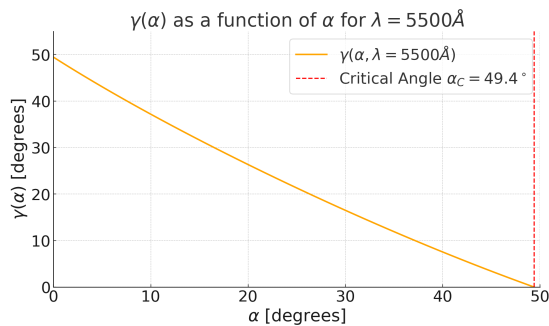
From the equation at the first interface, we have:

$$\beta = \arcsin\left(\frac{n_{air} \sin \alpha}{n_{BK7}}\right)$$

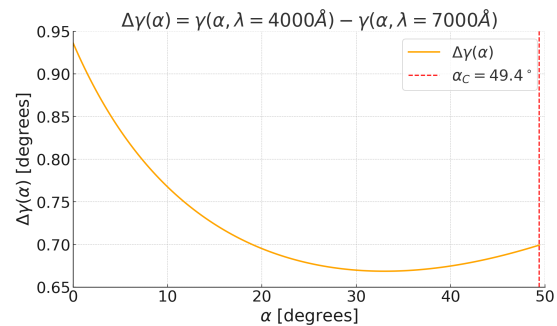
Which gives us the following expression for γ :

$$\gamma(\alpha) = \arcsin\left(\frac{n_{BK7}}{n_{air}} \cdot \sin\left[A - \arcsin\left(\frac{n_{air} \sin \alpha}{n_{BK7}}\right)\right]\right) \quad (2.5)$$

We can then use that expression to plot $\gamma(\alpha)$ for a wavelength within the VIS, $\lambda = 5500 \text{ \AA}$ (Figure 2.2a) between 0° and the critical angle α_C , showing that $\alpha = 0^\circ$ induces a maximal angular refraction. Further, we can plot the total dispersion angle $\Delta\gamma$ of the VIS (4000 - 7000 \AA) to verify that it is optimal for $\alpha = 0$ (Figure 2.2b).



(a) Figure 2.2.a: Angle of emergence as a function of α



(b) Figure 2.2.b: Total dispersion angle of the visible range

2.3.2 Dispersion angle

Using $\alpha = 0^\circ$, we can plot the refracted angle γ for all three main auroral emission lines. As evidenced in Figure 2.3, the $1/\lambda^2$ proportionality induced by the expression for the refractive index $n(\lambda)$ is verified via polynomial fit using the refracted angle at all 3 main auroral emission lines and causes smaller wavelengths to be significantly more dispersed than longer wavelengths.

$$\beta(\lambda_{VIS}) \approx \frac{2.30 \cdot 10^7}{\lambda^2} + 48.71^\circ \quad (\lambda \text{ in } \text{\AA}) \quad (2.6)$$

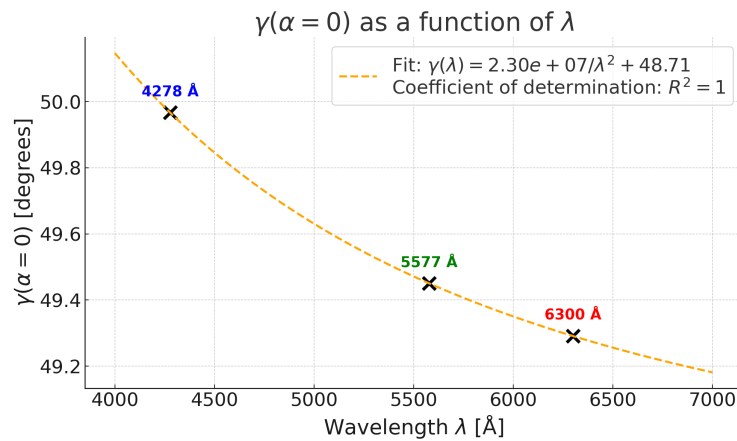


Figure 2.3: Refraction angles across VIS. Main emission lines of aurora; $\alpha = 0^\circ$.

2.4 Wave Optics

A push-broom imager such as the **MISS** spectrographs uses several optical components which, together, are here to ensure that the light from the imaged source is correctly prepared for dispersion in order to remain coherent for capture by the sensor. In this section, relevant optical notions will be presented, laying the groundwork for a full understanding of the theory involved in the functioning of a spectrometer.

2.4.1 Wave Equation

Within the boundaries of optical physics, we define light as a linear superposition of sinusoidal electromagnetic waves propagating through space and time. The electric field \mathbf{E} and magnetic field \mathbf{B} components of such a wave are perpendicular to each

other and to the wave's direction of propagation \mathbf{k} . \mathbf{E} , \mathbf{B} and \mathbf{k} are related via the "right-hand rule", which is formalised by the relation:

$$\mathbf{E} \times \mathbf{B} = c^2 \mathbf{k} \quad (2.7)$$

with c , the speed of light in a vacuum.

The expression of respective fields as functions of space and time is a solution of the wave equation, which in turn can be derived from Maxwell's equations:

Maxwell's Equations

$$\begin{aligned} \nabla \cdot \mathbf{E} &= \frac{\rho}{\epsilon} && \text{(Gauss's law for electricity)} \\ \nabla \cdot \mathbf{B} &= 0 && \text{(Gauss's law for magnetism)} \\ \nabla \times \mathbf{E} &= -\frac{\partial \mathbf{B}}{\partial t} && \text{(Faraday's law of induction)} \\ \nabla \times \mathbf{B} &= \mu\epsilon \frac{\partial \mathbf{E}}{\partial t} + \mu \mathbf{J} && \text{(Ampère's law with Maxwell's correction)} \end{aligned}$$

Where ϵ is the electric permittivity and μ the magnetic permittivity in the medium of propagation of the wave.

Determination of the Wave Equation for \mathbf{E}

To obtain a relation between spatial and temporal derivatives of \mathbf{E} , we first take the curl of *Faraday's law of induction*:

$$\nabla \times (\nabla \times \mathbf{E}) = -\frac{\partial}{\partial t} (\nabla \times \mathbf{B})$$

The vector identity $\nabla \times (\nabla \times \mathbf{E}) = \nabla(\nabla \cdot \mathbf{E}) - \nabla^2 \cdot \mathbf{E}$ allows us to rewrite the left-side expression, substituting $\nabla \cdot \mathbf{E}$ by ρ/ϵ according to *Gauss's law for electricity*:

$$\nabla(\nabla \cdot \rho/\epsilon) - \nabla^2 \cdot \mathbf{E} = -\frac{\partial}{\partial t} (\nabla \times \mathbf{B})$$

We identify the curl of \mathbf{B} , which can be substituted according to *Ampère's law with Maxwell's correction*, and consider a non-conductive medium, so we can approximate $\rho = 0$ and $\mathbf{J} = 0$ and further simplify accordingly:

$$-\nabla^2 \cdot \mathbf{E} = -\frac{\partial}{\partial t} \left(\mu\epsilon \frac{\partial \mathbf{E}}{\partial t} \right)$$

Which gives us the wave equation for \mathbf{E} and for \mathbf{B} , substituting ∇^2 with the Laplacian operator $\Delta = \nabla^2$ and $\mu\epsilon$ with $1/v^2$, v being the speed of light in the medium of propagation:

$$\Delta \cdot \mathbf{E} - \frac{1}{v^2} \frac{\partial^2 \mathbf{E}}{\partial t^2} = 0 \quad (2.9)$$

Expression of \mathbf{E}

Considering a plane wave propagating along the x-axis with its electric field along the y-axis and its magnetic field along the z-axis, the solution of the wave function for the field \mathbf{E} is a complex sinusoidal function of space and time of the following form:

$$E(x, t) = E_x e^{i(kx - \omega t + \varphi)} \quad (2.10)$$

Expanding it using Euler's formula ($e^{i\theta} = \cos \theta + i \sin \theta$), we can extract $Re\{\mathbf{E}(x, t)\}$, the real part of $\mathbf{E}(\mathbf{x}, \mathbf{t})$, which is usually used to represent the wave in a simple manner:

$$E(x, t) = E_0 \cos(kx - \omega t + \varphi) \quad (2.11)$$

Where E_0 represents the maximum amplitudes of the electric field, k its wave number such that $k = \frac{2\pi}{\lambda}$, ω its angular frequency such that $\omega = 2\pi\nu$ with ν , the frequency of the wave in Hertz (periods per second) and φ , the wave's phase.

2.4.2 Interference and Diffraction

Interference is the phenomenon that occurs when two or more waves propagate in the same space, effectively superposing. At any point in space where several waves interfere, their respective intensities will combine in a constructive (combined intensities) or a destructive way (subtracted intensities), depending on whether they are the same or opposite signs respectively.

The simplest scenario is the case where two identical waves with different phases φ_1 and φ_2 interfere. That configuration can be obtained using a single source S and two slits placed at the same distance from S , i.e. Young's double slit experiment.[25] That experiment can then be extended to a parallel wave from the same source S split into N waves through N evenly spaced slits. This configuration allows for the light waves to interfere. In this section, the effects of one, two and N slits will be presented.

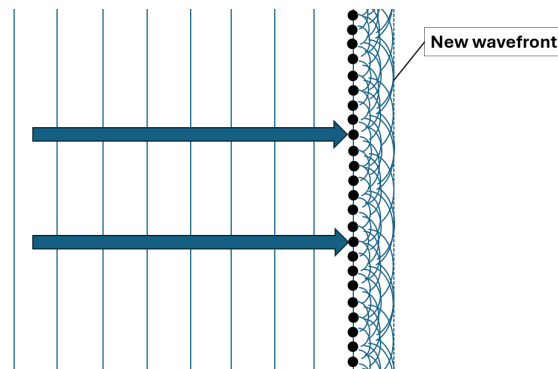


Figure 2.4: Wavelet-induced wavefront According to Huygens-Fresnel Principle

- **Light through one slit (Huygens-Fresnel Principle)**

According to the Huygens-Fresnel principle, a moving wavefront is merely the source of secondary, spherical wavelets which are generated at every point of the wavefront of a plane wave.[26] And so, as they propagate through infinitesimal distances, they add up to an infinite amount of wavelets, which interfere with each other in a destructive way in all directions but forward and form the new wavefront, as illustrated in Figure 2.4.

The single-slit experiment is a demonstration of that phenomenon. When propagating through a slit, a monochromatic plane wave will continue to propagate producing wavelets, within the limits of the slit width, with two main secondary sources on respective edges, leading to the propagation of a spherical wave and a diffraction pattern which is characterised by the wavelength λ of the wave and the width a of the slit, as shown in Figure 2.5. The diffraction pattern is described by the following formula:

$$a \sin \theta = m\lambda \quad (2.12)$$

Here, a represents the width of the slit, m the diffraction order, θ the angle of diffraction relative to the original angle of propagation and λ , the wavelength of the wave. $a \sin \theta$ as a whole represents the path difference Δ between the two edges of the slit.

From this expression, we get $\sin \theta = m\lambda/a$, showing what values for θ will get us the intensity minima (but not the maxima) at order m , for $\theta \neq 0^\circ$. As the ratio λ/a decreases, consecutive maxima will get at a closer angle from each other, which implies that a small slit width relative to the wavelength of the wave will optimise

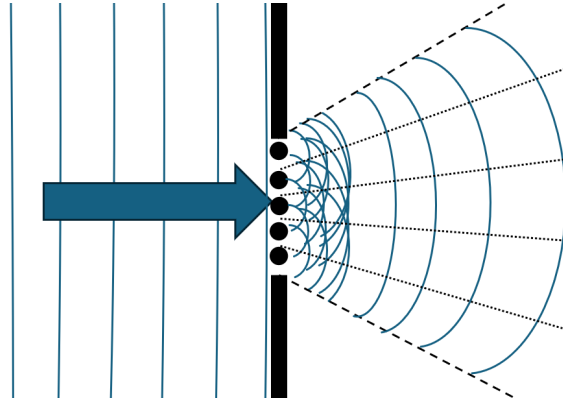


Figure 2.5: Single-slit diffraction experiment

the diffraction fringes observed and render them more visible. The intensity I of the diffracted light projected onto a screen placed at a distance y from the slit is a function of θ and can be derived for the electric field $E(\theta)$ of the diffracted light, knowing that $I \propto |E|^2$.

Let us first consider that $E(\theta)$ is the sum of infinitesimal contributions dE from across the entire width of the slit along the x -axis. Each contribution will logically amount to the portion $dE = E_0(dx/a)$, so $E(\theta)$ can be expressed according to the Fraunhofer diffraction equation [27]:

$$E(\theta) = \int_{-a/2}^{+a/2} \frac{E_0}{a} e^{i\delta} dx$$

with δ , the phase difference such that $\delta = k\Delta = \frac{2\pi}{\lambda} \cdot x \sin \theta$.

$$E(\theta) = \frac{E_0}{a} \int_{-a/2}^{+a/2} \exp\left(\frac{i2\pi x \sin \theta}{\lambda}\right) dx \quad (2.13)$$

The integral can then easily be expressed with the primitive of this exponential function:

$$E(\theta) = \frac{E_0}{a} \left[\frac{e^{\frac{i2\pi x \sin \theta}{\lambda}}}{\frac{i2\pi \sin \theta}{\lambda}} \right]_{-a/2}^{+a/2} = \frac{E_0}{a} \left[\frac{e^{\frac{i2\pi(a/2) \sin \theta}{\lambda}} - e^{\frac{i2\pi(-a/2) \sin \theta}{\lambda}}}{\frac{i2\pi \sin \theta}{\lambda}} \right]$$

Using Euler's formula, $e^{i\alpha} - e^{-i\alpha} = 2i \sin \alpha$, we can simplify the expression:

$$E(\theta) = \frac{E_0}{a} \left[\frac{2i \sin\left(\frac{\pi a \sin \theta}{\lambda}\right)}{\frac{i2\pi \sin \theta}{\lambda}} \right] = E_0 \left[\frac{\sin\left(\frac{\pi a \sin \theta}{\lambda}\right)}{\frac{\pi a \sin \theta}{\lambda}} \right]$$

Substituting with $\beta = \frac{\pi a \sin \theta}{\lambda}$, we get the following condensed expression:

$$E(\theta) = E_0 \left(\frac{\sin \beta}{\beta} \right) = E_0 \cdot (\beta)$$

And thus, $I(\theta)$ can be expressed as follows:

$$I(\theta) = I_0^2 \beta \quad \text{with} \quad \beta = \frac{\pi a \sin \theta}{\lambda} \quad (2.14)$$

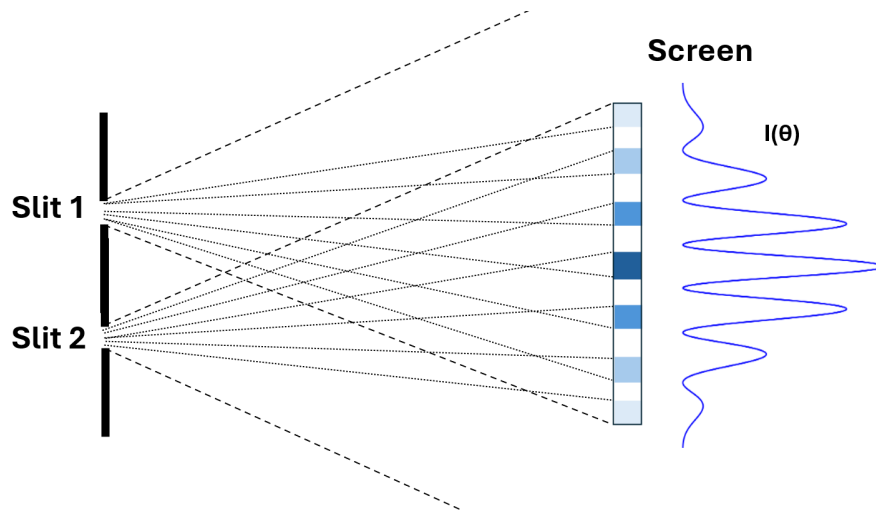


Figure 2.6: Young's double-slit experiment

- **Light through two slits (Young's double-slit experiment)**

Young's double-slit experiment, first performed by Thomas Young in 1801, is famously known for being the first documented demonstration of the dual nature of light, showing that this method of interferometry can be described via either quantum mechanics or classical wave optics, the latter being the relevant approach here.

Similarly to the one-slit experiment, a monochromatic coherent plane wave from a single source S is now propagating through two identical slits placed at a distance d from each other and better described as secondary sources E_1 and E_2 . The resulting

wave depicted in Figure 2.6 will therefore have the combined properties of a single spherical wave with diffraction patterns due to its passage through a slit and an additional interference pattern between two such waves. We will use the Fraunhofer diffraction equation in this scenario too, to illustrate the shape of the resulting light which can be expected to be captured via its intensity as a function of the angle θ , which can be accurately defined as the angle of the point of observation relative to the central axis, perpendicular to the plane of the two slits.

It was previously demonstrated that the light emanating from a single slit will have its intensity and electric field expressed as:

$$I(\theta) = I_0^2 \beta \quad \text{and} \quad E(\theta) = E_0 (\beta) \quad [23] \quad (1)$$

Adding a second wave will induce a second source of interference due to their path difference $\Delta = d \sin(\theta)$, leading to a phase difference $\delta = \frac{2\pi\Delta}{\lambda}$. On all points of the surface of a screen placed in front of the slits, we will now have a resulting electric field $E(\theta) = E_1(\theta) + E_2(\theta)$ from S_1 and S_2 respectively, where we can express E_2 as:

$$E_2 = E_1 e^{i\delta} = E_0 \cdot \beta \cdot e^{i\delta}$$

Hence a resulting electric field such that:

$$E = E_0 \beta \cdot (1 + e^{i\delta})$$

Using Euler's formula gives us $1 + e^{i\delta} = 2 \cos\left(\frac{\delta}{2}\right) \cdot e^{i\delta/2}$ so we can write:

$$E = E_0 \beta \cdot 2 \cos\left(\frac{\delta}{2}\right) e^{i\delta/2} = 2E_0 \left[\beta \cdot \cos\left(\frac{\delta}{2}\right) \cdot e^{i\delta/2} \right]$$

Using this complex expression of E, we can simply calculate as $I(\theta) \propto |E|^2$ i.e. $I(\theta) = k |E|^2$ with $k \equiv \text{constant}$:

$$I = k \cdot \left| 2E_0 \cdot \beta \cdot \cos\left(\frac{\delta}{2}\right) e^{i\delta/2} \right|^2 = I_0 \cdot^2 (\beta) \cdot \cos^2\left(\frac{\delta}{2}\right) \cdot 1 \quad \text{with} \quad I_0 = k \cdot 4 |E_0|^2$$

And thus, we get the final expression for $I(\theta)$:

$$I(\theta) = I_0 \cdot^2 \beta \cdot \cos^2\left(\frac{\delta}{2}\right) = I_0 \cdot^2 \left(\frac{\pi a \sin \theta}{\lambda}\right) \cos^2\left(\frac{2\pi d \sin \theta}{\lambda}\right) \quad (2.15)$$

This expression encompasses the cumulative effects of the diffraction of a wave with

itself when transmitted through a slit and the interference between two such waves. (β) can be assimilated to the envelope of the function, giving the overall shape of the pattern whereas $\cos^2\left(\frac{\delta}{2}\right)$ is giving its varying value within each diffraction order. It is important to note for ulterior use that the frequency of the wave λ plays an important role in both terms of the expression, one specific value of I at fixed angle θ being wavelength-specific.

• Light through N slits

The N-slit experiment is the mathematical extension of the previous experiment with two slits. As we add more slits in the same plane, at an identical distance d from each other, the number of destructive and constructive fringes per *diffraction order* will increase dramatically, leading to a very fine interference pattern. This can be expressed summing up all N electric fields superposed at an angle θ :

$$E(\theta) = \sum_{n=0}^{N-1} E_0 e^{in\delta} = E_0 + E_0 e^{i\delta} + E_0 e^{i2\delta} \dots$$

Knowing $\sum_{n=0}^{N-1} a^n = \frac{1-a^N}{1-a}$, we can rewrite this sum as:

$$E(\theta) = E_0 \left(\frac{1 - e^{iN\delta}}{1 - e^{i\delta}} \right)$$

Let us now rearrange this expression and use: $\frac{e^{i\alpha} - e^{-i\alpha}}{2i} = \sin \alpha$.

$$E(\theta) = E_0 \left(\frac{e^{-iN\delta/2}(e^{-iN\delta/2} - e^{iN\delta/2})}{e^{-i\delta/2}(e^{-i\delta/2} - e^{i\delta/2})} \right) = E_0 \left(\frac{e^{-iN\delta/2}(-2i \sin(N\delta/2))}{e^{-i\delta/2}(-2i \sin(\delta/2))} \right)$$

And finally:

$$E(\theta) = E_0 \left(\frac{\sin(N\delta/2)}{\sin(\delta/2)} e^{i(1-N)\delta/2} \right)$$

From this expression, we can express the intensity distribution at an angle θ , with the "envelope-factor" $I_0 \beta$ induced by the diffraction a single slit. With $\delta = \frac{2\pi}{\lambda} \cdot x \sin \theta$ and $\beta = \frac{\pi a \sin \theta}{\lambda}$, we can write:

$$I_N(\theta) = I_0 \left(\frac{\sin\left(\frac{N\delta}{2}\right)}{\sin\left(\frac{\delta}{2}\right)} \right)^2 \cdot I_0 \beta = I_0 \left[\frac{\sin\left(\frac{N\pi d \sin \theta}{\lambda}\right)}{\sin\left(\frac{\pi d \sin \theta}{\lambda}\right)} \right]^2 \cdot \left[\frac{\sin\left(\frac{\pi a \sin \theta}{\lambda}\right)}{\frac{\pi a \sin \theta}{\lambda}} \right]^2 \quad (2.16)$$

Normalised Intensity Distribution as a function of θ for $\lambda = 5577 \text{ \AA}$ (Green line)
 slit width $a = 5.56\text{e-}07 \text{ m}$, slit separation $d = 3a = 1.67\text{e-}06 \text{ m}$

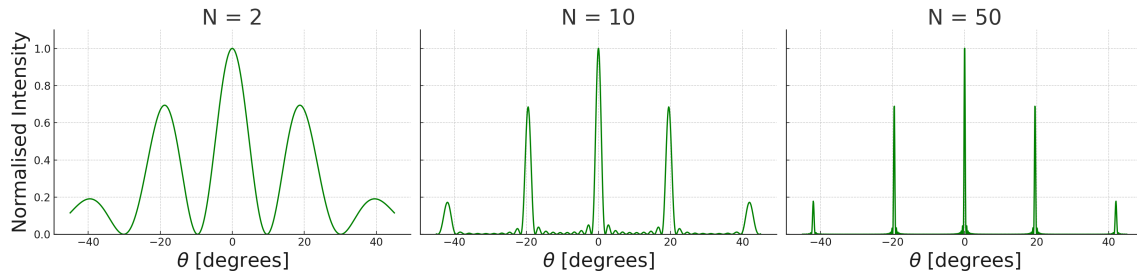


Figure 2.7: Normalised intensity distribution as a function of θ for $\lambda = 5500 \text{ \AA}$.
 Plot adapted from [23].

The plots of this expression for $N = 2, 10$ and 50 slits at $\lambda = 5577 \text{ \AA}$ in Figure 2.7 show that an increasing amount of slits will lead to significantly thinner, line-like bright fringes. With a line to be found at a clear, distinct location on the screen for each different wavelength (cf. Figure 2.8) and within the bright fringe of a given diffraction order, except the central bright fringe (order 0), where all wavelengths are superposed. This is a very advantageous effect and a fundamental feature in the field of spectroscopy.

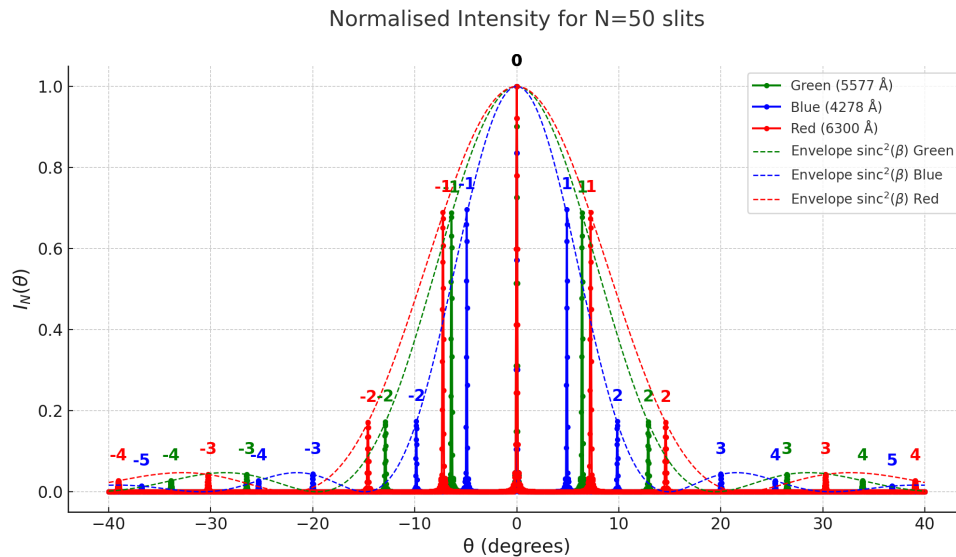


Figure 2.8: Normalised intensity distribution for emission lines of aurora, $N=50$.
 Plot adapted from [23].

2.4.3 Overlapping Orders and Non-Linear Dispersion

Figure 2.8 illustrated several key features of light diffraction using a grating. Namely, that although the angular dispersion between wavelengths is much more significant than via prism refraction, the wavelengths from different orders may superpose in space, as can be observed within the visible range beyond orders ± 2 . If the incident light beam consists of a broad wavelength range, it is therefore likely that *overlapping orders* will be observed at any order of diffraction.

Furthermore, the angular spacing between the three main auroral emission lines of a single diffraction order shows a very pronounced non-linearity, with a dispersion more pronounced for longer wavelengths.

2.5 Diffraction Grating

A diffraction grating is an optical component composed of a series of closely spaced thin slits, which efficiently separates different wavelengths of light from a source emitting multiple specific wavelengths according to the phenomena of diffraction presented earlier.

Increasing the number of slits in the path of the incident light enhances the interference-induced narrowing of the light diffracted by a grating surface. This results in better separation between different wavelengths within a single diffraction order, i.e. improved *spectral resolution*. The amount of slits is more conveniently expressed as a slit density σ , in amount of grooves per millimetre, where the grating spacing a can simply be calculated as $d = 1/\sigma$ in millimetres.

2.5.1 Grating Types and Characteristics

There are several types of gratings, the two traditional ones being simple reflection and transmission gratings. Each serves various purposes in spectrometry, with unique characteristics and geometries.

- **Reflection grating**

Reflection gratings use a reflective material with parallel grooves closely engraved on its surface. This creates a periodic arrangement of narrow parallel reflective surfaces (tiny mirror), each acting as a secondary source. The path difference between the reflected waves leads to phase differences, forming interference fringes similar to those produced by slits.

- **Transmission Grating**

A transmission grating uses narrow lines or *grooves* etched on a transparent material which allows the light it disperses to pass through. These grooves act similarly to slits, diffracting light as it passes through. This type is commonly used in the dispersing elements of spectrometers due to its effectiveness in separating wavelengths and the fact that it allows an on-axis dispersion of light, which is ideal for a compact design such as the [MISS](#) spectrographs.

The [MISS](#) spectrographs use a *Blazed Ruled Transmission Grating*, let us explicate more specifically the characteristics of such a grating.

- **Blazed grating**

Blazed gratings, also called echelette gratings (from the French *échelle* (small ladder)) are a type of reflection or transmission grating where the grooves are engraved at an angle to direct most of the diffracted light into a specific order, most of the light intensity residing in the central fringe if that angle is zero, as shown in [Figure 2.9](#). This angle optimises the dispersion of one specific wavelength. All other unwanted orders of diffraction are attenuated, which makes it a necessary device when used for the detection of a specific, narrow emission line with a maximised intensity.

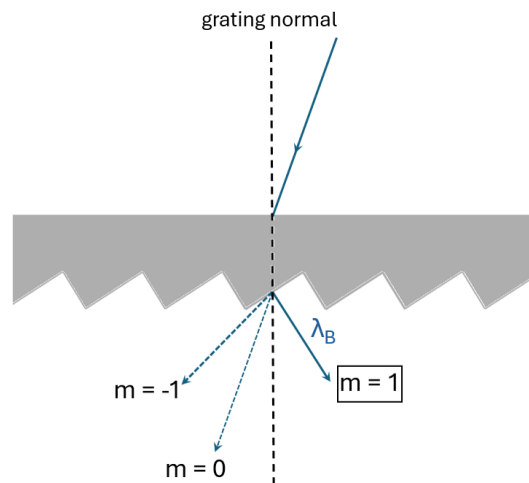


Figure 2.9: Blazed grating optimising one specific wavelength λ_B at diffraction order $m = 1$

- **Ruled Grating**

The grooves of that type of grating are etched mechanically onto the grating's transparent surface using a diamond-tipped ruling tool. They are usually sawtooth-shaped, at an angle which corresponds to the grating's blazing angle, allowing a selected diffraction order of a specific wavelength range to be selected.

2.5.2 Grating Equation

The diffraction pattern of an incident plane wave diffracted at a normal angle relative to the normal axis of two or more slit separated by a distance d is given by the expression of the path difference Δ between two adjacent slits: $d \sin \beta = m\lambda$. This is a special case where the angle of the incident light α equals 0° relative to the normal to the axis formed by the grooves. A plane wave with any incident $\alpha \neq 0^\circ$ implies an additional path difference $d \sin \alpha$, which gives a total path difference $\Delta = d \cdot \sin \alpha \pm d \cdot \sin \beta$. From this, it comes the following *grating equation* for the in-plane diffracted light [23]:

$$m\lambda = d(\sin \alpha + \sin \beta) \quad \text{(Grating Equation)}$$

This equation allows the prediction of the location of the bright fringe of the diffraction order of interest. As such, it is central in the design of a spectrograph using grating.

2.5.3 Blazed Wavelength

In practice, using a blazed grating is of high importance as it will help focusing the spectrograph on the right set of wavelength. A blazed grating is defined by its *blaze angle* θ_B , which is the angle of each groove relative to the plane of the grating surface.

This angle will allow one specific wavelength to be dispersed at maximum efficiency; it is the *blazed wavelength* λ_B .

The blazed grooves of a transmission grating can be approximated as triangular prisms with a refractive index $n_B \approx 1.6$. This refraction at the scale of a single groove will have to be accounted for, using the Snell-Descartes law on the angle of diffraction β , and allows λ_B to be conveniently approximated with a 10% uncertainty as follows, according to Newport Corporation, a well-established provider of diffraction gratings and related optical components [28]:

$$\lambda_B \approx (n_B - 1)d \cdot \sin \theta_B \quad (2.17)$$

If we take:

- $\theta_B = 28.7^\circ$ (Blazed angle of the grating used for the MISS spectrographs)
- $d = 1/\sigma = \frac{1}{600\text{mm}^{-1}} = 1.667 \cdot 10^{-6} \text{ m}$ (Grating spacing for the MISS spectrographs)

We can compute the value of the blazing wavelength:

$$\lambda_B(\theta_B = 28.7^\circ, d = 1.667 \cdot 10^{-6} \text{ m}) = 4800 \pm 480 \text{ \AA}$$

Following this estimate, it comes that the curve for the grating efficiency will be at its maximum in the VIS range, which is optimal in our case.

2.5.4 Grating Efficiency for MISS

Grating efficiency represents the proportion of the incident light intensity diffracted into a specific diffraction order. Parameters previously reviewed, such as the type of grating, its groove density and the type and shape of the grooves all affect grating efficiency.

In the case of the MISS spectrographs, where the visible range (4000 Å – 7000 Å) is of interest, it is not only necessary to have a high grating efficiency within that range, it is also crucial to make sure that potential overlapping fringes from higher diffraction orders are not transmitted. Blazed grooves are instrumental in ensuring that, as they will not only favour a specific wavelength range, but also a specific diffraction order, which is the first diffraction order for the MISS spectrographs.

The curve of the absolute grating efficiency as a function of wavelength can be assessed experimentally and is commonly provided by the manufacturer, as is the case for the grating manufactured by ThorLabs used for MISS 2 (Figure 2.10).

Comparing the trend of these curves within VIS, it is clear that the grating with 600 grooves/mm offers high absolute efficiency throughout most of that range, but also an efficiency plateau from about 4000 Å towards increasing wavelengths, with a decline only occurring near 6000 Å.

The balanced efficiency it provides for a satisfyingly high spectral resolution (300 grooves/mm is too limiting), compared to the quickly declining absolute efficiencies for gratings with higher groove densities shows that it is a coherent choice in the case of the MISS spectrographs, where the spectral resolution does not need to be especially high, whereas significant absolute efficiency variations throughout the visible range would imply significant detrimental compromises for the exposure time, in order to prevent any under- or overexposure.

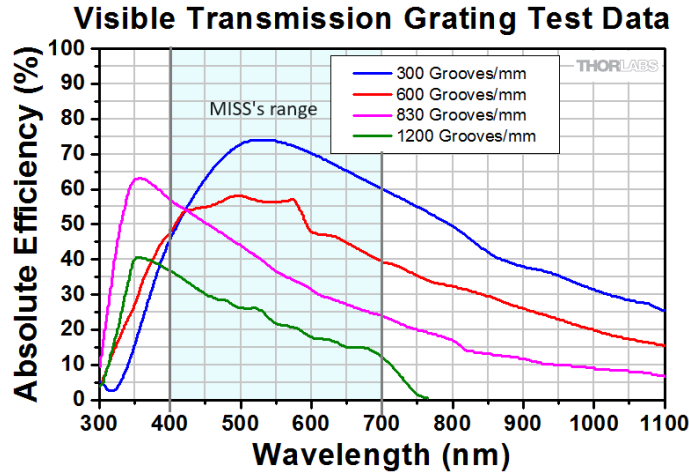


Figure 2.10: Absolute grating efficiencies with various groove densities provided by *ThorLabs* [29]

Curve in red: MISS's 600 grooves/mm grating.

2.6 Dispersive Element of MISS

The MISS spectrographs use a Tunable air-spaced Transmission Grating and Prism (TGRISM) as their dispersive element. It uses the combined effects of diffraction grating and refraction prism presented in the previous parts of this Chapter. The objective is to balance the respective effects of these opposite nonlinear dispersions to obtain a quasi-linear, well-resolved dispersion.

In this section, the focus will be put on offering an exhaustive description of the resulting dispersion of light using such a device, by first bridging the geometrical approach governed by the Snell-Descartes Law and the Grating Equation.

2.6.1 GRISM Equation

For the sake of simplicity, we first consider the case where the surface of the grating is perfectly parallel to the second side of the prism with an apex $A = 30^\circ$.

By geometry, the beam of light refracted by the prism with a wavelength λ will reach the surface of the grating at an angle of incidence $\theta_i = \beta = \arcsin[n_{BK7}(\lambda) \cdot \sin 30^\circ]$ and then be diffracted by the grating at an angle θ_m at diffraction order m . We can therefore substitute θ_i with this expression in the Grating Equation:

$$m\lambda = d(n_{BK7}(\lambda) \cdot \sin A + \sin \theta_m) \quad (\text{GRISM Equation [23]})$$

This specific set-up is designed to get a close to on-axis effect to keep optimal image quality. Ideally, the centre of our CCD screen should show green light ($\approx 5500\text{\AA}$) at a diffracted angle $\theta_m = -\alpha = -A = -30^\circ$ (negative according to the grating equation convention as it is in the 4th quadrant, on the opposite side of the grating's normal), i.e. parallel to the light entering the GRISM. For this specific case, the GRISM equation becomes:

$$m\lambda = d \cdot \sin 30^\circ (n_{BK7}(\lambda) - 1)$$

From which we can verify that:

$$\lambda(\theta_m = -30^\circ) = \frac{d}{2}(n_{BK7}(\lambda) - 1) \approx 4400 \text{ \AA} \quad (\text{On-axis Wavelength})$$

From this estimation and as illustrated in Figure 2.11, we can see that without any correction, the centre of the image obtained would show a wavelength around 4400 \AA (blue-violet), whereas we want a complete visible spectrum with a 4000-7000 \AA range centred around the green wavelengths ($\sim 5500 \text{ \AA}$). That is why the air-spaced transmission grating is tunable: An angular adjustment of the grating (tilt angle) will allow us to correct the diffracted angles of all visible light just enough to allow an optimal centring.

Dispersed angles at both extremities and centre of the visible range:

Wavelength λ (\AA)	θ_m (degrees)
4000	-32.00
5500	-25.50
7000	-19.70
Angular dispersion (GRISM, VIS): $\Delta\theta_m = 12.30^\circ$	

Table 1: Values of θ_m and deduced angular dispersion

2.6.2 Tilt Angle and TGRISM Equation

Let us rearrange the GRISM equation to account for a new tilt angle τ on the tunable grating, which should correct the diffraction angles so that the wavelengths around 5500 \AA reach the centre of the image obtained. The TGRISM equation becomes:

$$m\lambda = d [\sin (\arcsin (n_{BK7}(\lambda) \cdot \sin A) + \tau) + \sin(\theta_m)] \quad (\text{TGRISM Equation})$$

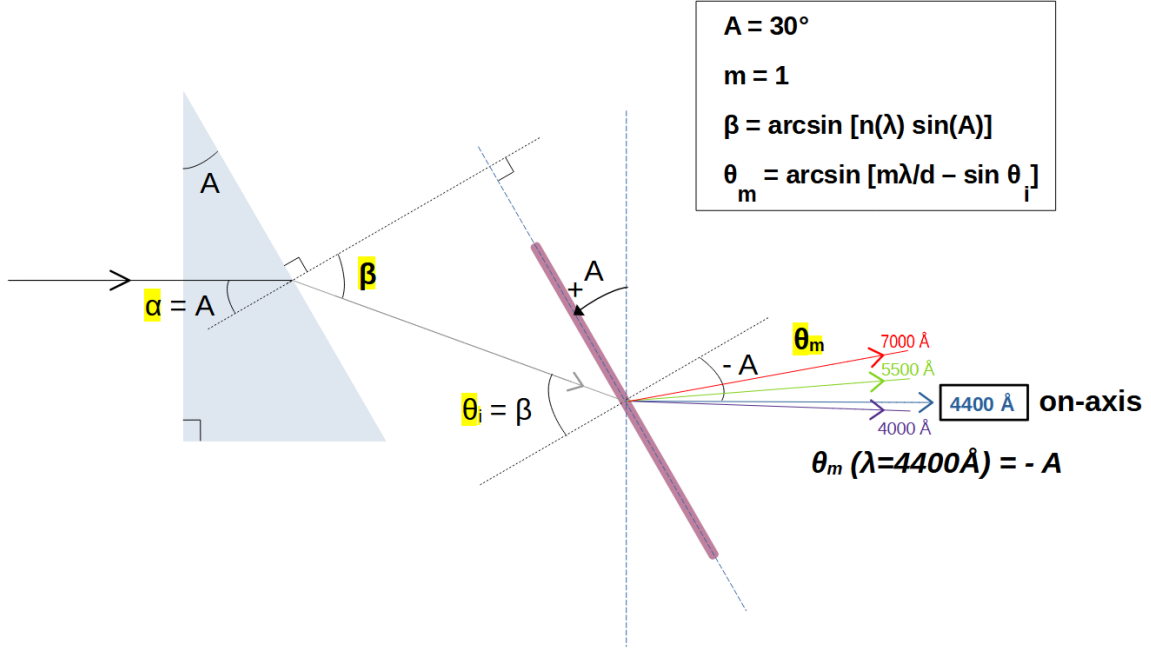


Figure 2.11: Dispersion by the TGRISM of MISS

Following the sign convention, τ is positive in the case of an anti-clockwise rotation of the grating. $\tau = 0$ implies that the grating surface is at an initial inclination A . We can now make an estimation of the tilt angle required in order to satisfy the requirements, $\theta_m(\lambda = 5500\text{\AA}) = -(A + \tau)$:

According to the *TGRISM equation*, at diffraction order $m = 1$, we have:

$$\frac{\lambda}{d} = [\sin(\arcsin(n_{\text{BK7}}(\lambda) \cdot \sin A) + \tau) + \sin(\theta_m)]$$

Using the identity: $\sin(x) - \sin(y) = 2 \cos\left(\frac{x+y}{2}\right) \sin\left(\frac{x-y}{2}\right)$, we get:

$$\frac{\lambda}{d} = 2 \cos\left(\frac{\arcsin(n_{\text{BK7}}(\lambda) \cdot \sin A) + \tau + \theta_m}{2}\right) \cdot \sin\left(\frac{\arcsin(n_{\text{BK7}}(\lambda) \cdot \sin A) + \tau - \theta_m}{2}\right)$$

We isolate the cosine term:

$$\frac{\lambda}{2d \cdot \sin\left(\frac{\arcsin(n_{\text{BK7}}(\lambda) \cdot \sin A) + \tau - \theta_m}{2}\right)} = \cos\left(\frac{\arcsin(n_{\text{BK7}}(\lambda) \cdot \sin A) + \tau + \theta_m}{2}\right)$$

And we deduce the expression for τ :

$$\tau = 2 \cdot \arccos \left(\frac{\lambda}{2d \cdot \sin \left(\frac{\arcsin(n_{\text{BK7}}(\lambda) \cdot \sin A) + \tau - \theta_m}{2} \right)} \right) - \arcsin(n_{\text{BK7}}(\lambda) \cdot \sin A) - \theta_m$$

Finally, substituting the known values for MISS ($A = 30^\circ$, $d = 1.6667 \times 10^{-6} \text{ m}$), $n_{\text{BK7}}(\lambda = 5500 \text{ \AA}) = 1.5187$ and $\lambda = 5500 \text{ \AA}$), we get:

$$\tau \approx -29.54^\circ$$

In practice, a clockwise tilt angle $-\tau$ of roughly 29.5° (according to the sign convention), corresponding to a nearly vertically aligned grating, will allow a satisfying centering of the visible range around the green range. This significant tilt angle required has implications on the off-axis effects arising at wavelengths significantly different from the on-axis wavelength, the estimated value of the wavelength remaining on-axis without any correction.

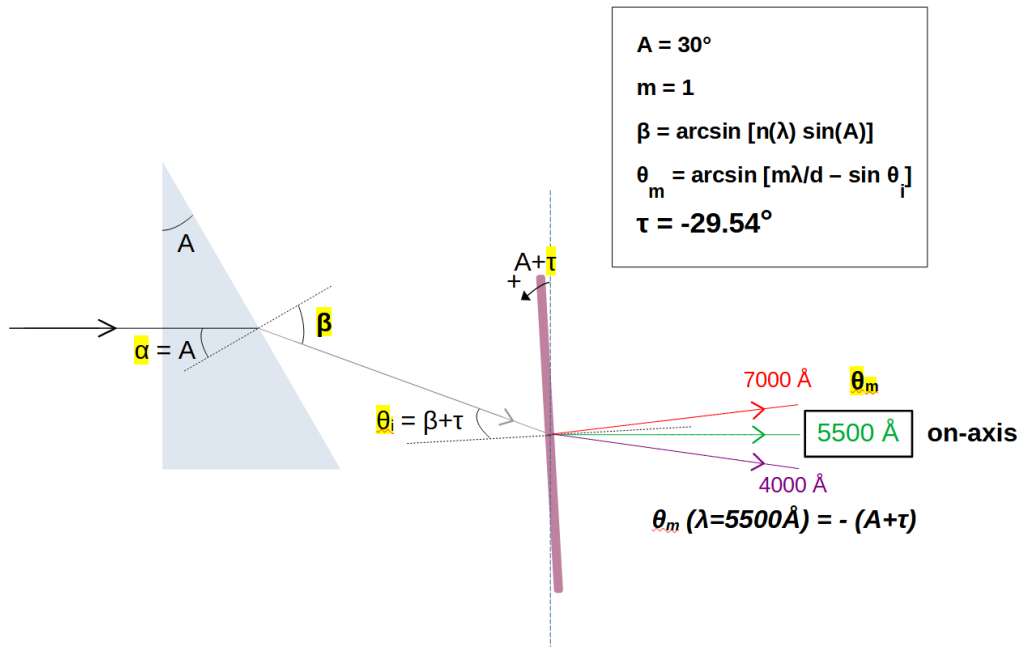


Figure 2.12: Dispersion by the TGRISM of MISS with tilt angle correction

According to the expression for the on-axis wavelength derived from the GRISM Equation, a prism made in a material with a greater refractive index $n(\lambda)$ would

allow an increased on-axis wavelength, and thus, a centering around the green range with a minimal adjustment required.

Using the TGRISM Equation with a known τ , we can now make estimations for the angular diffraction of red (7000 Å) and violet (4000 Å) in the visible range in order to make a full representation of the path taken by the visible light through the TGRISM (Figure 2.12) and make an estimation of the total angular dispersion $\Delta\theta_m$:

Dispersed angles at both extremities and centre of the visible range:

Wavelength λ (Å)	θ_m (degrees)
4000	4.60
5500	-0.46
7000	-5.73
Angular dispersion (TGRISM, VIS): $\Delta\theta_m = 10.33^\circ$	

Table 2: Values of θ_m and deduced angular dispersion

3 Instrument Design

In this Chapter, all components involved in the operation of MISS 2 are presented. It includes a description of how these components integrate with the TGRISM to perform hyperspectral imaging. It then continues with a review of the main metrics having an impact on the overall performance of our spectrograph and its capacity to provide satisfactory imaging of auroral phenomena.

3.1 Optical Design of MISS

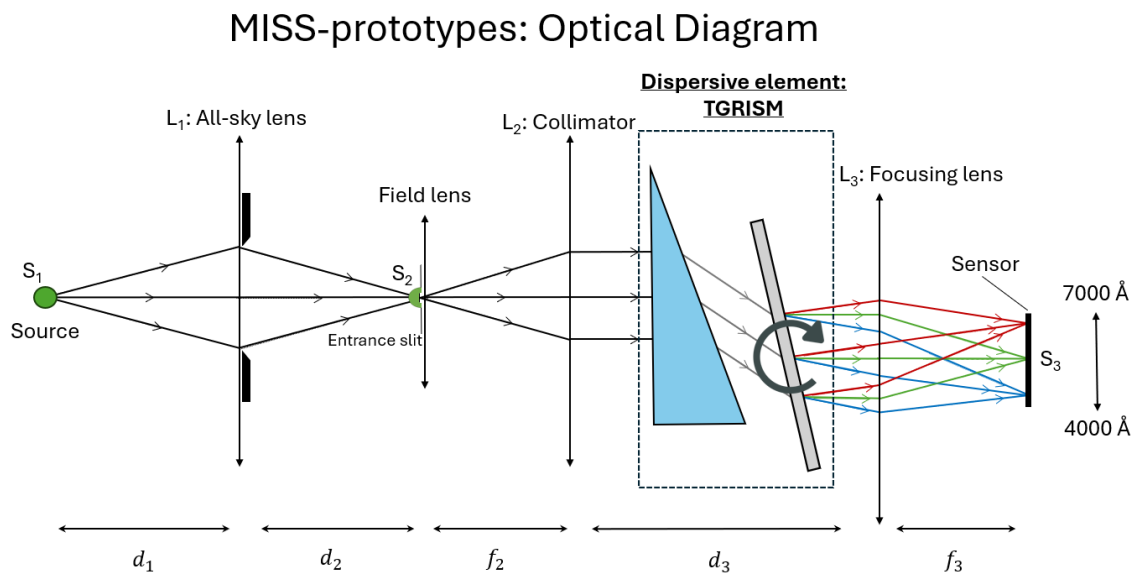


Figure 3.1: MISS2's Optical Diagram (adapted from [23])

As represented in Figure 3.1 above, the light from the source (entire sky) goes through the **all-sky lens** (L_1 , Peleng $f_1 = 8 \text{ mm}$) and is focused onto the **entrance slit** (width: $w = 0.1 \text{ mm}$). The light of the image formed by the slit is then reimaged by a **field lens** (32-979 Edmund Optics, $f_F = 50 \text{ mm}$), guiding the beam towards a **collimating lens** (L_2 , AC508-200-A-ML Thorlabs $f_2 = 200 \text{ mm}$), beyond which the now parallel light beam can be properly dispersed by the **TGRISM**. Finally, the resulting separated wavelengths are focused by the **focusing lens** (L_3 , Nikkor $f_3 = 35 \text{ mm}$) onto the surface of the **sensor** (CCD Atik 414EX camera).

3.1.1 All-sky Lens

An all-sky lens; the first prototype of which was patented as "fisheye-lens system" in 1973 (cf. Figure 3.2), in reference to the characteristic curved appearance of images taken using that type of lens; is used for the MISS spectrographs. This complex type of lens system is arranged in order to allow all incident light from any angle incident to the system's first, heavily convex lens into the optical system, while preventing the entry of stray light.

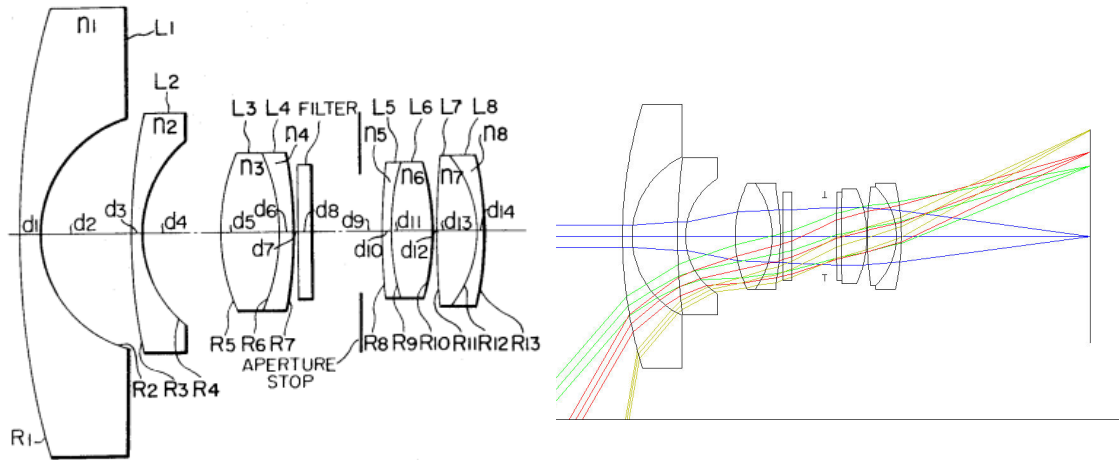


Figure 3.2: First Fish-eye layout (1973) [30] and corresponding optical layout [31]

This type of front-lens is used for all-sky imaging and allows MISS's required 180° FOV from a source at $d_1 \sim \infty$. However, the optical distortions remain significant by nature, especially at high degrees of incidence and need to be accounted for during the processing of the spectrograms captured by our imagers. Its characteristically small focal length f_1 impacts the overall spectral and spatial resolutions negatively and its wide aperture improves the signal-to-noise ratio (SNR).

3.1.2 Entrance Slit

The entrance slit is positioned behind the all-sky lens at the image distance d_2 . The incident light from the source is focused onto it as a disk of light with a surface S_2 and a diameter L , as illustrated in Figure 3.3. Only a specific portion of the sky passes through the slit, meaning a narrow strip of light from the entire 180° FOV is

selected.

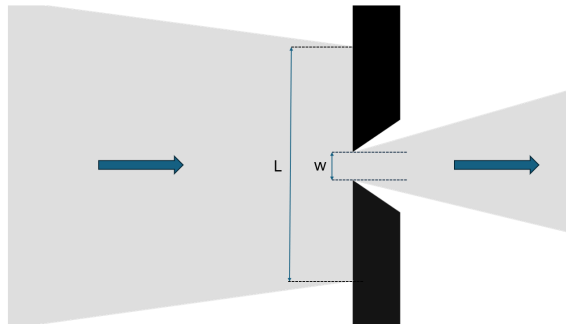


Figure 3.3: Beam of light through the slit entrance of MISS (width $w = 0.1\text{mm}$, length $L = 24\text{mm}$)

The slit width w affects spatial coherence: a narrower w allows an improved spatial resolution as the light from each portion of the FOV can be more closely identified as a specific mono-dimensional point in space, while a wider opening allows a higher light intensity into the optical system. Therefore, a balance must be found to allow sufficient light intensity across the entire FOV while maintaining an acceptable spatial resolution.

3.1.3 Field Lens

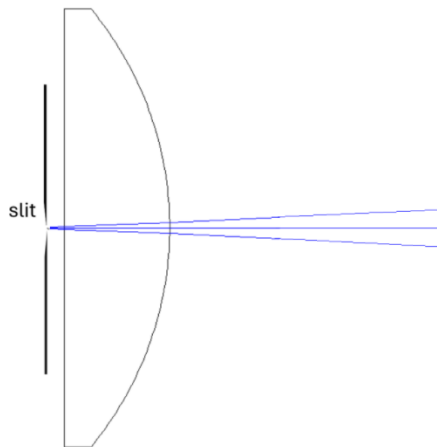


Figure 3.4: Reimaging by the plano-convex field lens ($f_F = 50\text{ mm}$) of MISS (OSLO software)

The incident light admitted through the slit would logically start diverging strongly, having formed a sharp image at a distance d_2 from the all-sky lens. A field lens (Figure 3.4), or *re-imaging system*, is therefore placed as close to the slit as possible to mitigate *vignetting*; i.e., loss of light intensity around the edges of the beam formed by the light admitted into the optical system; by converging the light so as to make up for the distance between the entrance slit and the collimating lens. As such, it can be considered an auxiliary component used for optical efficiency but not one of the components instrumental for performing the core optical transformations in the spectrograph.

3.1.4 Collimating Lens

Placed at one collimator's focal length f_2 from the image formed by the slit, the collimating element consisting of a convex-concave lens duet is used to convert the

divergent incident light into a parallel beam directed directly towards the dispersive element (see Figure 3.5). The goal is to achieve dispersion with one single incidence angle $\alpha = 0$ for the entire beam, to ensure that spectral and spatial coherence is preserved in the process.

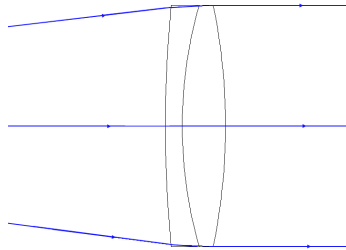


Figure 3.5: Collimating doublet lens ($f_2 = 200\text{ mm}$) of MISS (OSLO software)

3.1.5 Dispersive Element

The incident beam of parallel light passes through the dispersive element, a TGRISM, as described in 2.6.2 and following Equation 2.6.2. The beam of light of first diffraction order then emerges, with wavelengths dispersed along the vertical axis (slit width axis) and position (angular elevation) along the horizontal axis (slit length axis), as shown in Figure 3.6.

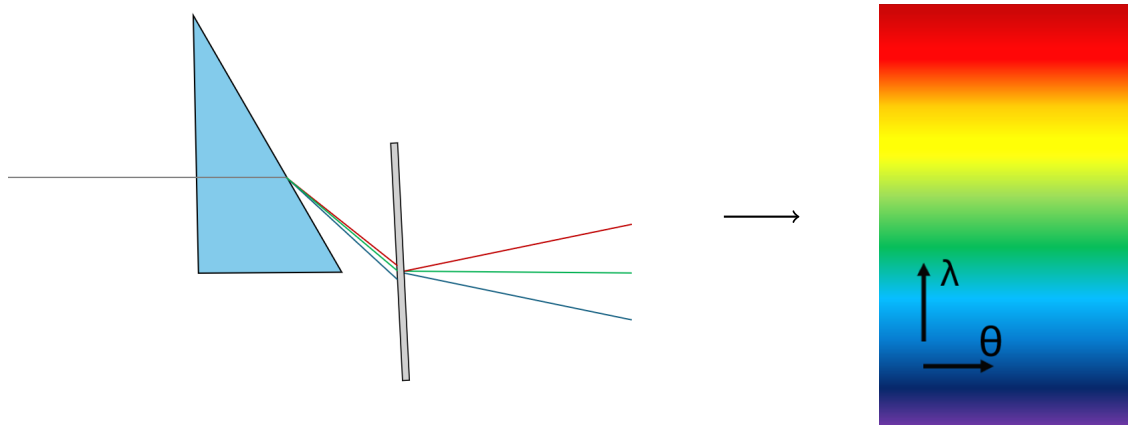


Figure 3.6: Light dispersed by MISS 2's TGRISM at Diffraction Order 1

3.1.6 Focusing Lens

The light dispersed by the TGRISM is emerging from the grating as a 10.33° wide diverging beam (rectangular solid angle) centered around the optical axis. It must be properly focused into a final image onto the spectrograph's sensor with the help of a camera focusing lens with a focal length f_3 (Figure 3.7), such that the projected image fits the surface of the sensor as closely as possible (Figure 3.10b).

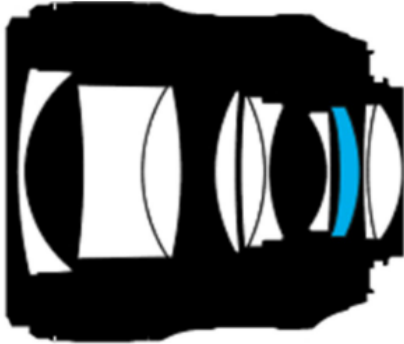


Figure 3.7: MISS 2's camera lens optical layout ($f_3 = 35\text{ mm}$)

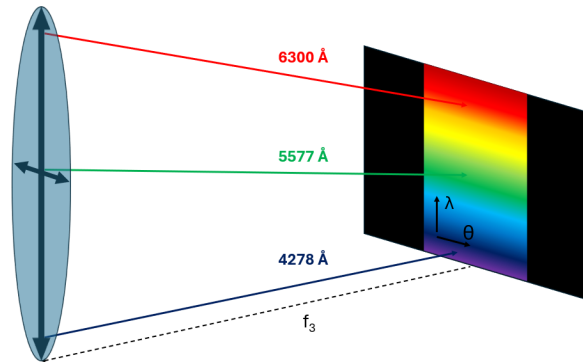


Figure 3.8: Light focused onto the sensor

3.1.7 Sensor

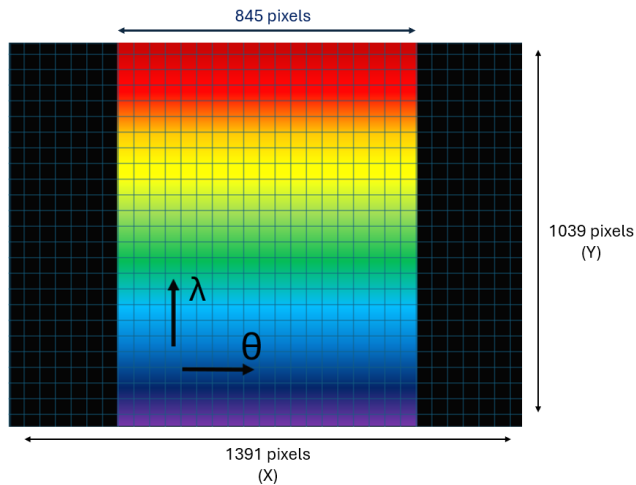


Figure 3.9: Digitised Spectrogram

MISS 2 uses a (CCD) sensor with a definition of $X \times Y = 1391 \times 1039$ pixels to capture and record spectrograms. That type of sensor works in the VIS range and is optimal for low-light condition as it offers a high SNR even at low light intensity. It is therefore suitable for aurora imaging.

It is positioned at the focal length of the camera focusing lens where it digitises the optical image of the dispersed light. For

each spectrogram capture, the entire surface S_3 taken by the hyperspectral image is converted into a grid of 1391×1039 pixels, as illustrated in Figure 3.9.

The vertical pixel axis (y-axis) shows the varying wavelengths through the entire 4000 to 7000 Å range. It therefore sets an absolute maximum of 1039 emission lines detectable within that range. Any line representing less than $\frac{3000 \text{ Å}}{1039 \text{ pix}} = 2.89 \text{ Å}$ allowed by the imager's optics would be "lost in translation" and would lead to the impossibility to resolve between two emission lines and to measure the light intensity from a specific emission line, as represented in Figure 3.10a. It is good practice to ensure the profile (width) of a single emission line over several pixels. Indeed, identifying the position of the centre (peak of intensity) of a given emission line is necessary in order to identify its corresponding wavelength with sufficient precision, as can be observed in Figure 3.10.

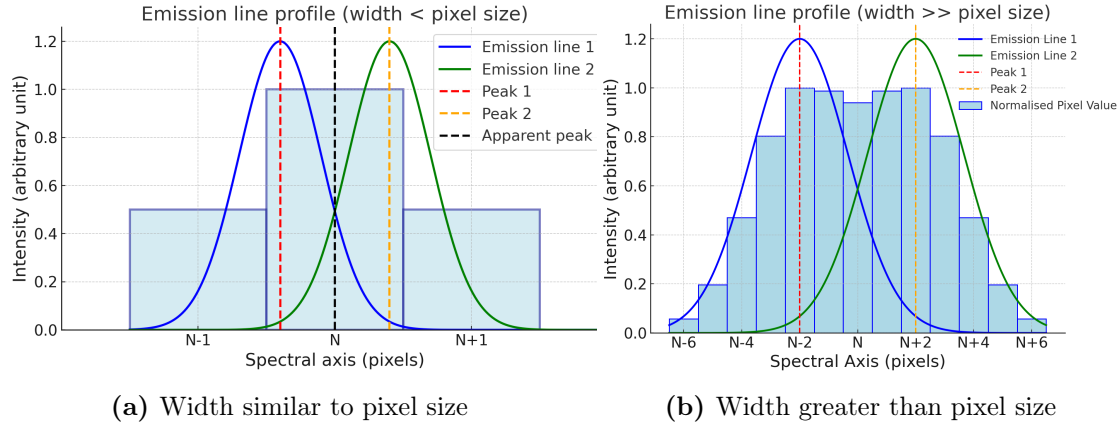


Figure 3.10: Emission lines amplitude profiles separated by $d = \text{FWHM}$.

The horizontal pixel axis (x-axis) shows the varying elevation angle through the entire -90° to 90° range. Similarly, it sets an absolute limit of 845 angular positions. But more realistically, there is no need for a finer resolution than one degree for MISS 2, which represents a resolution upper boundary of $\frac{845 \text{ pix}}{180^\circ} = 4.7$ pixels per degree.

3.2 Spectral Resolution

3.2.1 Expression of the Passband

The *spectral resolution* $\Delta\lambda$, i.e. the minimum discernible difference in wavelengths around a wavelength λ by a spectrograph's sensor is connected to the resolving power

via:

$$R = \frac{\lambda}{\Delta\lambda} \quad (3.1)$$

The spectral resolution itself is observed physically as the *bandpass* (BP), which represents the minimum identifiable width of a single diffracted emission line as captured by the spectrograph's sensor, accounting for the convolution caused by the entrance and exit slits (aperture) on an ideally monochromatic line. In practice, it is best defined as the *Full Width at Half Maximum* (FWHM) of the light intensity of a monochromatic spectral line captured by the spectrograph's sensor.

An approximation of its expression in the ideal case where the optics are perfectly well-aligned:

$$BP_{ideal} = FWHM \approx \frac{\Delta\lambda}{\Delta x} \cdot w' \quad (\text{Ideal Bandpass approximation [23]})$$

Where $\frac{\Delta\lambda}{\Delta x}$ represents the linear dispersion, i.e. the wavelength change $\Delta\lambda$ per position unit Δx on a spectrograph's detector and w' is the width of the aperture of the spectrograph.

Let us now derive an expression for BP_{ideal} using this approximation which accounts for the convolution of a single emission line with a wavelength λ through MISS 2 to make an estimation of the FWHM to be expected for a given emission line λ .

We do not have a direct mean to calculate the linear dispersion, however we can use the GRISM Equation to differentiate λ with respect to the diffraction angle θ_m and obtain an expression for the *angular dispersion* $\frac{d\lambda}{d\theta_m}$.

$$m\lambda = d [\sin(n_{BK7}(\lambda) \sin A) + \sin \theta_m]$$

$$\begin{aligned} \frac{d\lambda}{d\theta_m} &= \frac{d}{m} \left(\sin A \cdot \frac{dn(\lambda)}{d\theta_m} + \cos \theta_m \right) \\ &= \frac{d}{m} \left[\sin A \cdot \frac{d}{d\lambda} \left(A_1 + \frac{B_1}{\lambda^2} \right) \frac{d\lambda}{d\theta_m} + \cos \theta_m \right] \\ &= \frac{d}{m} \left[\sin A \cdot \left(-\frac{2B_1}{\lambda^3} \right) \frac{d\lambda}{d\theta_m} + \cos \theta_m \right] \end{aligned}$$

We can now factorise:

$$\frac{d\lambda}{d\theta_m} \left(1 + \frac{d}{m} \cdot \sin A \cdot \frac{2B}{\lambda^3} \right) = d \cdot \cos \theta_m$$

And we obtain an expression for $\frac{\Delta\lambda}{\Delta\theta_m}$:

$$\frac{d\lambda}{d\theta_m} = \frac{d \cdot \cos \theta_m}{1 + \frac{d}{m} \cdot \sin A \cdot \frac{2B}{\lambda^3}} \quad (3.2)$$

dx being an infinitesimal change on the image plane induced by a diffraction angle change $\Delta\theta_m$ between the focusing lens with focal length f_3 and the sensor, we can use the small angle approximation:

$$d\theta_m \approx \sin(d\theta_m) = \left(\frac{dx}{f_3} \right) \Leftrightarrow d\theta_m = dx/f_3$$

So we can write:

$$\frac{d\lambda}{dx} = \frac{d \cdot \cos \theta_m}{f_3 \left(1 + 2 \cdot \frac{d}{m} \cdot \sin A \cdot \frac{B_1}{\lambda^3} \right)} \quad (3.3)$$

- Expression for $\boxed{w'}$

Here, we need to express the exit aperture w' as a function of the entrance aperture (slit width w), which is a known parameter. To achieve this, we need to introduce the *étendue* G of an optical instrument, defined as the projection of the solid angle of the light admitted onto a surface or optical component:

$$G = \pi S \sin^2 \Omega \quad (3.4)$$

With $\pi \sin^2 \Omega$, the solid angle formed by the light admitted into or out of a slit and S , the surface the admitted light projects onto.

In a spectrograph, we have G_2 , the input *étendue* - i.e. spread of the entire light admitted through the entrance slit onto the collimating lens L_2 -, and G_3 the output *étendue* - i.e. spread of the light focused onto and admitted by the exit slit (portion of the spectrograph's sensor onto which the light is focused). Considering the *étendue* constant throughout the entire instrument, i.e. without any obstruction, we can write:

$$G_2 = G_3 \Rightarrow \left(\frac{G_A \cos A}{f_2^2} \right) \cdot (Lw') = \left(\frac{G_A \cos \theta_m}{f_3^2} \right) \cdot (L'w)$$

And thus:

$$w' = \left(\frac{\cos A}{\cos \theta_m} \right) \cdot \left(\frac{f_3^2}{f_2^2} \right) \cdot \left(\frac{L}{L'} \right) \cdot w \quad (3.5)$$

Where L is the entrance slit length and L' is the exit slit length

Knowing that $L/L' = f_2/f_3$ by definition, we can simplify as follows to obtain the expression of the slit width magnification:

$$w' = \left(\frac{\cos A}{\cos \theta_m} \right) \cdot \left(\frac{f_3}{f_2} \right) \cdot w \quad (3.6)$$

Using the new expression for both parts of the expression of BP, we get:

$$BP_{ideal} = \frac{d \cdot \cos \theta_m}{f_3(1 + 2 \cdot \frac{d}{m} \cdot \sin A \cdot \frac{B_1}{\lambda^3})} \cdot \left(\frac{\cos A}{\cos \theta_m} \right) \cdot \left(\frac{f_3}{f_2} \right) \cdot w$$

And finally:

$$BP_{ideal} = \frac{d \cdot \cos A}{f_2(m + 2 \cdot d \cdot \sin A \cdot \frac{B_1}{\lambda^3})} \cdot w \quad (3.7)$$

3.2.2 Application for MISS 2

With the help of the equation for BP_{ideal} obtained in 3.3.1. we can now compute estimations of BP_{ideal} of MISS 2 as a function of the wavelength λ and we obtain the curve in Figure 3.11.

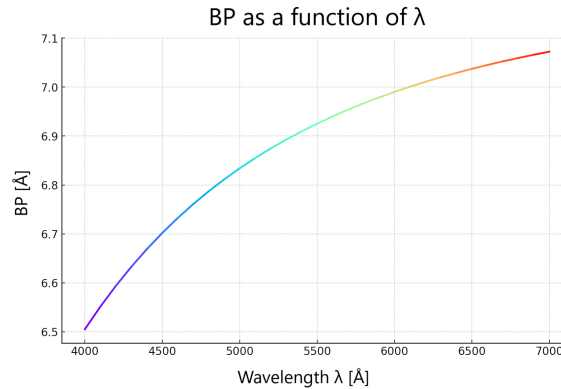


Figure 3.11: Passband (BP) as a function of the wavelength (λ)

In practical terms, we have $BP_{ideal} \leq BP_{real}$. As illustrated in Figure 3.12, any imperfection or misalignment of the optical components, or source of uncertainty on the slit width may make BP_{real} significantly greater.

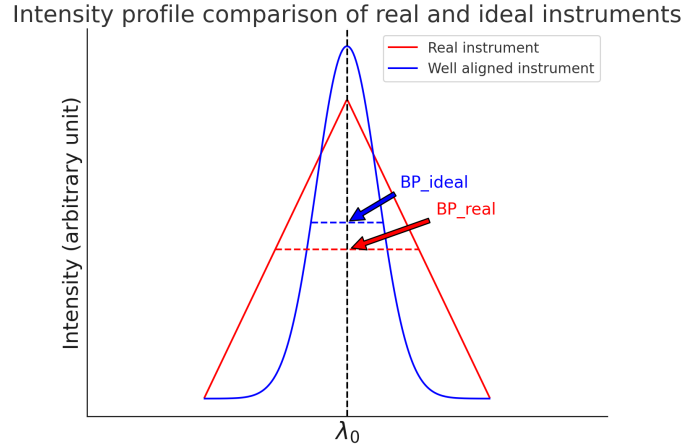


Figure 3.12: Comparison of BP_{ideal} and BP_{real} (triangular, pixelated profile)

Figure 3.11 shows an increasing trend of BP_{ideal} for increasing wavelengths, which implies that the FWHM observed on a spectrogram captured by MISS will be greater towards the red range and minimal around 4000 \AA . Ranging from about 6.5 \AA to 7.1 \AA , the values are well within the 1 nm -spectral resolution required for a single spectrogram to contain up to 300 discernible emission lines ranging from 4000 \AA to 7000 \AA . In other words, we may be able to get close to a 1 nm spectral resolution in practical applications.

3.3 Spatial Resolution

3.3.1 Spatial Resolution of a Hyperspectral Imager

Hyperspectral imagers are commonly used as remote sensing payload instruments on-board satellite, spacecraft, aircraft or unmanned aerial vehicles (UAV) for the imaging of the Earth's surface. For such purpose, they capture spectrograms continuously while in movement relatively to the ground, which allows the collection of spectral data across a two-dimensional source along the x-axis (flight direction) and the y-direction (normal to the flight direction).

The *spatial resolution* is then defined as the size of the smallest feature discernible on a spectrogram along the x-axis, Δx and along the y-axis, Δy .

- Resolution Δx

In order to derive an expression for Δx , we need to first take into account the *angular spread* $\alpha_S = \frac{w}{f_1}$. It is best described as the **FOV** along the x-axis induced by the entrance slit width and inversely proportional to the front lens focal length, which represents an angular overlap on every spectrogram and projects on the ground as the ground segment dx_{optics} , expressed as $dx_{optics} = z \cdot \alpha_S$, using the small angle approximation. And thus:

$$dx_{optics} = z \cdot \frac{w}{f_1} \quad (3.8)$$

Adding up to the ground segment $dx_{optical}$, is the further resolution limitation segment dx_{motion} induced by the velocity v at an altitude z away from the ground during a single capture's exposure time t_{exp} such that:

$$dx_{motion} = v \cdot t_{exp} \quad (3.9)$$

The resulting Δx is then simply a sum of both these two segments:

$$\Delta x = \frac{z \cdot w}{f_1} + v \cdot t_{exp} \quad (3.10)$$

Here, we neglect the read out time τ between two consecutive image captures, considering an application where $dx_{optical} > v \cdot \tau$ implying that two consecutive images have a sufficient overlap to avoid having any missing portion of the target area.

Similarly to Δx , the resolution along the slit v , Δy , depends on the optics (front-lens and slit length L), but also on the amount of pixels N along the horizontal dimension axis of the **CCD** camera - a greater N will logically allow smaller features to be discernible on the spectrogram, along the spatial y-axis.

$$\Delta y = dy_{optics} = \frac{z \cdot L}{N \cdot f_1} \quad (3.11)$$

3.3.2 Application for **MISS 2**

- **Spatial Resolution**

As opposed to a spectrograph used for remote sensing of the surface of the Earth, the **MISS 2** imager is to be operated in an observatory, aimed at the sky and therefore

static relatively to the ground. It scans a thin section of the sky along the entire geomagnetic continuously and as such, it is the sky itself which is in movement relative to **MISS 2**, at a velocity equal to the speed of rotation of the Earth at the imager's location. However, the atmosphere's angular speed matching that of the Earth, we can consider it static with respect to it. Instead, it is the movements of the aurora across the magnetic meridian that is monitored by the spectrograph.

Further, in lieu of an altitude above ground level, we are now considering a *slant range* z between **MISS 2** and the source, which may vary significantly considering the fact that the range of altitudes h of the aurora can span from 80 km to over 600 km. However, considering that atomic oxygen (1S) green (5577 Å) aurora usually occurs between 100-150 km, atomic oxygen (2D) red (6300 Å) aurora between 200-300 km and molecular nitrogen ion (N_2^+) blue-violet (4278 Å) between 80-100 km, we will focus on a [80 - 300 km] range, taking also into account the *angle of elevation* ρ , relative to the position of **MISS 2**.

Parameters for **MISS 2**:

- ▶ **Elevation angle:** $-90^\circ \leq \rho \leq +90^\circ$
- ▶ **Slant range:** $z = \sqrt{R_E^2 + (R_E + h)^2 - 2R_E(R_E + h) \cdot \cos \rho}$ [32]
- ▶ **Altitude range:** $80 \text{ km} \leq h \leq 300 \text{ km}$
- ▶ **Exposure time:** $t_{exp} = 12 \text{ s}$
- ▶ **Focal length of the front-lens:** $f_1 = 8 \text{ mm}$
- ▶ **Slit width:** $w = 0.1 \text{ mm}$
- ▶ **Slit length:** $L = 24 \text{ mm}$
- ▶ **Number of pixels along the spatial dimension:** $N \approx 845 \text{ pixels}$

We deduce the new expressions for Δx and Δy :

$$\begin{cases} \Delta x(\rho) = \sqrt{R_E^2 + (R_E + h)^2 - 2R_E(R_E + h) \cdot \cos \rho} \cdot \frac{w}{f_1} \\ \Delta y(\rho) = \sqrt{R_E^2 + (R_E + h)^2 - 2R_E(R_E + h) \cdot \cos \rho} \cdot \frac{L}{N \cdot f_1} \end{cases}$$

At zenith ($\rho = 0^\circ$), we get the following estimation intervals:

$$1.00 \text{ km [80 km]} \leq \Delta x_0 \leq 3.75 \text{ km [300 km]}$$

$$293 \text{ m [80 km]} \leq \Delta y_0 \leq 1.07 \text{ m [300 km]}$$

Plotting Δx and Δy across the entire FOV of MISS 2, we obtain the curves in Figure 3.13. We observe a significant increase for high $|\rho|$, as expected.

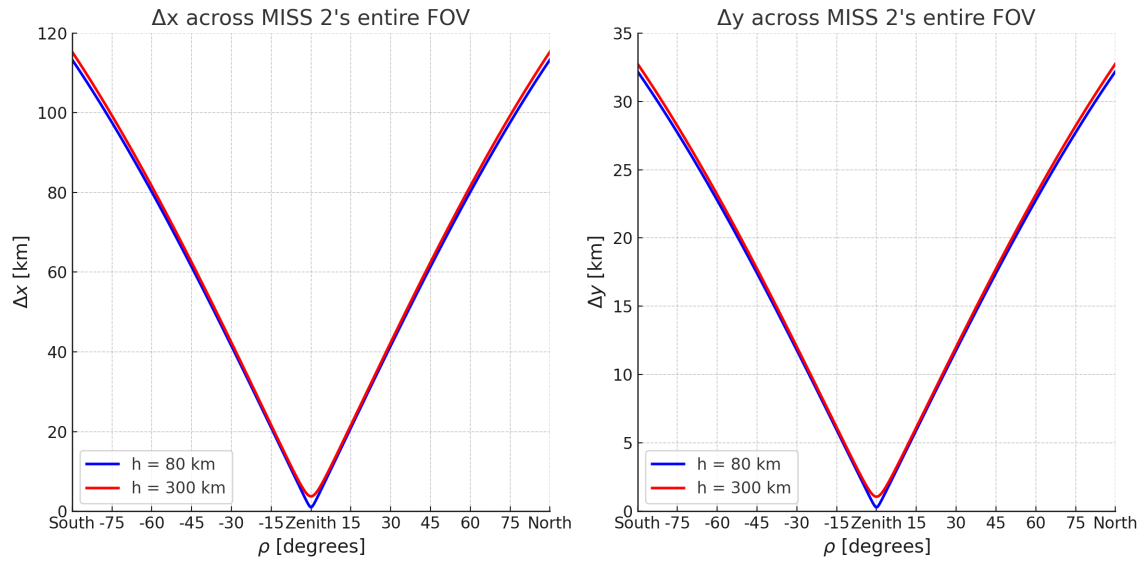


Figure 3.13: $\Delta x(\rho)$ and $\Delta y(\rho)$ for $h = 80 \text{ km}$ and 300 km

However, Δx and Δy represent apparent segments, and not the object's size as observed directly from below ($\rho = 0$). For an estimation of the size of the smallest object MISS 2 can distinguish projected onto the corresponding horizontal section of the sky, we can introduce Δx_{PROJ} and Δy_{PROJ} , the projected linear projection of the spatial resolutions which can be approximated as:

$$\Delta x_{PROJ} \approx \frac{\Delta x}{\cos \rho} \quad \text{and} \quad \Delta y_{PROJ} \approx \frac{\Delta y}{\cos \rho} \quad (-90^\circ < \rho < 90^\circ) \quad (3.12)$$

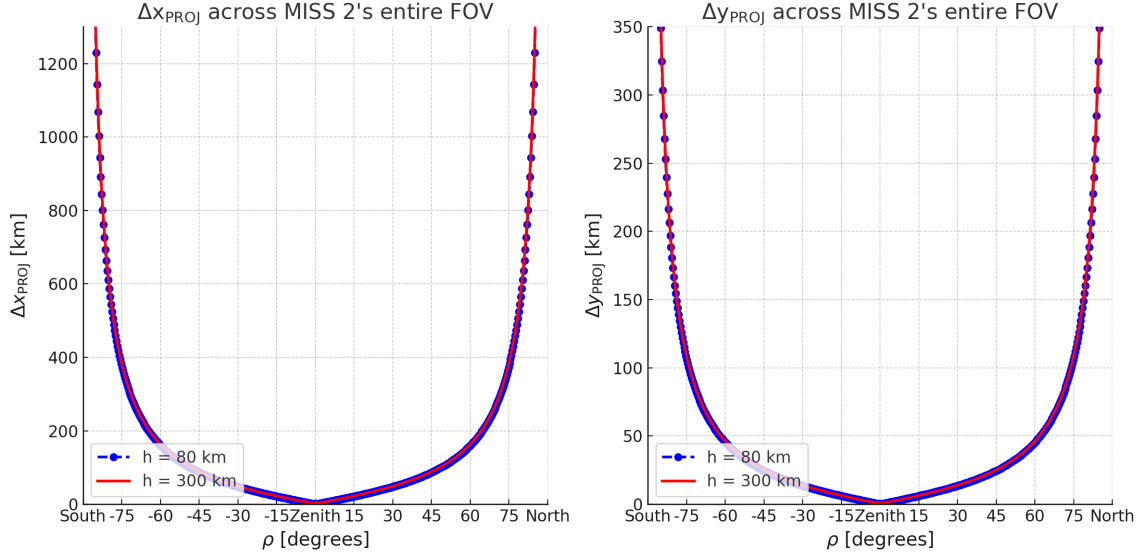


Figure 3.14: $\Delta x(\rho)$ and $\Delta y(\rho)$ for objects at $h = 80$ km and 300 km

Visualising this projection of the spatial resolutions in Figure 3.14, it comes that the actual minimum size discernible Δx is showing a steep increase near the horizons, implying that depending on the size of the feature of interest, it might not be detected beyond a certain elevation angle $\pm\rho$. Likewise, a steep increase of Δy suggests a limited spectral resolution at elevation angle close to the horizons (Asymptotes at $\rho = -90^\circ$ and $+90^\circ$).

3.4 Angular Resolution

Let us define the angular resolution components δ_x and δ_y as the smallest angles allowing to resolve a single features optically along the plane of the slit width (x-axis) and along the plane of the slit length (y-axis) respectively. We can simply express them as follows:

$$\delta_x = \frac{\Delta x(\rho)}{z(\rho)} = \frac{w}{f_1} [rad] \quad \text{and} \quad \delta_y = \frac{\Delta y(\rho)}{z(\rho)} = \frac{L}{N \cdot f_1} [rad] \quad (3.13)$$

From which we deduce the following values for MISS 2:

$$\delta_x = 0.713^\circ \quad \text{and} \quad \delta_y = 0.203^\circ$$

The interpretation of these values is that if we take a single spectrogram [x: λ , y: ρ , z: Intensity] capturing the intensity for each wavelength λ within $400 - 700$ nm along the x-axis as a function of the elevation angle ρ along the y-axis:

- The ideal angular resolution across the slit width is $\delta_x = 0.713^\circ$ across the entire $FOV = 180^\circ$. Realistically, we can therefore consider that we fulfill a condition $\delta_x(reel) \approx 1^\circ$, which accounts for imperfections and misalignment.
- The angular resolution across the slit length is $\delta_y = 0.203^\circ$. It represents an angle uncertainty across the y-axis of the spectrogram (λ) which itself has an impact on spectral resolution.

3.5 Slit Length and Width Magnification

For the design of a spectrograph, it is important to determine the dimensions of the spectrogram to capture (surface S_3), in order to ensure that the spectrogram size fits the surface of the CCD. We can use the coefficients of *magnification* of the slit length L and width w respectively, which represent the coefficients by which the resulting exit slit length L' and width w' are formed on the CCD. The slit width is magnified by the grating upon dispersion, and both the slit width and length are first magnified by the collimating lens f_2 and then, de-magnified by the focusing lens f_3 .

If we consider the full angular dispersion $\Delta\theta_m = 10.33^\circ$ from MISS 2's TGRISM, we can simplify the expression for the exit slit w' :

$$L' = \left(\frac{f_3}{f_2}\right) \times L \quad \text{and} \quad w' = \Delta\theta_m \times f_3 \quad (3.14)$$

$$\begin{cases} L' = 4.20 \text{ mm} \\ w' = 6.30 \text{ mm} \end{cases}$$

So, we have: $S_3 = 4.20 \text{ mm} \times 6.30 \text{ mm}$

Let us verify that the dimensions of the CCD match the surface S_3 . The CCD has a resolution of 1391 pixels \times 1039 pixels. Given a pixel pitch of $6.45 \mu\text{m}$, the dimensions of the CCD are:

$$S_{CCD} = 1391 \cdot 6.45 \mu\text{m} \times 1039 \cdot 6.45 \mu\text{m} = 8.97 \text{ mm} \times 6.70 \text{ mm}$$

The dimensions of the CCD are indeed compatible with the image of surface S_3 in any orientation as both the image's width and length fit within both pixel axes.

3.6 Transmission Efficiency

For a spectrograph designed to capture faint light intensity such as MISS 2, another important parameter is its capacity to allow the transmission of a sufficient portion

of it to be detected by its sensor. Each optical component along the optical path has a transmittance below 100%, some of which, show significant variations in function of the wavelength within the visible range.

Transmittance for each optical component as well as the two UV fused silica windows used to isolate and protect the dispersive element, for $\lambda \approx 5500 \text{ \AA}$ (Provided by constructors or external source):

- Peleng All-sky lens 8 mm (Belomo): $T_1 = 0.7$ [33]
- Field lens 50 mm (Edmund Optics): $T_F = 0.9825$ [34]
- Achromatic collimating lens 200 mm (Thorlabs): $T_2 = 0.995$ [35]
- BK7 glass prism (Altechna Co.): $T_{BK7}(\lambda = 5500\text{\AA}) \approx 0.996$ [36]
- Grating 600 lines/mm (blazing: 28.7°): $T_G(\lambda = 5500\text{\AA}) \approx 0.56$ [37]
- Nikkor objective 50 mm (Nikon): $T_3 = 0.605$ [38]
- UV fused silica windows: $T_{w1} = T_{w2} = 0.995$ [39]

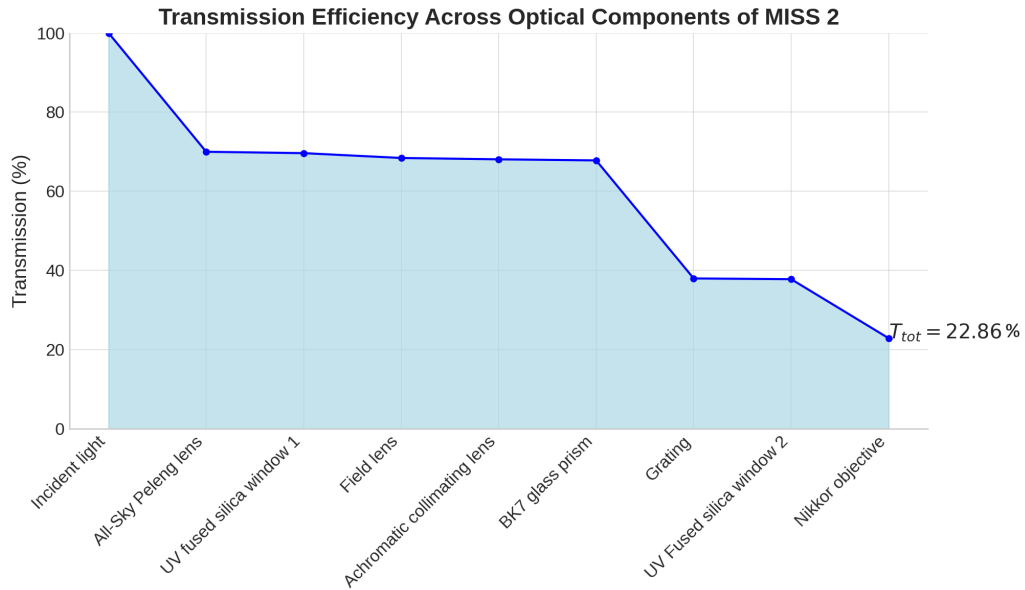


Figure 3.15: Transmission efficiency of MISS 2

The overall transmission efficiency T_{tot} of the instrument (ie. portion of the incident light intensity reaching the sensor) is expressed following the path of light through respective components and as illustrated in [Figure 3.15](#):

$$T_{tot} = T_1 \times T_F \times T_2 \times T_{w1} \times T_{BK7} \times T_G \times T_{w2} \times T_3 \quad (3.15)$$

$T_{tot} = 22.86\%$, which is significantly lower than the transmission efficiency of a regular camera due to the additional optics required. A longer exposure time is therefore required to allow a similar photon flux onto the [CCD](#) sensor, which has implications for the time resolution of hyperspectral imaging in low-light conditions.

4 Components and Assembly



Figure 4.1: KHO, Longyearbyen

In Chapter 3, the optical design used for the MISS 2 imager was presented, along with the role of its optical components and the instrument's relevant characteristics. This present Chapter serves as a summary of the construction and adjustment processes of the MISS 2 project.

MISS 1 and MISS 2 (cf. Figure 4.3) were both designed and assembled at UNIS (Figure 4.1). MISS 1 seen in Figure 4.2, is operated at KHO (78.15°N, 16.04°E),

on the top of Breinosa, a conveniently plateau-shaped mountain about 15 km away from the centre of Longyearbyen, whereas MISS 2 will be operated at the Ny-Ålesund Research Station (78.91°N, 11.88°E), some 110 km or a 25 minutes flight away from Longyearbyen. The principle is that they perform the tracking in the same way, providing two sets of data of the same type, which may then allow comparative studies. Improvements were made on the hardware for MISS 2 (front lens protection shutter and structural reinforcement). All components required to build MISS 2 are listed in *Appendix A*.



Figure 4.2: MISS 1 in operation at KHO



Figure 4.3: MISS 1 (left) and MISS 2 (right)

4.1 Optical Component Specifications

4.1.1 Transmitting Grating

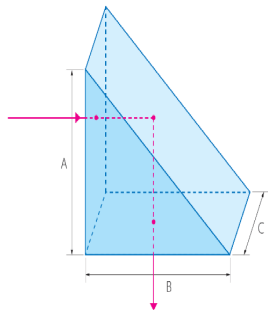


Specifications	
Model	GT50-06V
Manufacturer	Thorlabs
Groove Density	600 lines/mm
Blaze Angle	28.7°
Dimensions	50 mm x 50 mm
Material	Schott B270

Figure 4.4: Transmission grating and specifications from ThorLabs.

About: 600 lines/mm grating, chosen for balance between spectral resolution and transmission efficiency (cf. 2.5.4). Blaze angle of 28.7° for maximised first diffraction order in VIS (cf. 2.5.3).

4.1.2 Littrow Prism



Specifications	
Prism Type	Right-angle Littrow prism
Manufacturer	Altechna Co., Ltd
Material	BK7
Surface Flatness	$< \lambda/10$ @ 632.8 nm
Dimensions (A x B x C)	50 mm x 28.87 mm x 50 mm
Apex	30°
Right Angle Tolerance	± 5 arcsec

Figure 4.5: BK7 prism and specifications from Altechna Co., Ltd.

About: BK7 glass offers a high transmission efficiency in VIS. The characteristic non-linear prism light dispersion keeps the dispersed light near the on-axis direction while exiting the TGRISM quasi-linearly.

4.1.3 Lenses

- All-sky Lens

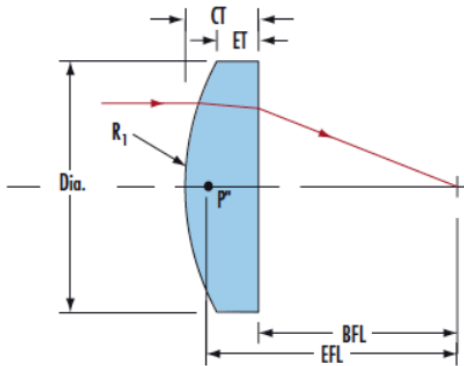


Specifications	
Model	Peleng Fisheye
Manufacturer	Belomo
Mount Type	Nikon F-Bayonet
Focal Distance	8 mm
Relative Aperture	f/3.5 - f/16
Field of View	180°
Flange Focal Distance	44 mm
Focusing Limits	0.22 mm - ∞
Diameter	73 mm
Length	65.5 mm
Weight	0.4 kg

Figure 4.6: All-sky Peleng 8 mm and specifications from Belomo.

About: Provides a 180° FOV, covering the entire hemispheric sky. Its maximum aperture of f/3.5 allows for adequate light flux in low-light conditions.

- Field Lens



Specifications	
Lens Type	Plano-Convex Uncoated
Manufacturer	Edmund Optics
Diameter	50 mm
Effective Focal Length (EFL)	50 mm
Back Focal Length (BFL)	43.28 mm
Centre Thickness (CT)	12 mm
Convex radius (R_1)	39.2 mm
Edge Thickness (ET)	7.39 mm

Figure 4.7: Field lens 50 mm and specifications from Edmund Optics.

About: Plano-convex lens, converges the light from the image formed by the slit towards the collimator at a back focal length (BFL) distance of 43.28 mm ± 1 mm from the back of the lens.

- Collimator



Specifications	
Model	AC508-200-A
Manufacturer	Thorlabs
Focal Length	200 mm
Focal Length Tolerance	$\pm 1\%$
Diameter	50 mm
Spherical Surface Irregularity	$\lambda/4$

Figure 4.8: Collimator 200 mm and specifications from Thorlabs.

About: Collimates the light with minimal optical aberration. It has a $\pm 1\%$ focal length tolerance, which represents a 4 mm interval.

- Focusing Lens



Specifications	
Model	Nikkor
Manufacturer	Nikon
Mount Type	Nikon F-Bayonet
Focal Length	35 mm
Maximum Aperture	f/1.4
Minimum Aperture	f/16
Format	FX/35mm
Weight	0.4 kg

Figure 4.9: Nikkor 35 mm focusing lens and specifications from Nikon.

About: Sharp focus of the dispersed light to form the final image of the full spectrogram. Max aperture of f/1.4, allows high light intake.

4.1.4 Sensor Specifications



Specifications	
Model	Atik 414EX
Manufacturer	Atik Cameras
Sensor	Sony ICX825 CCD
Resolution	1391 x 1039 pixels
Pixel Pitch	6.45 μm
Full Well Capacity	18,000 e-
Read Noise	4 e- (typical)
Dark Current Noise	0.001 e-/s @ -10°C
ADC	16 bit
Backfocus Distance	13 mm \pm 0.5
Exposure Range	1 ms - unlimited

Figure 4.10: Atik 414EX camera and specifications from Atik Cameras.

About: High sensitivity CCD sensor with 1391 \times 1039 (full-frame) resolution and low noise performance. 16-bit ADC (Analogue to Digital-Convertor) capture slight changes in light intensity. Suitable for long exposures due to low dark current noise.

4.1.5 Front Lens Protection Shutter Specifications



Specifications	
Model	SunShield 1
Manufacturer	Keo Scientific
Dimensions	18 cm x 17 cm x 14 cm
Weight	0.7 kg
Mounting Screw Torque	1 N-m
Power Input	100 – 240 VAC; 50/60 Hz, 0.9 A
Operating Temperature	+5°C to +60°C

Figure 4.11: SunShield 1 specifications from constructor.

In short: Protects the front lens from direct sunlight when MISS 2 is not operational. Screw torque shutter engine (defaults as open). Complete with its controller box (22 cm \times 17 cm \times 6 cm).

4.2 Mechanical Structure

The mechanical structure of *MISS 2* is designed to ensure that the instrument's optical and electronic components can perform in correct alignment, while protecting the components from environmental factors and stray light.

The key mechanical components include the slit, essential practical component of our spectrograph, a *GRISM* house for the prism and transmitting grating which includes a tuner for the grating, lens tubes of various sizes connecting the optical components, which are combined and can be adjusted and fine-tuned to match the exact distances required between the instrument's various components. The assembly of all these elements form the instrument's one piece optical tube assembly (*OTA*), which is mounted on an aluminium breadboard. For clarity, this section uses an exploded view of *MISS 2*'s structure, created with the help of a *CAD* (Computer-Aided Design) and shown in [Figure 4.12](#).

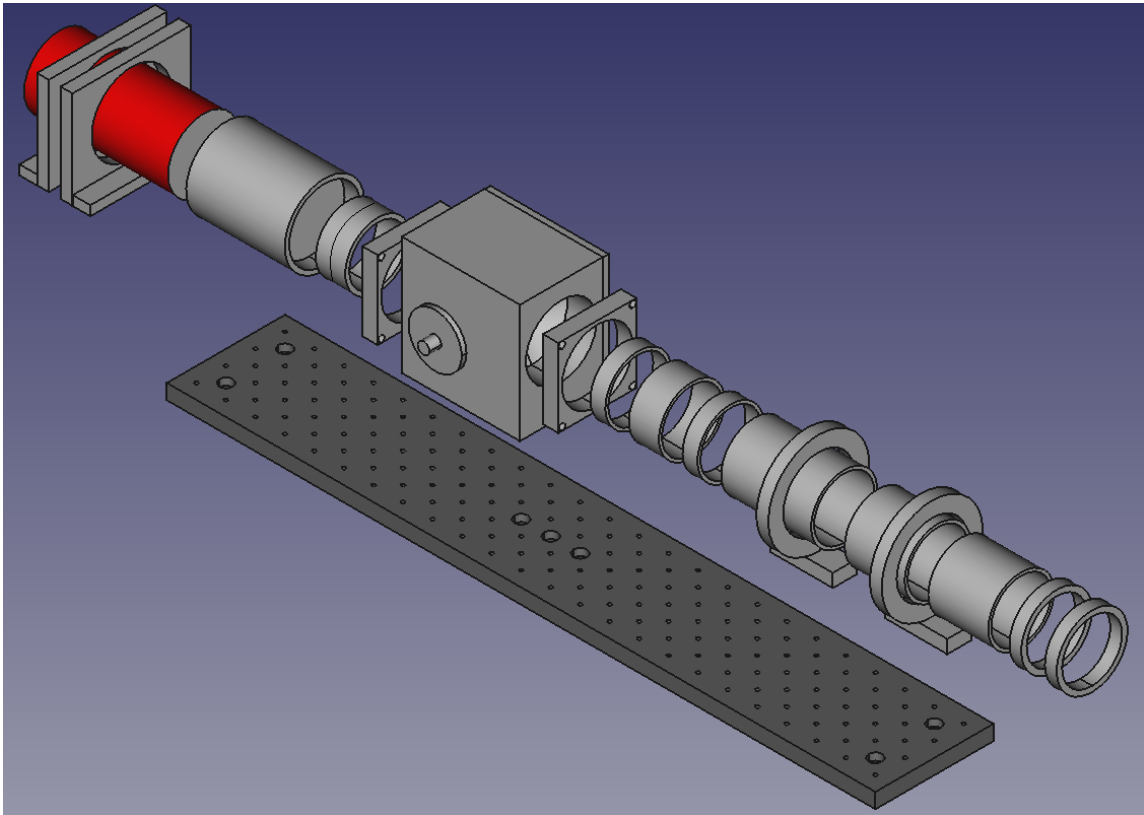


Figure 4.12: 3D Exploded View of *MISS 2*'s *OTA*. (Model created using FreeCAD)

4.2.1 Assembly Protocol

The key parts of the structure are shown in Figure 4.13.

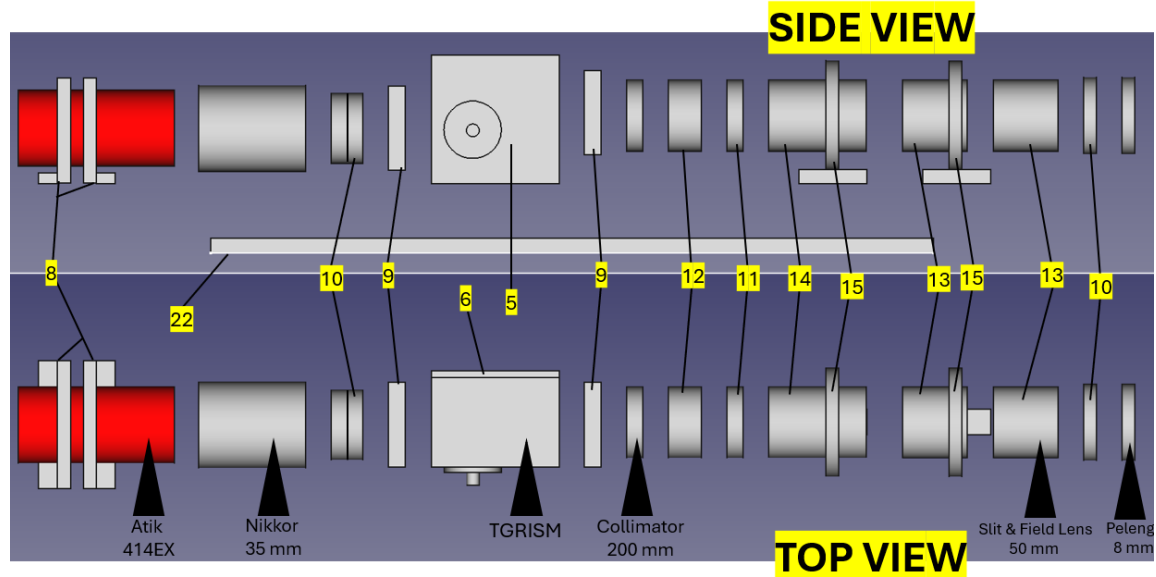


Figure 4.13: Side and Top Views of MISS 2's OTA

From left to right and as listed in *Appendix A*:

(8) - Camera Mount. (22) - Breadboard. (10) - Nikon F-Mount Adapter. (9) - SM2 Tube Adapter Plate. (6) - Grism Lid. (5) - GRISM Lid. (12) - Lens Tube 1.00". (11) - Lens Tube 2.00". (14) - Lens Tube 3.00". (15) - Clamp for SM2 Tube. (13) - Lens Tube 2.00".

Main steps of the assembly:

- **TGRISM House Assembly (5):**

This sturdy component is custom-made by eMachineShop.com. It is sealed with a tight lid (6) screwed onto it, which allows the access to the space reserved for the prism, which can be stuck to its designated space and the grating (23), which is placed on a grating holder (1) designed to allow it to be tilted via an external tuner. The GRISM house is then mounted onto the breadboard (22), forming the base of the instrument's structure.

- **Atik 414EX + Nikkor 35 mm Assembly:**

The Atik CCD sensor with its complementary Nikkor camera lens, fully equipped with its power supply and controlled via a USB connection using the manufacturer’s software, Artemis, form a fully operational CCD camera. The lens is connected to the sensor’s T2-thread mount using an SM2 coupler external thread (18).

- **Spectrograph Front Part Assembly:**

One can start by connecting the front-lens (27) to the slit house (3). The slit house contains the steel blade slit (4) adjusted to a width of 0.1 mm with the help of a feeler gauge, as well as the field lens (25). The slit house is in turn connected to the mounted collimating lens (20) using a series of SM2 lens tubes represented in Figure 4.12 (11, 12, 13 and 14). Additionally, an adjustable internal lens tube (17) is added, for fine-tuning of the slit alignment and to reach focal point precisely.

- **Front and Back Part Installation:**

The front part of the instrument is mounted using 2 lens tube clamps (15) fixed onto the board via custom 3D printed bases. The back part, which includes the Atik-Nikkor setup, is also mounted onto the board with the help of a custom 3D printed camera mount (8) screwed in the board. Both cylindrical sides are conceived to allow rotation about their longitudinal axis for adjustment and fine-tuning. Both ends are connected to the central GRISM house, hermetically shut with the help of two UV fused silica windows (24), using SM2 adapter plates (9) connected to the Nikkor lens via a Nikon F-mount adapter (10).

4.2.2 Front-Lens Mechanical Shutter Integration

The SunShield front-lens mechanical shutter is the main new feature of MISS 2, added to protect the front-lens and allow operation in regions and periods of the year with significant daylight without damaging the instrument’s sensitive components. After exploring various designs to adapt to the shutter support’s geometry while ensuring it could withstand the repeated shocks from the shutter’s activation, the decision was ultimately made to fix it directly to the breadboard via a suitable custom-made support. This might simplify the challenge of designing a stress-resistant adapter.



Figure 4.14: Left: Equipment required to operate the SunShield [40] Right: Own Design Suggestion, 3-piece interlocking aluminium SunShield adapter fixed onto the breadboard. (Model created using FreeCAD)

*As of September 2024, the shutter has not been mounted yet and **MISS 2** shall enter its testing phase without it for the season 2024/25.*

4.2.3 Fine-Tuning Stages

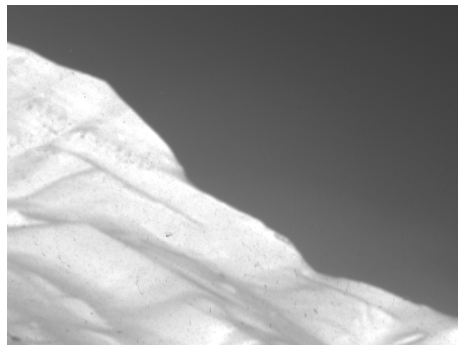


Figure 4.15: Sharp image "at infinity" of Hiortfjellet, a local landmark.

- **Focusing the CCD camera:**

Achieving a sharp, well-focused imaging of the light dispersed by the instrument requires the camera-lens duo to be focused to infinity. This crucial step is best carried out prior to assembly. It can be done via iterative adjustments of the

distance separating the sensor's CCD surface and the camera lens until a sharp image of a source at infinity (distant feature, stars in a night sky...) can be obtained (see sharp image at infinity in Figure 4.15). The Nikkor lens itself remains on infinity (∞) setting. While the Atik 414EX CCD camera cannot record videos, the Artemis software controlling it can be configured to capture images in a loop with customised exposure times and settings. When focus to infinity is obtained, the distance camera-lens can be locked with the coupler external threaded ring.

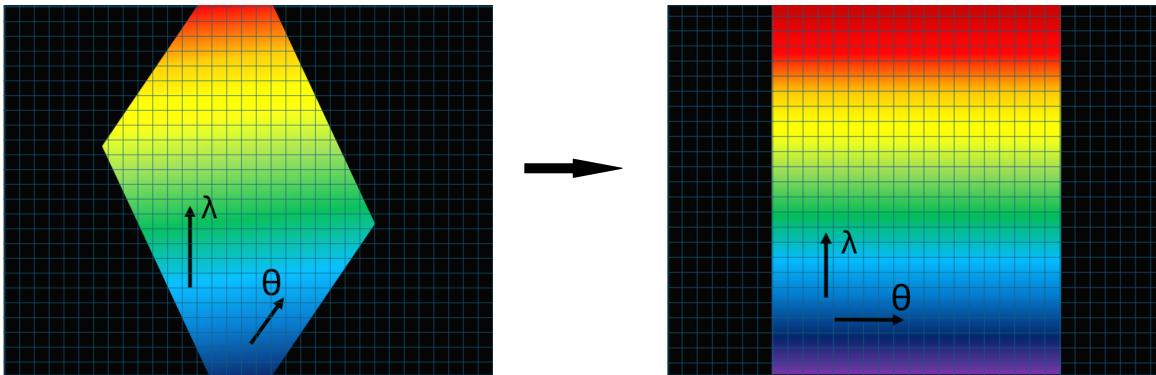


Figure 4.16: Illustration - spectrogram before (left) and after slit-alignment (right).

- **Slit-Alignment and Collimation Focal Length:**

After the back and front parts of the instrument are installed, the camera should be set in an upright orientation to capture spectrograms with spatial and spectral axes aligned to the horizontal and vertical sides of the image. Once aligned, the camera can be secured on the camera mount. The front part can also be installed and all elements adjusted until only the adjustable internal lens tube can be rotated freely, with the lens tube clamps open. At this point, the instrument has effectively become a spectrograph.

In order to resolve the light collimated by the collimating lens, one can now capture spectrograms using the loop imaging feature. Spectral lines from a chosen source (e.g. a low pressure gas discharge lamps) can be observed and, using successive 180° increments starting from outside the focal distance, the first objective is to reach the distance with the sharpest and brightest emission lines, which is a sign that the collimation is performed correctly.

After achieving proper collimation, the second objective is slit-alignment. It

consists in fine-tuning the internal lens tube precisely until the emission lines observed are exactly horizontal on the spectrograms (cf. Figure 4.16). It is necessary to refer to the central portion of the spectrograms where optical distortions - *smile* along the spectral axis causing curvature and *keystone* along the spatial axis causing trapezoidal deformation - are more subtle. Once alignment is obtained, the internal lens tube can be locked with the help of an external threaded coupler ring.

- **Tunable Grating Adjustment:**

The last stage of fine-tuning involves adjusting the tilt angle of the transmission grating in order to ensure the capture of the entire VIS, around the greens range (5500 Å). Based on the theoretical value of the tuning required estimated in 2.6.2, the surface of the grating should be positioned in a nearly upright position (perpendicular to the plane of the breadbord), and then more finely tuned with the visual of the spectrograms of known emission sources in the green range until that green line is centered. Once a satisfactory centering is obtained, the grating tuner is fixed, completing the assembly of the spectrograph.

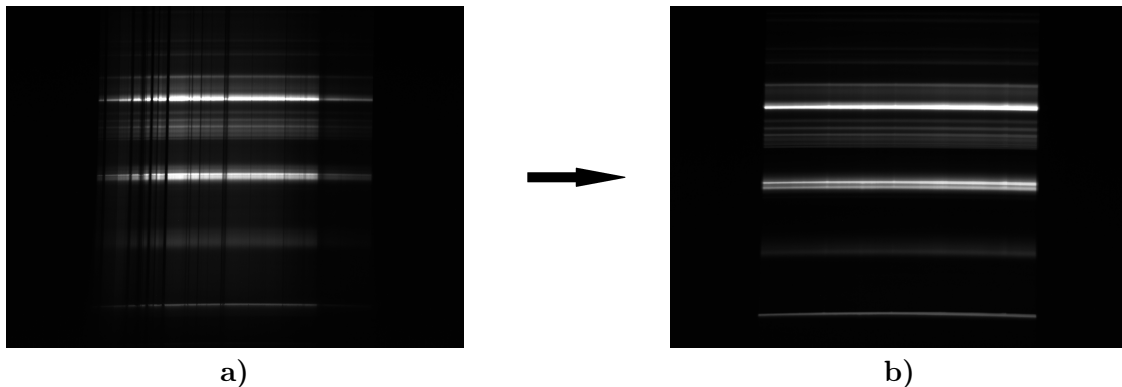


Figure 4.17: Spectrogram with a dusty slit (a) and spectrogram after slit de-dusting at the Electronic Workshop of UNIS using a pressurised air gun (b).

- **De-dusting of the Slit:**

The thin slit opening is letting the entirety of the light through the instrument's optical system. It is exposed to ambient atmosphere during the construction process, especially during the adjustment of the spacing between its two blades,

which implies that tiny dust particles of even a fraction of the 0.1 mm slit width might obstruct portions of the slit. This issue is revealed on the spectrograms captured, which show entire missing or significantly attenuated portions of the FOV. It is therefore necessary to de-dust the slit carefully, using a pressurised air gun. Once each portion of the entire FOV has a continuous spectrum (see Figure 4.17), the spectrograph is fully assembled and ready for calibration.

4.3 Imager Fully Assembled

Once fully assembled and tuned, MISS 2 is a one-piece instrument, with its entire structure secured to the breadboard. It can withstand being aimed towards any orientation, including the required upright position towards Zenith. The sides are marked with geomagnetic South and North orientations.

When entering calibration phase, it is crucial that no further adjustment is made to any component, as it may not only compromise the instrument's alignment but also the validity of the calibration itself. Under operation, it will face structural, mechanical and digital de-calibration, which is why calibration shall be repeated at least yearly.

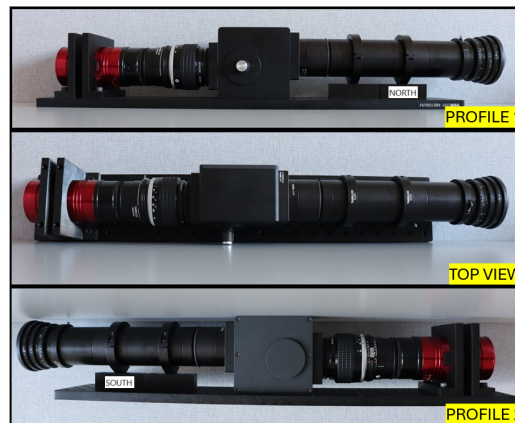


Figure 4.18: Views of MISS 2 mounted and fine-tuned.
(Cf. *Appendix B* for larger scale views)

5 Software Design

5.1 MISS 2.0: Purpose and Functionalities



Figure 5.1: AI-generated program icon for the new MISS software, using own picture of an emblematic Svalbard traffic sign.

This Chapter aims at offering a clear and detailed description of the entire software suite used to handle automated aurora tracking with a MISS imager, and process the data sampled for informative visuals of the auroral activity. Special attention has been given to preserving the integrity of the data collected and following a data management guideline, allowing their use for any scientific purpose.

The entire software was developed around the fundamental idea that the tasks required should be performed by a suite of independent algorithms, each performing a full operation (or image processing task) on their own but especially fit for running simultaneously and uninterruptedly. Aurora tracking can be initiated by the user via a click on the software's icon shown in Figure 5.1.

Furthermore, each of these constitutive scripts is run using a universal parameters.py script, which allows the user to modify the program settings with ease. This allows the operation of any MISS device, as well as the processing of the data collected by it, given that parametric and calibration data are readily available. The current version of the software, 'MISS 2.0' is a personal design performing tasks similar to the ones performed by the current software developed by Mikko Syrjäsuo (KHO/UNIS) used to run MISS 1. It primarily handles the uninterrupted capture of spectrograms at darkness conditions along with the activation of the eventual mechanical front-lens shutter. Additionally, MISS 2.0 updates KHO's website with the latest averaged spectrogram on a minute-basis, along with a 24-hour keogram which is then also archived for ulterior needs.

The entirety of the software is written in Python, a convenient tool for automation and real-time data handling. It is currently able to handle operations for both MISS 1 and MISS 2, using respective parameters and the calibration data detailed in Chapter 6. All scripts used for the MISS 2.0 can be found in a personal GitHub repository (<https://github.com/NicolasLTU/KHO-MISS/tree/main>) and will be

made available on the repository of UNIS, <https://github.com/UNISvalbard>.

5.2 Configuration Parameters

This script gathers the main parameters susceptible to require modifications by the user of MISS 2.0. It is loaded by all script composing MISS 2.0 to ensure that the same parameters are used throughout the entire software.

Paths
Folder for spectrograms [raw data]
Folder for averaged spectrograms [temporary files]
Folder for processed spectrograms [temporary files]
Folder for RGB columns [temporary files]
Folder for keograms [archived files]
Folder for website data feed
Camera Settings
Exposure duration
Set temperature for the camera
Time between image captures
Horizontal binning
Vertical binning
Spectral Calibration Fit
Polynomial fit coefficients for MISS 1
Polynomial fit coefficients for MISS 2
Radiometric Calibration Factor
Polynomial fit coefficients for MISS 1
Polynomial fit coefficients for MISS 2
Horizon Limits
Pixel extent of the FOV of MISS 1
Pixel extent of the FOV of MISS 2

Table 3: Detail of the configuration parameters contained in parameters.py

5.3 Automated Aurora Tracking

5.3.1 MISS Controller (Main script)

- Overview

This script manages all system operations of MISS. It operates both the Atik 414EX camera and the SunShield shutter (if connected) based on real-time darkness conditions at KHO.

- Functionality

It checks whether it is dark enough every 60 seconds with the condition that the sun should be at an elevation below -10° and either opens the SunShield and starts image capture when conditions are met, or stops the processes when the darkness condition is no longer met. It also works as the ON/OFF switch button of the aurora tracking program for MISS, with a safe handling of any manual interruption using the `ctrl + c` command.

- User Access

A clickable icon using the image in Figure 5.1 is available on the computer controlling MISS.

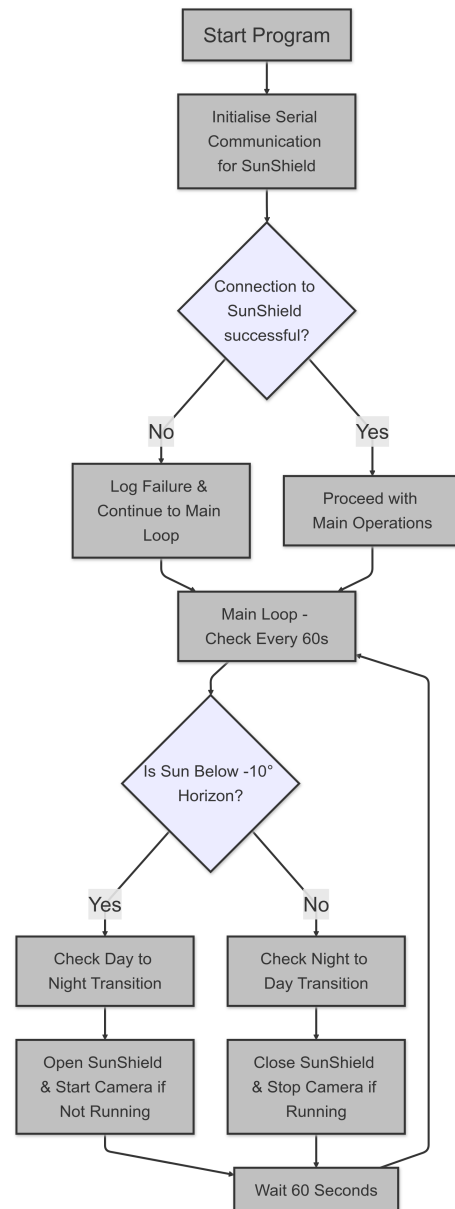


Figure 5.2: Workflow - MISS Controller

5.3.2 Atik Controller

- Overview

This script controls the Atik 414EX camera in the MISS spectrograph, capturing four 12-second exposure images per minute starting at exactly zero seconds passed each new minute ($12 \text{ sec} + t_{\text{readout}} + t_{\text{left}} = 15$ seconds between two consecutive capture starts).

- Functionality

Saves the data in 16-bit PNG grayscale along with relevant metadata (name of the device, exposure time, temperature measured by the camera, binning, etc.). The spectrograms are stored in a date-based folder structure using a UTC (Universal Time Coordinated) date-time filename of the type:

MISS[1 or 2]-yyyymmdd-hhmmss.png.

- Integration

The Atik 414EX is controlled via a C/C++ SDK (Software Development Kit), integrating it to the rest of the Python program therefore requires a Python wrapper, also made available by Atik Cameras on their website. The script uses some of the wrapped commands for capture operations and temperature control and lists all of them.

- Product

16-bit grayscale PNG spectrograms with relevant metadata.

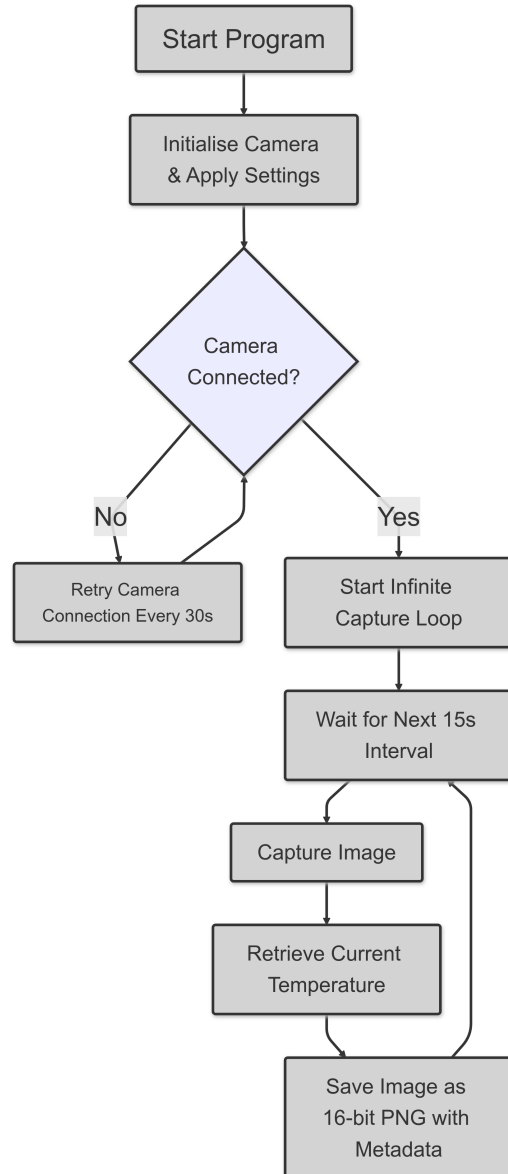


Figure 5.3: Workflow - Atik Controller

5.3.3 SunShield Controller

This script gathers the functions which are called by the main script (MISS Controller) to control the SunShield shutter via serial communication. It initialises a serial connection and allows for opening and closing the shutter. The script is also equipped to handle potential communication errors and provides real-time feedback on the shutter's status.

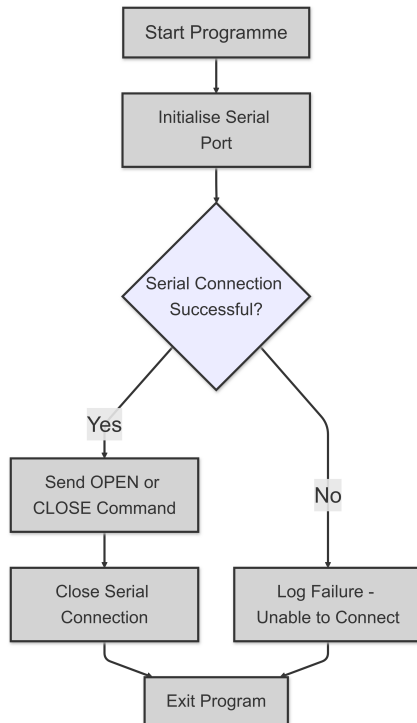


Figure 5.4: SunShield Control Test Workflow

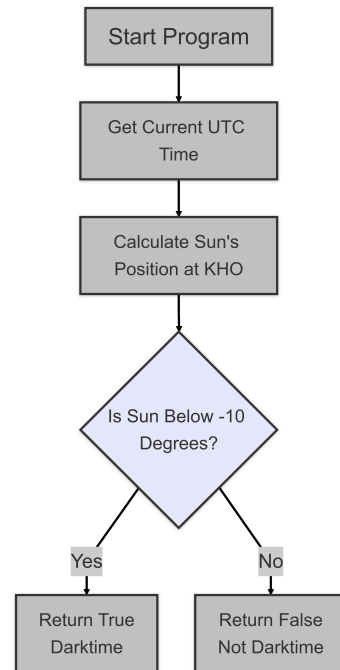


Figure 5.5: Workflow of Night Condition

5.3.4 Darkness Condition

- Overview

The script checks if the sun is under -10° of elevation below the horizon to determine whether it is dark enough for MISS operations.

-Functionality

The calculation is performed using UTC time and the geographical coordinates of KHO. If the sun is below -10° , the script returns True, indicating that MISS

shall remain/be turned ON. Otherwise, it returns None, indicating that *MISS* shall remain/be turned OFF.

*The geographical coordinates must be modified accordingly if the *MISS* is operated at a different location. Likewise, the condition on the angular elevation of the sun has to reflect the darkness level required by the user.*

5.4 Real-Time Data Processing

5.4.1 Summary of the Program Workflow

The figure below shows the main processes by which a processed spectrogram and a daily keogram are updated on *KHO*'s website. The outputs in blue are all temporary and shall therefore not be conserved past their use. The files in red are archived.

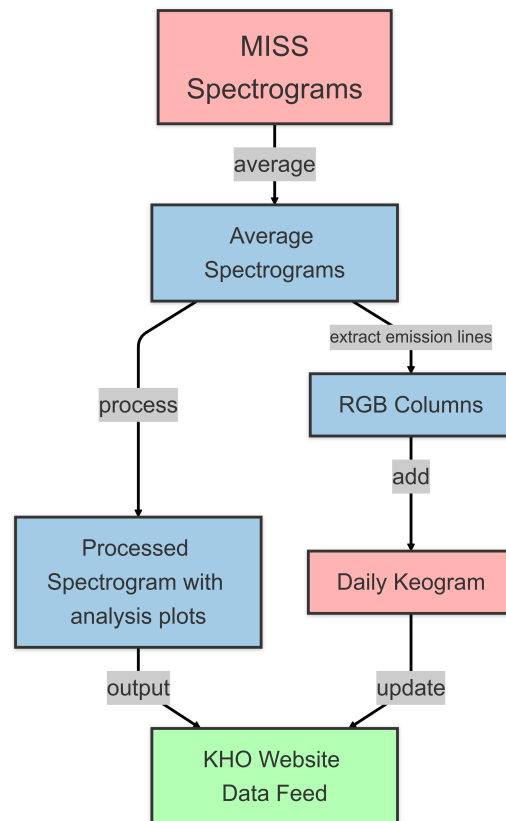


Figure 5.6: Summary of the Main Steps of Real-Time Data Processing

5.4.2 Real-Time Data Processor (Main Script)

- Overview

This script essentially works as an ON/OFF switch for the uninterrupted live-update of the latest data collected by [MISS](#).

- Functionality

Starts all programs contributing to the generation of analytical views of the most recent spectrometric data available under the form of a spectrogram with spectral and spatial analyses and a 24-hour keogram, updated on the instrument's data page on [KHO's website](https://kho.unis.no/Data.html) (<https://kho.unis.no/Data.html>).

- User Access

Launched via a clickable icon and made to be safely interrupted using the `ctrl + c` command. It can be used on any computer with real-time access to the directory where the spectrograms captured by [MISS](#) are saved, provided that it is correctly configured.

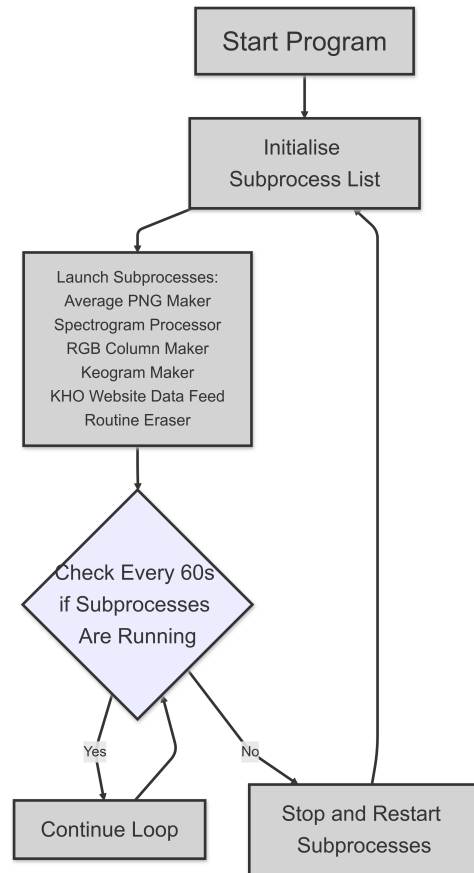


Figure 5.7: Workflow - real-time data processor

5.4.3 Average Spectrogram Maker

- Overview

All live updates (spectrograms and keograms) are based on data averaged over one-minute intervals. To facilitate this, it is therefore necessary to first average all spectrograms minute-wise, which serves as the base for all subsequent processes.

- Functionality

This script groups spectrogram by the full minute in which they were captured (each minute containing 4 spectrograms). It reads the instrument's name in the metadata to ensure that the right dataset is being used consistently by the entire program. It then averages them and stores the result in a dedicated date-specific directory. Relevant metadata, some of which is useful for key parts of the subsequent processes. A note about the averaging process is also added to prevent them from being mistaken for unprocessed spectrograms, in case of accidental relocation.

- Input files

Spectrograms captured by [MISS](#).

- Product

Temporary minute averaged spectrograms with relevant metadata.

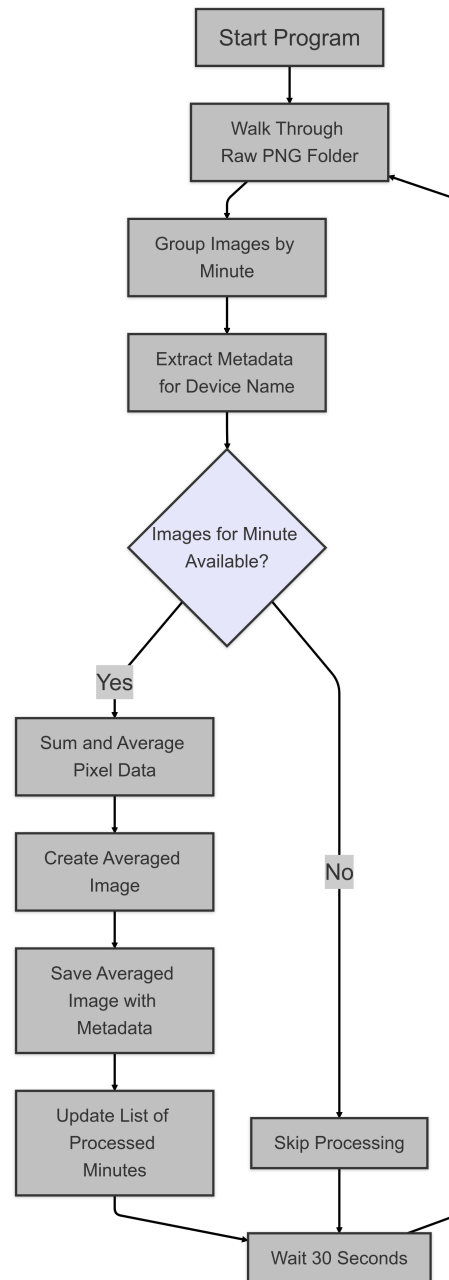


Figure 5.8: Workflow - average spectrogram maker

5.4.4 RGB Column Maker

- Overview

This script extracts the emission line data corresponding to the aurora's red (6300 Å), green (5577 Å), and blue (4278 Å) channels. It processes these data into RGB columns, which are used for visual representation in keograms.

- Functionality

Extracts the spectral data corresponding to the 3 key aurora emission lines (6300Å, 5577Å, 4278Å) from the 1-minute averaged spectrograms, calculating their respective position using the spectral calibration data presented in Chapter 6. *Note: the current version does not account for optical distortions (smile and keystone). Instead, it considers the emission lines aligned.*

Averages respective sections into one-line rows covering the entire FOV before transforming them into a 300 row-long 24-bit (3 x 8 bit) RGB column.

The RGB columns are generated and saved every minute using any new averaged spectrogram found in the allocated directory, using a filename of the type:

MISS[1 or 2]-yyyymmdd-hhmm00_RGB.png.

- Input files

Averaged spectrograms.

- Product

Temporary 24-bit RGB columns (300,1,3) representing the auroral events of a minute each.

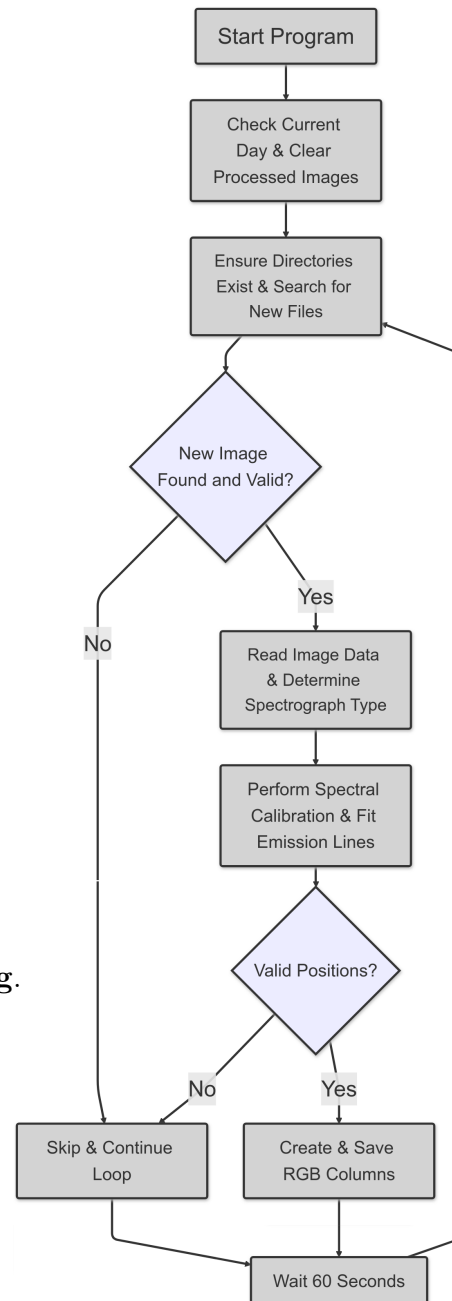


Figure 5.9: Workflow - RGB column maker

5.4.5 Keogram Maker

- Overview

This script continuously updates a daily keogram using RGB columns generated from the spectrograms captured by [MISS 1](#) or [MISS 2](#). It ensures that all auroral spectral data available for each minute of the day is processed and included in the keogram, which presents the auroral activity from the three main auroral emission lines.

- Functionality

Checks for new RGB columns every five minutes. Every new RGB column is added to the current day's keogram created daily and presenting the visual record of auroral activity throughout the day in UTC time. A special routine ensures a smooth transition between yesterday's and a new day's keogram. All keograms are placed in their respective date-based directory and are archived for later use under the filename type:

MISS[1 or 2]-keogram-yyyymmdd.png

- Input Files

Temporary 24-bit RGB columns (300,1,3) representing the activity of one minute each.

- Product

Daily Keogram providing a visual representation of the auroral activity over 24-hour.

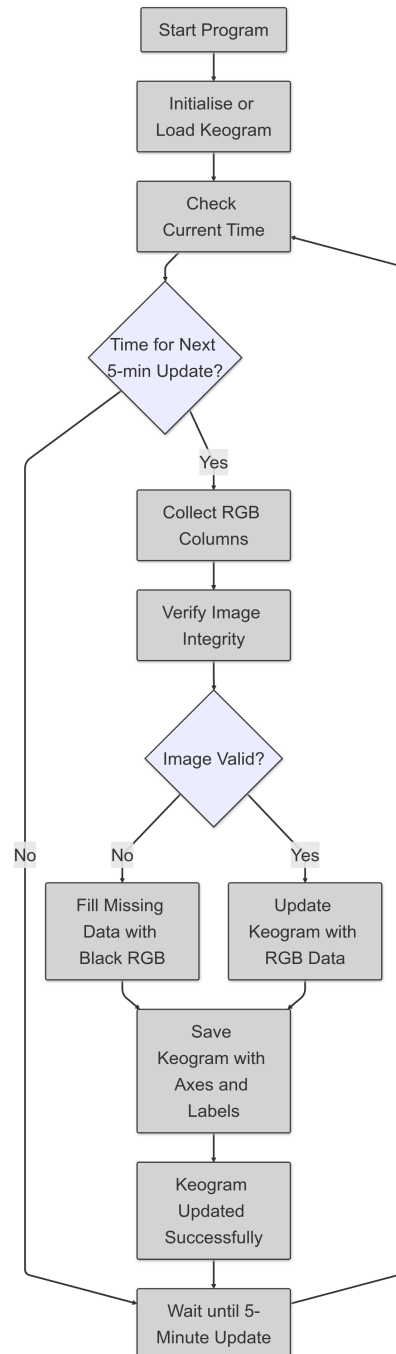


Figure 5.10: Workflow - keogram maker

5.4.6 Spectrogram Processor

- Overview

This script processes averaged spectrogram images generated by the *Average spectrogram maker* (5.4.3). It performs processing tasks in order to save the 1-minute averaged spectrogram along with spectral and spatial plot analyses.

- Functionality

Each new averaged spectrogram is first flipped and rotated to present its wavelength axis horizontally and its FOV vertically. A background subtraction is then made, to improve the SNR and the portion of the image beyond the pixel FOV of the instrument is removed. Instrument specific spectral and radiometric calibration data are then applied to present the data plotted in physical units, with the instrument's spectral range and with the radiance in Rayleigh. The processed spectrogram is then saved along the spectral plot (up) and the spatial plot (right side) as a temporary file with the following filename type:

MISS[1 or 2]-spectrogram-yyyymmdd-hhmm00.png

- Input files

Temporary averaged 16-bit grayscale spectrograms over all spectrograms generated within 1 minute.

- Product

Temporary image of processed spectrogram along with spatial and spectral analysis plots.

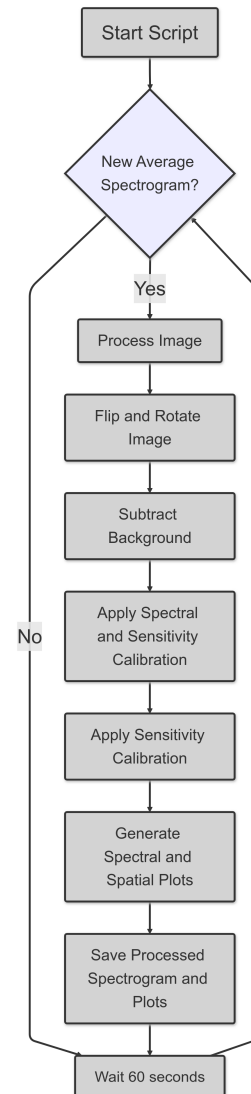


Figure 5.11:
Workflow -
spectrogram
processor

5.4.7 KHO Website Data Feed

- Overview

This script updates a web feed directory by copying the latest processed spectrogram and keogram images from their respective directories. These files represent the updates eventually seen on KHO's website. The script runs continuously, checking for new images and replacing older updates in the feed directory.

- Functionality

Checks every 30 seconds for new processed spectrograms and updated daily keogram. Then verifies their integrity to guarantee that the webpage will not show corrupted or incomplete files.

- Input Files and Product

Latest processed spectrogram and most recent update of the keogram of day (UTC time).

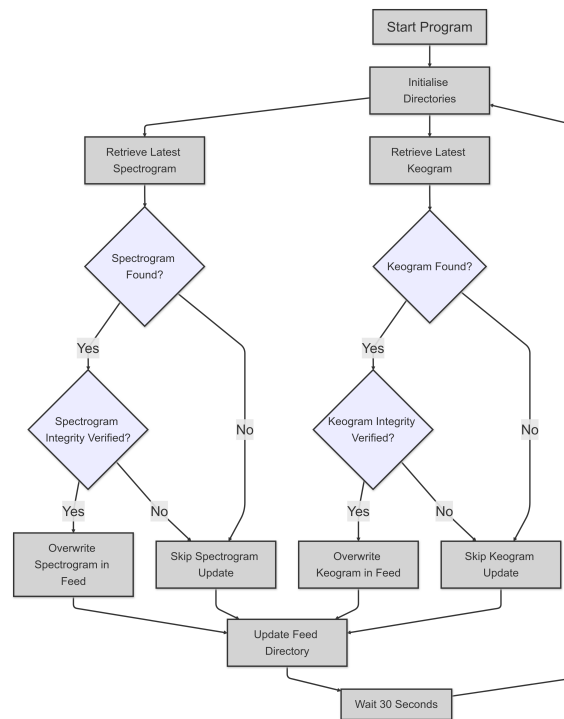


Figure 5.12: Workflow - KHO website data feed

5.4.8 Routine Eraser

- Overview

This script is designed to clean up all unnecessary temporary data resulting from the different processes of real-time data processing to prevent any storage issue. The directories where all temporary data are stored are structured by date (YYYY/MM/DD) and any data from past days is deleted if not needed for further processing.

- Functionality

The script goes through the date-directories of all temporary files from past days (temporary averaged spectrograms, processed spectrograms and RGB columns) and erase all directories for past days over since 10 minutes or more.

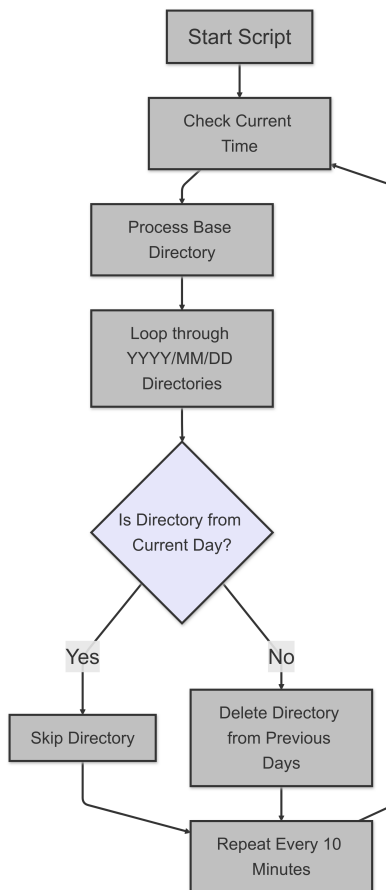


Figure 5.13: Workflow - Routine Eraser

5.5 Real-Time Website Data Output

The program described in 5.4 allows the uninterrupted generation of processed spectrograms and update of a keogram with the appearance of the following example figures, respectively based on a spectrogram of a the light from a regular office gas-discharge lamp captured by MISS 2 and on an image with fake colours. The processed spectrogram uses spectral and radiometric calibration data.

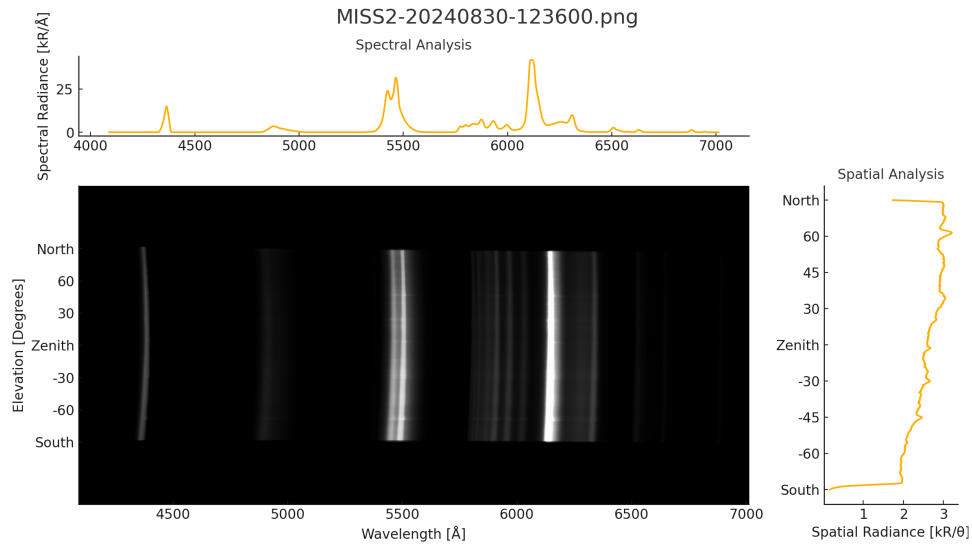


Figure 5.14: Example Processed Spectrogram of the light from a gas-discharge lamp

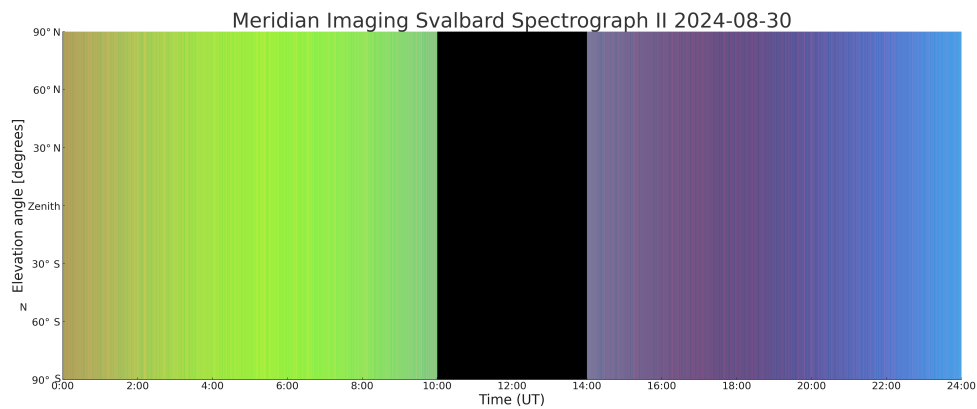


Figure 5.15: Example Daily Keogram with fake colours

5.6 Past Keogram Maker

Technical issues with the real-time data processing program may arise (electricity shortage, system failure...), preventing daily keograms to be generated for specific days. This extra program was specifically designed to allow the generation of any missing keogram. It gathers all the intermediary processes required for the generation of a keogram presented in the software detailed description, while integrating an extra feature: the possibility to generate a keogram with or without temporal and spatial analysis plots on respective sides.

It presents the advantage to synthesise the entire creation of a keogram in a comprehensive way, potentially allowing the user to gain a better understanding of the process used by MISS 2.0 to generate a keogram in real-time.

5.6.1 Simulated Keogram without Analysis Plots

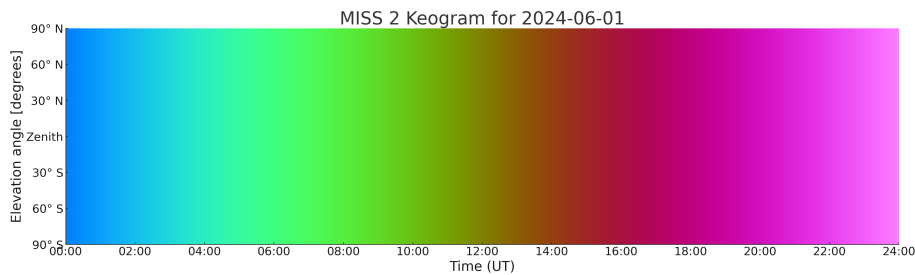


Figure 5.16: Keogram with fake colours (without analysis plots)

5.6.2 Simulated Keogram with Analysis Plots

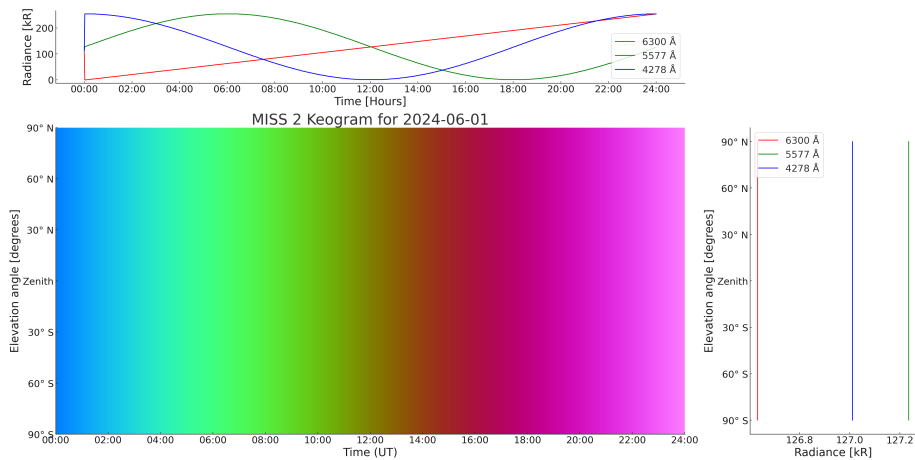


Figure 5.17: Keogram with fake colours (with analysis plots)

5.6.3 Diagram of the Workflow of Past Keogram Maker

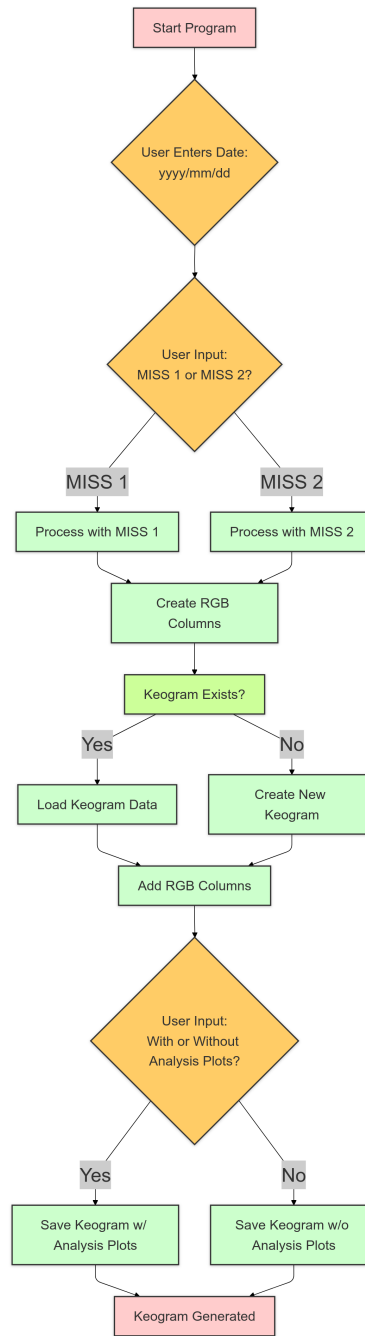


Figure 5.18

6 Calibration

6.1 Spectral Calibration

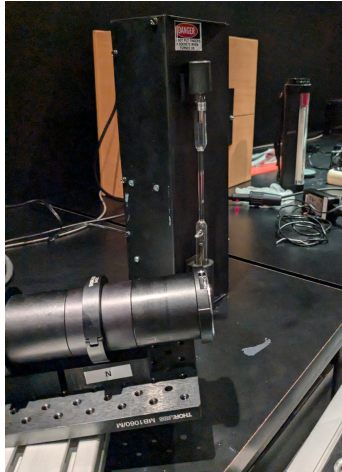


Figure 6.1: Spectral calibration using a hydrogen lamp

Spectral calibration is crucial for the interpretation and analysis of the spectrograms captured. It involves determining the precise correspondence between pixel positions on the detector and their associated wavelengths. Without proper calibration, the spectral information recorded in the spectrograms would be unreliable, and the non-linearity of the dispersion of light across wavelengths would prevent the identification of a specific emission line across the spectrogram.

I performed spectral calibration of [MISS 2](#) following Fred Sigernes' instructions at the optical laboratory of the department of Arctic Geophysics of [UNIS](#) in June 2024, with a *hydrogen lamp* as a light source (cf. [Figure 6.1](#)), using its main hydrogen-alpha emission line at $\lambda_1 = 6562 \text{ \AA}$. I then associated it with two characteristic mercury emission lines obtained via a spectrogram captured by [MISS 2](#) of light from a discharge gas lamp, $\lambda_2 = 5461 \text{ \AA}$ and $\lambda_3 = 4358 \text{ \AA}$ for polynomial fitting to map the non-linear dispersion of the spectrograph.

This process allows not only for the calibration, but also for the correction of any optical distortion (smile, keystone). This section will present a visual of how a specific emission line can be mapped, taking optical effects into account. However, implementing that solution to the software was not in the scope of this project, so

the MISS 2.0 software described in the previous Chapter approximates all emission lines as strictly linear.

6.1.1 Calibration Protocol

1. Turn on the hydrogen lamp, wait a few minutes until it is warmed up and reaches a constant output.
2. Place the front of the spectrograph faced directly towards the hydrogen lamp.
3. Carefully remove the front-lens to expose the entirety of the entrance slit to the light from the lamp. It should be placed a few centimetres from the lamp.
4. Ensure that no other light source is present in the room during the capture of calibration spectrograms.
5. Use a usb connection to control the Atik camera via the Artemis software from a separate monitoring room. Adjust the exposure time to avoid pixel saturation. A 1 x 1 binning is used.
6. Verify that a satisfactory spectrogram with clearly identifiable emission lines has been recorded before ending the manipulation and placing the front-lens back on the spectrograph to prevent dust from settling on the slit.

6.1.2 Results

The three emission lines used for the calibration can be identified by detecting all the peaks of intensity of the line through the entire FOV of MISS 2 on the hydrogen lamp emission calibration spectrogram (Figure 6.2) and the discharge gas lamp spectrogram (Figure 6.3). **Note: spectrograms are flipped by default by the Artemis software.**

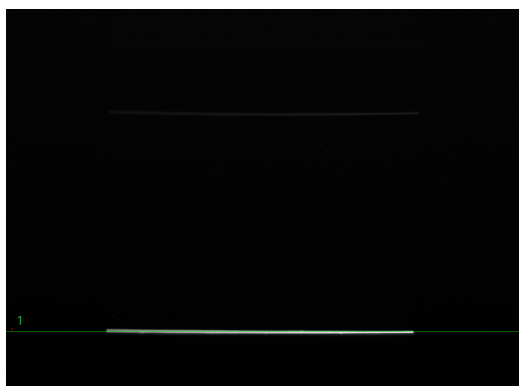


Figure 6.2: Hydrogen lamp emission calibration spectrogram
 $\lambda_1 = 6562 \text{ \AA} (H - \alpha)$

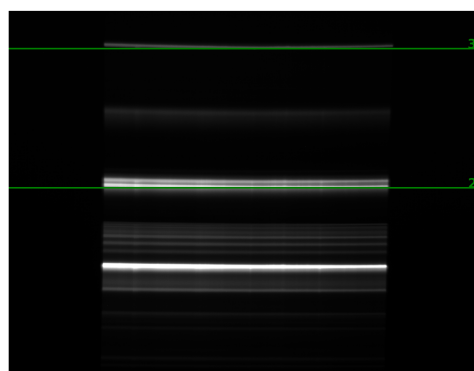


Figure 6.3: Discharge gas lamp 76 spectrogram
 $\lambda_2 = 5461 \text{ \AA}; \lambda_3 = 4358 \text{ \AA}$

The fainter H-beta emission can also be observed on Figure 6.2 at $\lambda = 4861\text{\AA}$. I deemed it too faint on this calibration spectrogram and decided not to use it as one of the calibration wavelength for MISS 2, but I used it successfully for the calibration of MISS 1.

6.1.3 Wavelength Mapping

For a wavelength mapping of the entire FOV of the spectrogram, polynomial fittings of all three emission lines are performed. We obtain an expression for the y-pixel position (spectral dimension) as a function of the x-pixel (spatial dimension) of the type $y(x) = A_0 + A_1x + A_2x^2$:

$$\begin{aligned} y_{4358}(x) &= 137.50 - 0.097863 \cdot x + 6.3437 \times 10^{-5} \cdot x^2 \\ y_{5461}(x) &= 516.08 - 0.043540 \cdot x + 3.0094 \times 10^{-5} \cdot x^2 \\ y_{6562}(x) &= 882.62 + 0.0060031 \cdot x - 4.2209 \times 10^{-6} \cdot x^2 \end{aligned}$$

This approach provides a close approximation of the position of these 3 emission lines. With these horizontal fits, we then perform a column-by-column vertical polynomial fitting, resulting in one polynomial equation per column within FOV. This process generates an approximation of the wavelength corresponding to every single pixel in range, which can be saved in a text-file. The entire wavelength mapping can be visualised in Figure 6.4, it helps deducing the positions of the three auroral emission lines (Figure 6.5).

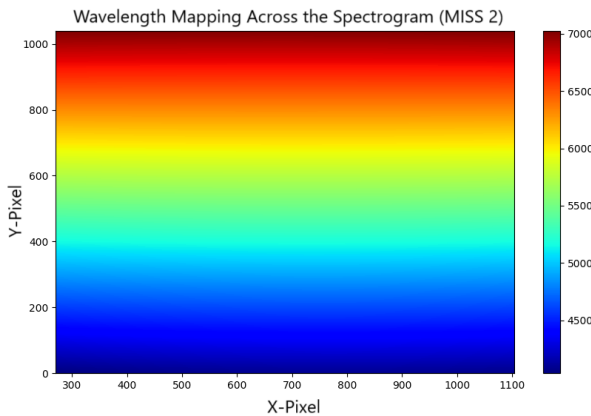


Figure 6.4: Wavelength map of the spectrograms of MISS 2

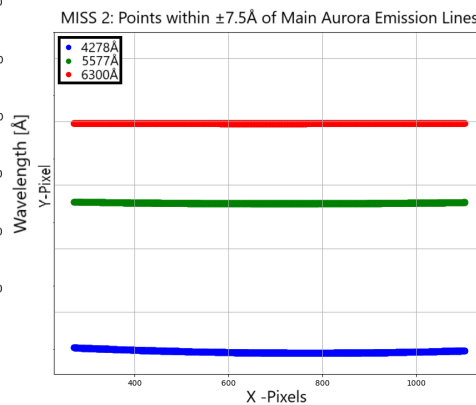


Figure 6.5: Estimated positions of 4278Å, 5577Å and 6300Å

6.1.4 Spectral Fitting Coefficients for MISS 2.0

For MISS 2.0, we approximate the emission lines appearing on the spectrograms as perfectly horizontal lines. We focus therefore on the vertical fitting made for the central columns and obtain a general spectral polynomial fit equation of the type $\lambda(y) = A_0 + A_1y + A_2y^2$:

$$\lambda(y) = 4088.5 + 2.6739 \cdot y + 1.3462 \times 10^{-4} \cdot y^2 \quad [\text{\AA}]$$

Or, when flipped to account for the natural orientation of a spectrogram recorded by MISS 2 using MISS 2.0 (with λ in \AA).

$$\lambda(y) = 4088.5 + 2.6739 \cdot (1039 - y) + 1.3462 \times 10^{-4} \cdot (1039 - y)^2 \quad (\text{MISS 2})$$

When using this approximation which does not account for the distortions caused by the smile and the keystone, it is important to make sure that the emission line sample collected is wide enough to get the entire portion at any elevation angle. It is therefore necessary to estimate the expected **FWHM** for a given wavelength.

6.1.5 Estimation of the FWHM

Using the hydrogen-alpha emission calibration spectrogram recorded in experimental settings, we approximate the **FWHM** for $\lambda_1 = 6562 \text{\AA}$ by plotting the average of the intensity (pixel value) along the 20 central columns (Figure 6.6). We can then observe the emission line profile of the emission line and calculate the **FWHM** directly from it.

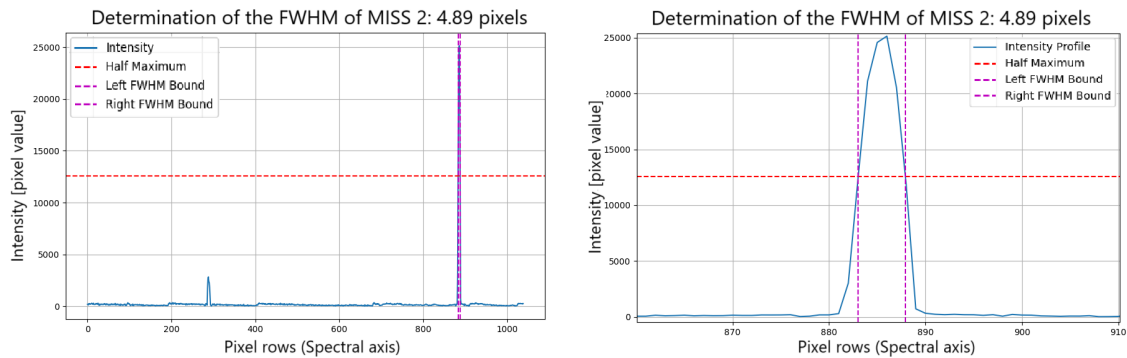


Figure 6.6: Left: Averaged intensity across central columns. Right: Zoomed-in hydrogen-alpha emission line profile for FWHM determination.

We first obtain a value in pixels (4.89 pixels), which we can approximate in Ångström using the spectral calibration data:

$$FWHM(\text{MISS 2}, \lambda = 6562 \text{ \AA}) \approx 14 \text{ \AA}$$

The expression for the ideal **FWHM** in 3.7 gives $FWHM_{ideal}(\lambda = 6562 \text{ \AA}) = 6.84 \text{ \AA}$. This real-life discrepancy is likely due to unaccounted factors such as imperfect alignment, uncertainty over the width of the entrance slit and imperfect focusing. It might also be exacerbated by overexposure, which could be explained by a non-linearity of the sensor response over brief exposure times, as was the case for this calibration method. Measurements made on auroral emission line might lead to closer estimations.

6.1.6 Spectral Calibration and Estimated **FWHM** for **MISS 1**

I calibrated **MISS 1** following the exact same procedure and the following spectral calibration equation (with λ in Å) and estimated **FWHM** were determined:

$$\lambda(y) = 4217.3 + 2.5652 \cdot (1039 - y) + 1.7000 \times 10^{-4} \cdot (1039 - y)^2 \quad (\text{MISS 1})$$

$$FWHM(\text{MISS 1}, \lambda = 6562 \text{ \AA}) \approx 13 \text{ \AA}$$

6.2 Radiometric Calibration

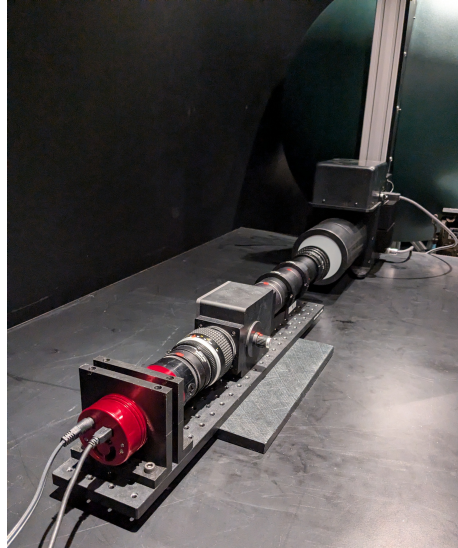


Figure 6.7: Sensitivity calibration.

With the results from spectral calibration, it is possible to proceed to spectral radiance calibration, which is an important step of the process accounting for the radiometric response of the spectrograph across the wavelength range of a spectrogram and throughout the entire FOV.

I performed the radiometric calibration of [MISS 2](#) following Fred Sigernes' instructions at the optical laboratory of the department of Arctic Geophysics of [UNIS](#) in July 2024, using a *Alcor-RC low brightness lamp* conceived by Keo Scientific and using the data from its certified spectral radiance calibration performed by the National Research Council of Canada ([National Research Council of Canada \(NRC\)](#)), which can be found in integral in *Appendix C*. The setup for this calibration is shown in [Figure 6.7](#).

6.2.1 Calibration Protocol

1. Turn on the low brightness lamp, wait a few minutes until the lamp reaches a stable spectral radiance. It is connected to a computer, which monitors and displays the spectral radiance curve of the lamp in real-time.

2. Position the front of the spectrograph faced directly towards the low brightness lamp, as close as possible to maximize the detection of low-intensity light.
3. With the front-lens on, only a portion of the spectrogram will receive light from the lamp. Start with the spectrogram at right angle to the flat surface of the lamp, capturing light directly corresponding to the zenith.
4. Ensure that no other light source is present in the room during the capture of calibration spectrograms.
5. Use a usb connection to control the Atik camera via the Artemis software from a separate monitoring room. Adjust the exposure time to match the exposure time of the instrument during operation (**t = 12 seconds**). A 1 x 1 binning is used.
6. Verify that a satisfactory spectrogram has been recorded. Then, repeat the process rotating the spectrograph at various angles relative to the surface of the lamp by increments allowing all portions of the spectrogram get illuminated on at least one spectrogram.
Suggested angle increments: $-90^\circ, -75^\circ, -60^\circ, -45^\circ, -30^\circ, 0^\circ, 30^\circ, 45^\circ, 60^\circ, 75^\circ, 90^\circ$.

6.2.2 Results

Using the captured calibration spectrograms from all required angles, a composite image covering the entire surface of a spectrogram. Background subtraction is applied to ensure that all pixel values reflect the actual radiance from the lamp:

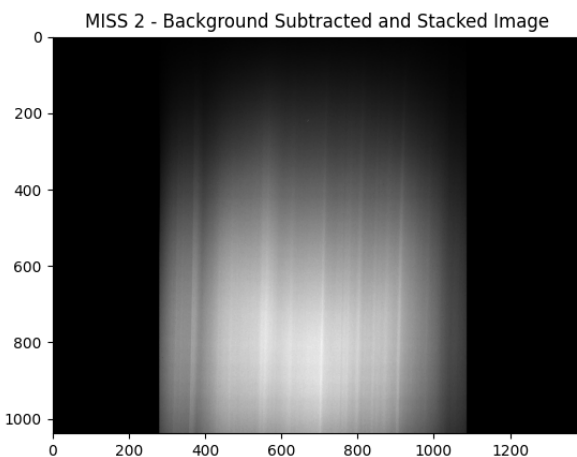


Figure 6.8: Composite spectrogram covering the entire FOV of MISS 2 (enhanced contrast)

Each pixel has a specific pixel value in 16-bit (i.e ranging from 0 to 65535) which we can attribute to a specific incident spectral radiance, knowing the spectral radiance curve provided by the calibration detailed in *Appendix C* and shown in [Figure 6.9](#).

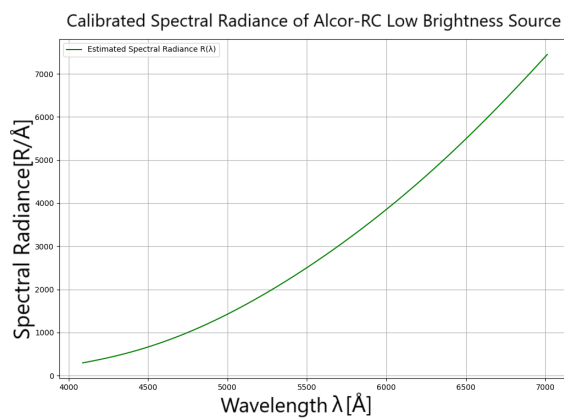


Figure 6.9: Alcor RC low-brightness calibrated spectral radiance curve

We can use this curve of the spectral radiance from the source, associated with the spectral calibration fitting from spectral calibration to convert each pixel value with the help of the calibration factor $K(\lambda)$ such that:

$$K(\lambda) = \frac{\text{pixel value}(\lambda)}{\text{calibrated radiance } L(\lambda)} \quad (6.1)$$

We average the pixel values of the 20 central columns and plot them as a function of λ . The resulting curve is shown below:

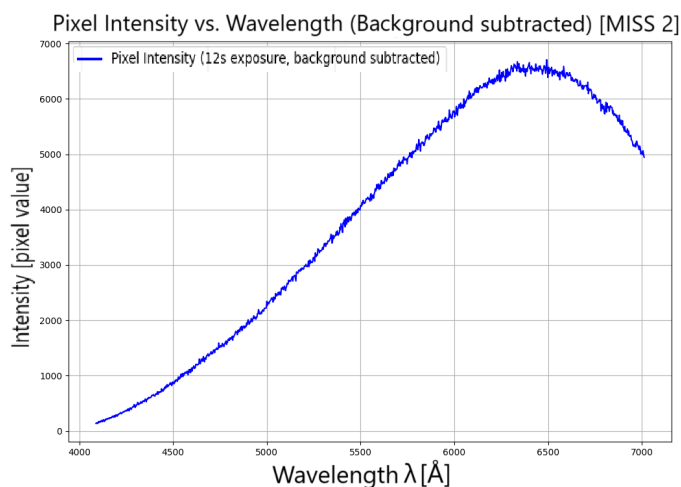


Figure 6.10: Pixel as a function of the wavelength

We can observe a significant decrease at wavelengths above 7000 Å despite the increasing spectral radiance, showing an expected reduced spectral response as the wavelength gets higher. Finally, we obtain $K(\lambda)$ using the calibration data represented in Figure 6.9 and the pixel values across the entire spectral range of MISS 2 in Figure 6.10. We get the following curve:

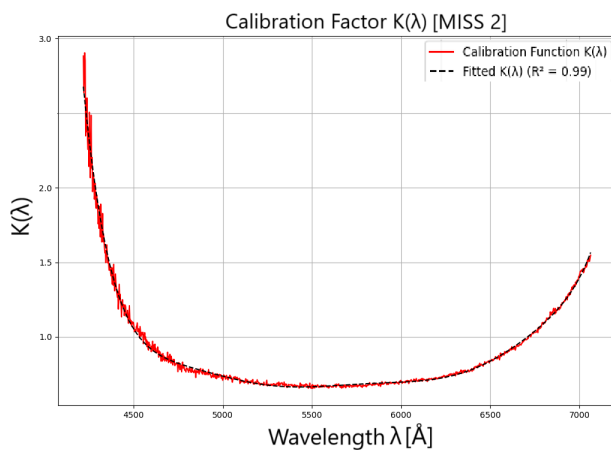


Figure 6.11: Calibration coefficient $K(\lambda)$ (MISS 2)

6.2.3 Radiance mapping

Due to the steep slope of $K(\lambda)$ at wavelengths below 4500 Å, achieving a high coefficient of determination ($R^2 \approx 0.99$) as seen on Figure 6.11 requires a 10th-degree polynomial fit, resulting in an overly complex expression for $K(\lambda)$. To balance accuracy and simplicity, we opt for a 5th-degree polynomial, providing a reasonable approximation. This expression using the fit of $K(\lambda)$ is then used to calibrate the spectral radiance of each pixel across the entire spectrogram. Here, we neglect the optical distortions and consider that each given row represent the same wavelength across the entire spectrogram:

$$L(\lambda) = \text{Pixel value}(\lambda) \times K(\lambda) \quad (6.2)$$

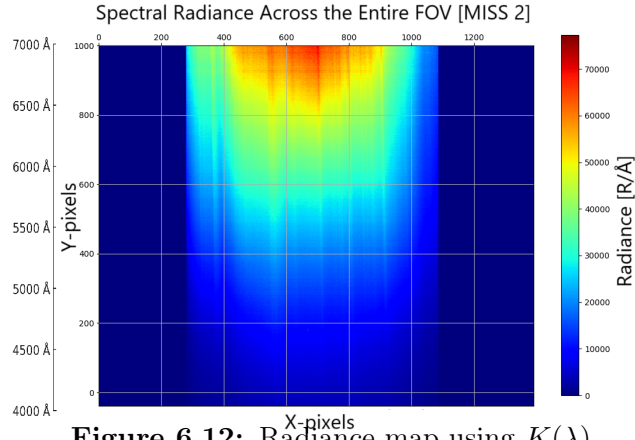


Figure 6.12: Radiance map using $K(\lambda)$

6.2.4 Calibration Coefficient K Fitting Coefficients

The expression of $K(\lambda)$ below was estimated. K is in $\frac{R}{\text{Å} \cdot \text{counts}}$ and λ is in Å.

$$\boxed{K(\lambda) = -1.2875 \times 10^{-16} \lambda^5 + 3.9290 \times 10^{-12} \lambda^4 - 4.7259 \times 10^{-8} \lambda^3 + 2.6455 \times 10^{-4} \lambda^2 - 7.8096 \lambda + 922.15} \quad (\text{MISS 2, } R^2 = 0.97) \quad (6.3)$$

6.2.5 Linearity Test

Using the same Alcor-RC low brightness lamp, we verify that the spectrograph maintains a consistent, linear response over different exposure times by determining the expression of the pixel values across all wavelengths as a function of the exposure time. In order to do that, we need to follow the calibration protocol in 6.2.1 with a few amendments:

- 2'. The spectrogram remains positioned at a right angle to the surface of the lamp during the entire process.

- 3'. The capture and record processes are made with the front-lens removed to allow the entire slit to receive light in one capture.
- 5'. Spectrograms are recorded using different exposure times: 1 s, 2 s, 4 s, 6 s, 8 s, 10 s, and 12 s.

Using a 50 central column averaging on all spectrograms with respective exposure times, we get the values plotted in Figure 6.13.

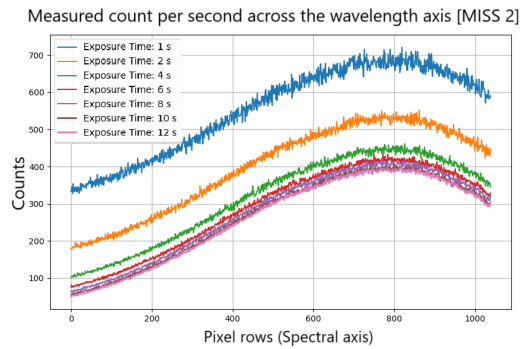


Figure 6.13: Averaged intensity across central columns

Based on these values, we can now make a polynomial fitting of the pixel values as a function of the exposure time for each pixel of the averaged column, which gets us the determined linear fitting equations of the form $Ax + B$ where each A and B is determined and represented in Figure 6.14. The proportional variation of the pixel value over exposure time is verified with $R^2 = 1$.

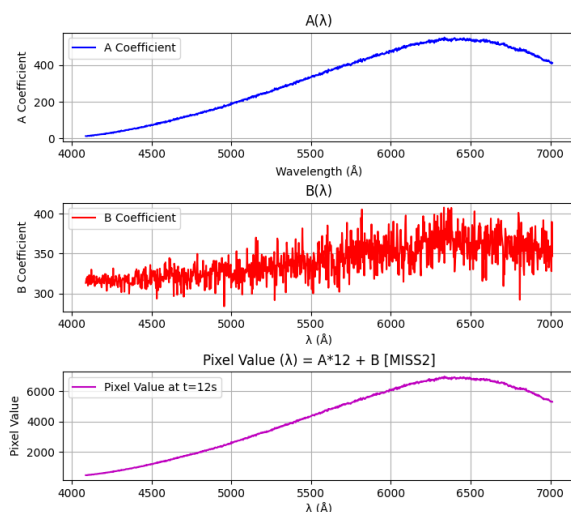


Figure 6.14: Fitted A and B coefficients for each averaged pixels for MISS 2

6.2.6 Radiometric calibration and Linearity Test for MISS 1

I calibrated MISS 1 following the exact same procedure and the following calibration factor $K(\lambda)$ for MISS 1 was determined (Figure 6.15) and the proportionality of the variation of its pixel values over exposure time was also verified (Figure 6.16).

$$\begin{aligned}
 K(\lambda) = & -1.3786 \times 10^{-16} \lambda^5 + 4.0883 \times 10^{-12} \lambda^4 \\
 & - 4.8063 \times 10^{-8} \lambda^3 + 2.8024 \times 10^{-4} \lambda^2 \\
 & - 8.1099 \lambda + 932.96
 \end{aligned}
 \quad (\text{MISS 1, } R^2 = 0.995) \quad (6.4)$$

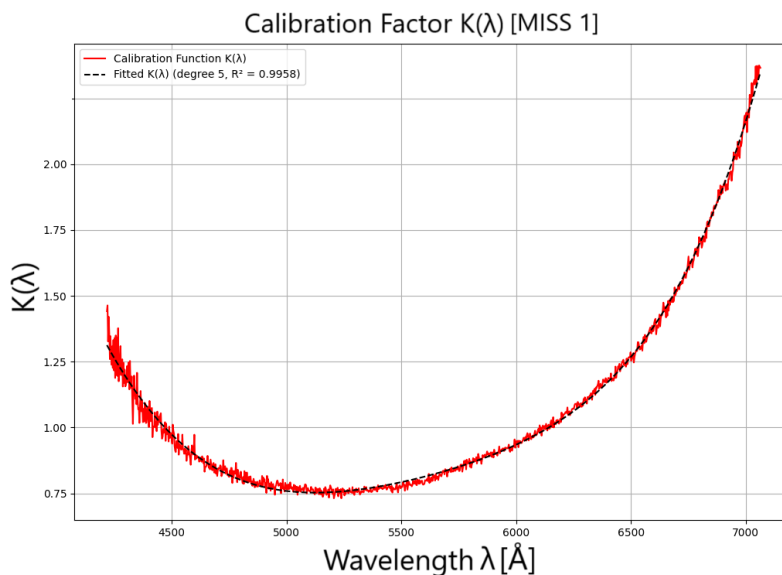


Figure 6.15: Calibration coefficient $K(\lambda)$ (MISS 1)

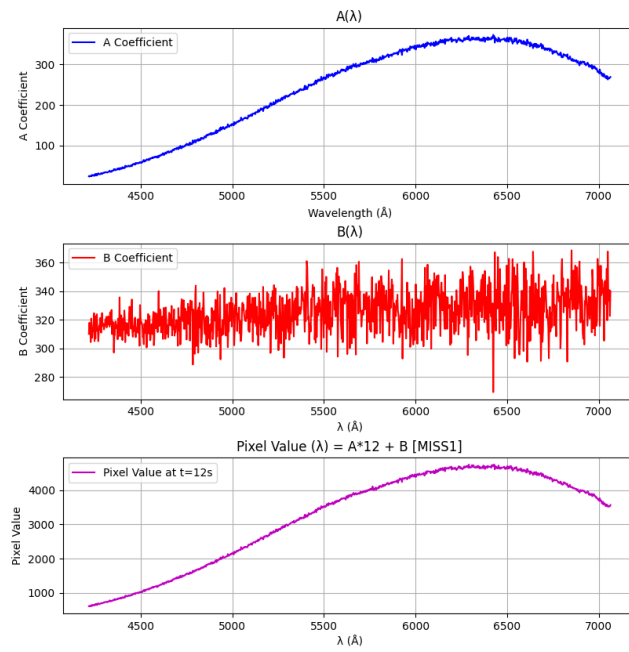


Figure 6.16: Fitted A and B coefficients for MISS 1.

7 Results

At the time of writing, MISS 2 has not been tested for aurora tracking yet. However, it will enter testing phase at KHO during winter 2024/25. This will be a chance to verify that both hardware and software provide a satisfying output. It is, however, possible to comment on the data gathered by MISS 1, which has been operational for several years, along with MSP.

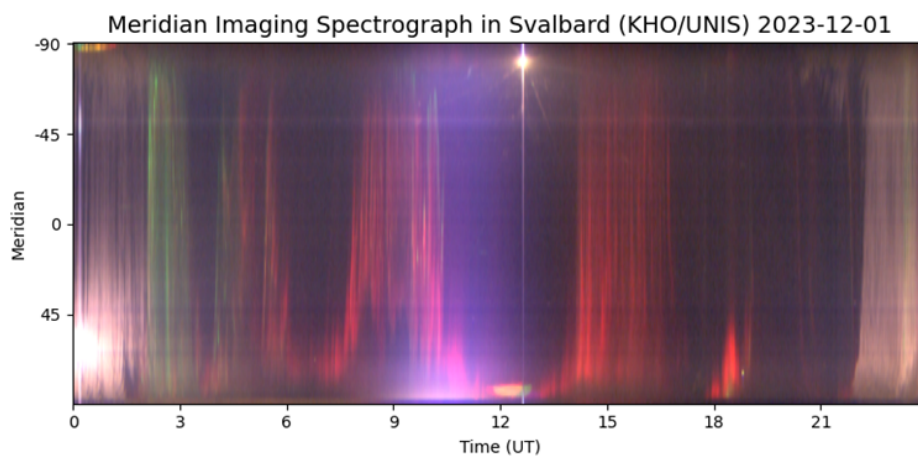


Figure 7.1: MISS 1 keogram for 2023-12-01 (KHO)

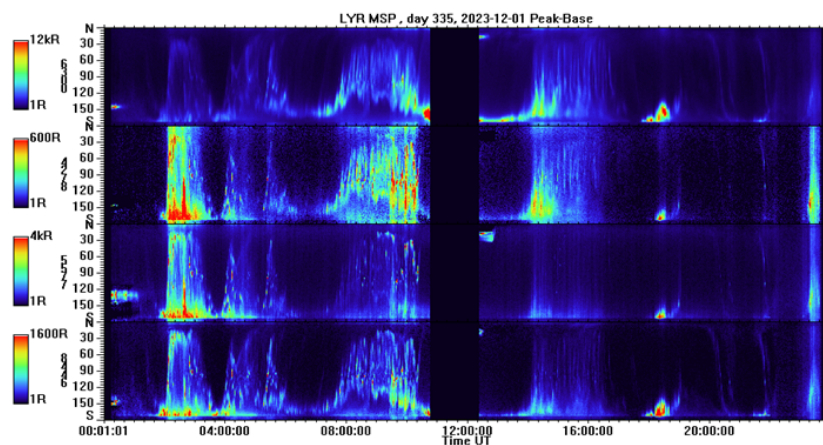


Figure 7.2: MSP keogram for 2023-12-01 (KHO)

The data gathered by [MISS 1](#), as shown in the keogram for December 1, 2023 ([Figure 7.1](#)), demonstrates the imager's capability in aurora tracking with improved spectral and spatial resolution. It also shows that its sensor sustains a wide intensity range, performing well on both low-intensity light and during the most luminous part of the day around noon. This observation is significant because monitoring faint dayside auroras is one of the imager's most crucial tasks at [KHO](#). The ideally high geographical latitude of Svalbard allows their observation and their study is therefore of high importance.

In contrast, the [MSP](#) keogram for the same day, based on data from its four channels (see [Figure 7.2](#)), shows limitations in handling the full range of intensities. While the blue dayside aurora was correctly captured by [MISS 1](#), it appears too subtle for [MSP](#)'s detectors. Monitoring the subtle features of faint dayside auroras might therefore be performed more appropriately using [MISS 1](#), which also presents the great advantage of capturing spectrograms of the entire visible range, effectively increasing the amount of valuable data greatly. This point is also important, considering the visible range contains numerous auroral emission lines, including potentially rare and unknown ones, which the imager might detect.

8 Conclusion

This project had one primary goal: to ensure that the design of the first **MISS** spectrograph could be successfully adapted into a fully functional new instrument, with both its hardware and software described in detail to guarantee its reproducibility, potential improvements, and future use.

Through my work at **UNIS**, I was given the opportunity to gain valuable knowledge about the functioning of the **MISS** spectrograph, which allowed me to contribute to the development of an improved version. The assembly, fine-tuning and calibration processes were successfully completed, allowing the instrument to function as intended, enabling nabling both qualitative and quantitative studies of auroral activity. The software development focused on providing real-time data, which is of particularly important for ongoing research projects at **UNIS** and for future studies.

Several challenges were encountered during the project, notably, a logistical delay in receiving the custom-made TGRISM house, which delayed the assembly of the instrument. Additionally, developing and improving the software without being able to test it on auroras was challenging at times, though tips and feedbacks from the persons involved in the project proved very helpful.

Replacing a spectrophotometer operating solely on four select auroral emission lines with data from the entire visible range, coupled with improved sensitivity and spectral resolution might give the ability to track rarer, more subtle features, which could allow advancing our understanding of auroral phenomena.

Overall, it can be estimated that putting **MISS**-type instruments into operation in Svalbard to effectively accomplish the task of tracking auroral activity might benefit research projects at large. With that in mind, I was offered by my project supervisor Fred Sigernes to introduce the new **MISS** imager to the international atmospherical studies community during the *21st EISCAT Symposium 2024 and 48th Annual European Meeting on Atmospheric Studies by Optical Methods* of Tromsø, as a novel optical instrumentation method for the study of aurora. An opportunity to familiarise concerned parties with an instrument to track auroras which could be beneficial to their own research.

I now look forward to the upcoming testing phase of 2024/25, which will allow to verify the operational capacities of **MISS 2**. My participation in the development of **MISS 2** has been a significant personal achievement, and I am optimistic it will benefit auroral research and atmospheric monitoring in the years to come.

References

- [1] Anders Jonas Ångström. “Recherches sur le spectre solaire”. In: *Kungliga Svenska Vetenskaps-Akademiens Handlingar* (1868). Section: Spectre de l’aurore boréale, pp. 41–42. URL: <https://archive.org/details/recherchessurle00nggoog>.
- [2] Helge Kragh. “The green line: a chapter in the history of auroral physics”. In: *Astronomy Geophysics* 50.5 (2009), pp. 5.25–5.28. DOI: <https://doi.org/10.1111/j.1468-4004.2009.50525.x>.
- [3] J. W. Chamberlain. “Oxygen Red Lines in the Airglow. I. Twilight and Night Excitation Processes”. In: *Astrophysical Journal* 127 (1958), pp. 54–66. DOI: [10.1086/146434](https://doi.org/10.1086/146434).
- [4] A. Vallance Jones and R. L. Gattinger. “The $O_2(b_g^{16} - X_g^{36})$ system in aurora”. In: *Journal of Geophysical Research* 79 (1974), pp. 4821–4822.
- [5] D. C. Cartwright, S. Trajmar, and W. Williams. “The excitation of O_2 in auroras”. In: *Annales Geophysicae* 28 (1972), pp. 397–401. URL: <http://www.ann-geophys.net/28/397/1972/>.
- [6] A. S. Kirillov. “Electronically excited molecular nitrogen and molecular oxygen in the high-latitude upper atmosphere”. In: *Polar Geophysical Institute of the Kola Science Centre RAS* (2024).
- [7] NASA Jet Propulsion Laboratory. *Airborne Visible/Infrared Imaging Spectrometer*. 2023. URL: <https://www.jpl.nasa.gov/missions/airborne-visible-infrared-imaging-spectrometer-aviris>.
- [8] Priyabrata Karmakar et al. “Crop monitoring by multimodal remote sensing: A review”. In: *Computers and Electronics in Agriculture* 178 (2020), p. 105762. URL: <https://www.sciencedirect.com/science/article/pii/S0168169920301367>.
- [9] Patrick Schratz et al. “Monitoring Forest Health Using Hyperspectral Imagery: Does Feature Selection Improve the Performance of Machine-Learning Techniques?” In: *Remote Sensing* 13.23 (2021). DOI: [10.3390/rs13234832](https://doi.org/10.3390/rs13234832). URL: <https://doi.org/10.3390/rs13234832>.
- [10] Marcel König, Gerit Birnbaum, and Natascha Oppelt. “Mapping the Bathymetry of Melt Ponds on Arctic Sea Ice Using Hyperspectral Imagery”. In: *Remote Sensing* 12.16 (2020), p. 2623. DOI: [10.3390/rs12162623](https://doi.org/10.3390/rs12162623). URL: <https://doi.org/10.3390/rs12162623>.

-
- [11] Paul Linton et al. “The application of hyperspectral core imaging for oil and gas”. In: *Geological Society, London, Special Publications* 527 (2022), pp. 95–119. DOI: 10.1144/SP527-2022-2. URL: <https://doi.org/10.1144/SP527-2022-2>.
- [12] Cyril Juliani and Steinar L. Ellefmo. “Prospectivity Mapping of Mineral Deposits in Northern Norway Using Radial Basis Function Neural Networks”. In: *Minerals* 9.2 (2019). Published: 24 February 2019, p. 131. DOI: 10.3390/min9020131. URL: <https://doi.org/10.3390/min9020131>.
- [13] Ines Dumke, Stein M. Nornes, and Autun et al. Purser. “First hyperspectral imaging survey of the deep seafloor: High-resolution mapping of manganese nodules”. In: *Scientific Reports* 8 (2018). DOI: 10.1038/s41598-018-28755-0. URL: <https://doi.org/10.1038/s41598-018-28755-0>.
- [14] Daniel McCraine et al. “Automated Hyperspectral Feature Selection and Classification of Wildlife Using Uncrewed Aerial Vehicles”. In: *Remote Sensing* 16.2 (2024). Corresponding author: Daniel McCraine, Geosystems Research Institute, Mississippi State University, Starkville, MS 39759, USA, p. 406. DOI: 10.3390/rs16020406. URL: <https://doi.org/10.3390/rs16020406>.
- [15] Silje Grue. “Machine Learning for Classifying Marine Vegetation from Hyperspectral Drone Data in the Norwegian Coast”. Applied mathematics and physics. Master’s thesis. UiT Norges arktiske universitet, 2022, p. 114.
- [16] Tiit Kutser, Ian Miller, and David L. B. Jupp. “Mapping coral reef benthic substrates using hyperspectral space-borne images and spectral libraries”. In: *Estuarine, Coastal and Shelf Science* 70.3 (2006), pp. 449–460. DOI: 10.1016/j.ecss.2006.06.026. URL: <https://doi.org/10.1016/j.ecss.2006.06.026>.
- [17] Chelsey Sturtevant. “AI-HyperCal: In-Scene Hyperspectral Imagery Calibration Using Artificial Intelligence Known-Point Identification”. In: *Air University Press* (2022). Capt. Chelsey Sturtevant, U.S. Air Force. URL: <https://www.airuniversity.af.edu>.
- [18] Kamaruzaman Jusoff and Kasawani Ibrahim. “Hyperspectral Remote Sensing for Tropical Rain Forest”. In: *American Journal of Applied Sciences* 6.12 (2009). Published on 31 December 2009, pp. 2001–2005. DOI: 10.3844/ajassp.2009.2001.2005. URL: <https://doi.org/10.3844/ajassp.2009.2001.2005>.
- [19] Martin H. Skjelvareid et al. “Mapping Marine Macroalgae along the Norwegian Coast Using Hyperspectral UAV Imaging and Convolutional Nets for Semantic Segmentation”. In: *Proceedings of the IEEE International Geoscience and Remote Sensing Symposium (IGARSS)*. IEEE. 2023.

-
- [20] University Centre in Svalbard. *Meridian Imaging Svalbard Spectrograph (MISS)*. <https://kho.unis.no/Instruments/MISS.html>. Accessed: September 30, 2024.
- [21] University Centre in Svalbard. *Multi-Spectral Imager (MSP)*. <https://kho.unis.no/Instruments/MSP.html>. Accessed: September 30, 2024.
- [22] Fred Sigernes. *Head of KHO*. Personal communication. "31 optical and 16 radio instruments" - Kjell Henriksen Observatory, as of October 2024.
- [23] F. Sigernes. *BASIC HYPER SPECTRAL IMAGING*. Hyperspectral remote sensing - detailed lecture notes. Accessed: 30 September 2024. URL: https://aurora.unis.no/doc/TTK20/BASIC_HYPER_SPECTRAL_IMAGING.pdf.
- [24] Bahaa E. A. Saleh and Malvin Carl Teich. *Fundamentals of Photonics*. Discusses principles of light propagation, including Fermat's principle. John Wiley & Sons, 2007. Chap. 1.
- [25] Thomas Young. "The Bakerian Lecture: On the Theory of Light and Colours". In: *Philosophical Transactions of the Royal Society of London* 94 (1804), pp. 1–16. DOI: [10.1098/rstl.1804.0001](https://doi.org/10.1098/rstl.1804.0001).
- [26] Christiaan Huygens. *Traité de la lumière*. A foundational work for the wave theory of light. 1690.
- [27] Yen-Jie Lee. *Chapter 13: Interference and Diffraction*. MIT OpenCourseWare, 8.03SC Physics III: Vibrations and Waves. Accessed: 4 October 2024. 2016. URL: https://ocw.mit.edu/courses/8-03sc-physics-iii-vibrations-and-waves-fall-2016/79c0663b6fc5d0a84a9f453e292ae121_MIT8_03SCF16_Text_Ch13.pdf.
- [28] Newport Corporation. *Determination of Blaze Wavelength*. Accessed: 30 September 2024. URL: <https://www.newport.com/n/determination-blaze-wavelength>.
- [29] Thorlabs, Inc. *Grating Efficiency Curves*. Accessed: 30 September 2024. URL: https://www.thorlabs.com/newgrouppage9.cfm?objectgroup_id=1123.
- [30] Yoshiyuki Shimizu. "Fisheye Lens System". US3734600A1. Granted: 22 April, 1973; Status: Expired. Dec. 1971.
- [31] Dr. Christophe Cavadore. *AllSkyMon Optical Layout*. <http://www.astrosurf.com/cavadore/technical/allSky/AllSkyMon/>. Made by Dr. Christophe Cavadore, PhD in Physics and Optics, specialised in astronomical instrumentation. Accessed: [11 October 2024].

-
- [32] Michael Geyer. *Project Memorandum*. Prepared for: Wake Turbulence Research Office. Refer to Section 3.5.1 for details on Satellite Altitude and Geocentric Angle Known. Accessed: 4 October 2024. URL: <https://ntlrepository.blob.core.windows.net/lib/59000/59300/59358/DOT-VNTSC-FAA-16-12.pdf>.
- [33] *Peleng All-sky lens 8 mm (Belomo)*. <https://lens-db.com/belomo-peleng-a-8mm-f35-fisheye-mc/>. Transmittance $T_1 = 0.7$, Accessed: September 30, 2024.
- [34] Edmund Optics Inc. *Field Lens, 50 mm Diameter, Uncoated*. <https://www.edmundoptics.com/p/50mm-dia-x-50mm-fl-mgfsb2sub-coated-double-convex-lens/2746/>. Transmittance $T_F = 0.9825$ for $\lambda \approx 5500 \text{ \AA}$, Accessed: September 30, 2024.
- [35] Thorlabs Inc. *200 mm FL Achromatic Collimating Lens (AC508-200-A-ML)*. Thorlabs Technical Specifications. Transmittance $T_2 = 0.995$, Accessed: September 30, 2024. URL: https://www.thorlabs.com/newgrouppage9.cfm?objectgroup_id=2696.
- [36] Schott AG. *N-BK7 Optical Glass Data Sheet*. <https://www.schott.com/shop/advanced-optics/en/Optical-Glass/N-BK7>. Transmittance $T_{BK7} \approx 0.996$ for $\lambda \approx 5500 \text{ \AA}$, Accessed: September 30, 2024.
- [37] Thorlabs Inc. *600 lines/mm Transmission Grating, Blazed at 28.7° (GT50-06V)*. https://www.thorlabs.com/newgrouppage9.cfm?objectgroup_id=1123&pn=GT50-06V. Transmittance $T_G = 0.56$ for $\lambda \approx 5500 \text{ \AA}$, Accessed: September 30, 2024.
- [38] Nikon Inc. *AF-S Nikkor 50mm Lens*. https://www.dxomark.com/Lenses/Nikkor/Nikon-AF-S-Nikkor-35mm-f14G-mounted-on-Nikon-D5600---Measurements__1139. Transmittance $T_3 = 0.605$ for $\lambda \approx 5500 \text{ \AA}$, Accessed: September 30, 2024.
- [39] Edmund Optics Inc. *1 λ UV Fused Silica Windows*. <https://www.edmundoptics.eu/f/1lambda-uv-fused-silica-windows/12485/>. Transmittance $T_{w1} = T_{w2} = 0.995$ for $\lambda \approx 5500 \text{ \AA}$, Accessed: September 30, 2024.
- [40] Keo Scientific. *SunShield*. Accessed: 2024-09-30. 2024. URL: <https://keoscientific.com/products/sunshield/>.

Appendix A, Component List for MISS 2 Spectrograph

#	ITEM	No.	DESCRIPTION	COMPANY
1	Grating holder	1	Transmission grating tunable holder	Electronic workshop (eMachineShop.com)
2	Grating frame	1	Locks grating	Electronic workshop (eMachineShop.com)
3	Slit house	1	Variable slits	Electronic workshop (eMachineShop.com)
4	Slit blade	2	Sharp steel blades	Electronic workshop (eMachineShop.com)
5	Tgrism house	1	Prism and grating box	Electronic workshop (eMachineShop.com)
6	Grism lid	1	Grism house top lid	Electronic workshop (eMachineShop.com)
7	Slit height	1	Slit height aperture	Electronic workshop (eMachineShop.com)
8	Camera mount	1	Camera mount	Electronic workshop (eMachineShop.com)
9	XT66SM2	2	SM2 Adapter plate	Thorlabs
10	SM2NFMA	2	Nikon F-mount adapter	Thorlabs
11	SM2M05	1	Lens tube 0.5" (12.7 mm)	Thorlabs
12	SM2L10	1	Lens tube 1.00" (25.4 mm)	Thorlabs
13	SM2L20	2	Lens tube 2.00" (50.8 mm)	Thorlabs
14	SM2L30	1	Lens tube 3.00" (76.2 mm)	Thorlabs
15	SM2TC	2	Clamp for SM2 lens tubes	Thorlabs
16	SM2RR	4	Internal retaining threaded ring	Thorlabs
17	SM2V10	1	Adjustable lens tube	Thorlabs
18	TM4	1	External T-mount to internal SM2	Thorlabs
19	SM2T2	2	SM2 Coupler external threads	Thorlabs
20	AC508-200-A-ML	1	Mounted Coated Achromatic $f = 200$ mm	Thorlabs
21	GT50-06V	1	Transmitting grating, 600 lines/mm @ 28.7°	Thorlabs
22	MB1060/M	1	Breadboard (100 mm x 600 mm x 12.7 mm)	Thorlabs
23	Littrow prism	1	BK7 (50 mm x 28.87 mm x 50 mm)	Altechna Co. Ltd
24	19-843	2	UV Fused Silica Window	Edmund Optics
25	32-979	1	Field lens $f = 50$ mm	Edmund Optics
26	Camera lens	1	Nikkor $f = 35$ mm $f/1.4$ objective	Nikon
27	Fish-Eye lens	1	Belomo Peleng $f = 8$ mm $f/3.5$ for Nikon	Belomo
28	SunShield 1	1	Front lens protection shutter [not mounted]	Keo Scientific
29	CCD sensor	1	Atik 414EX	Atik Cameras

Table 4: Full Component List for MISS 2 (September 2024)

Appendix B, Views of MISS 2 Spectrograph

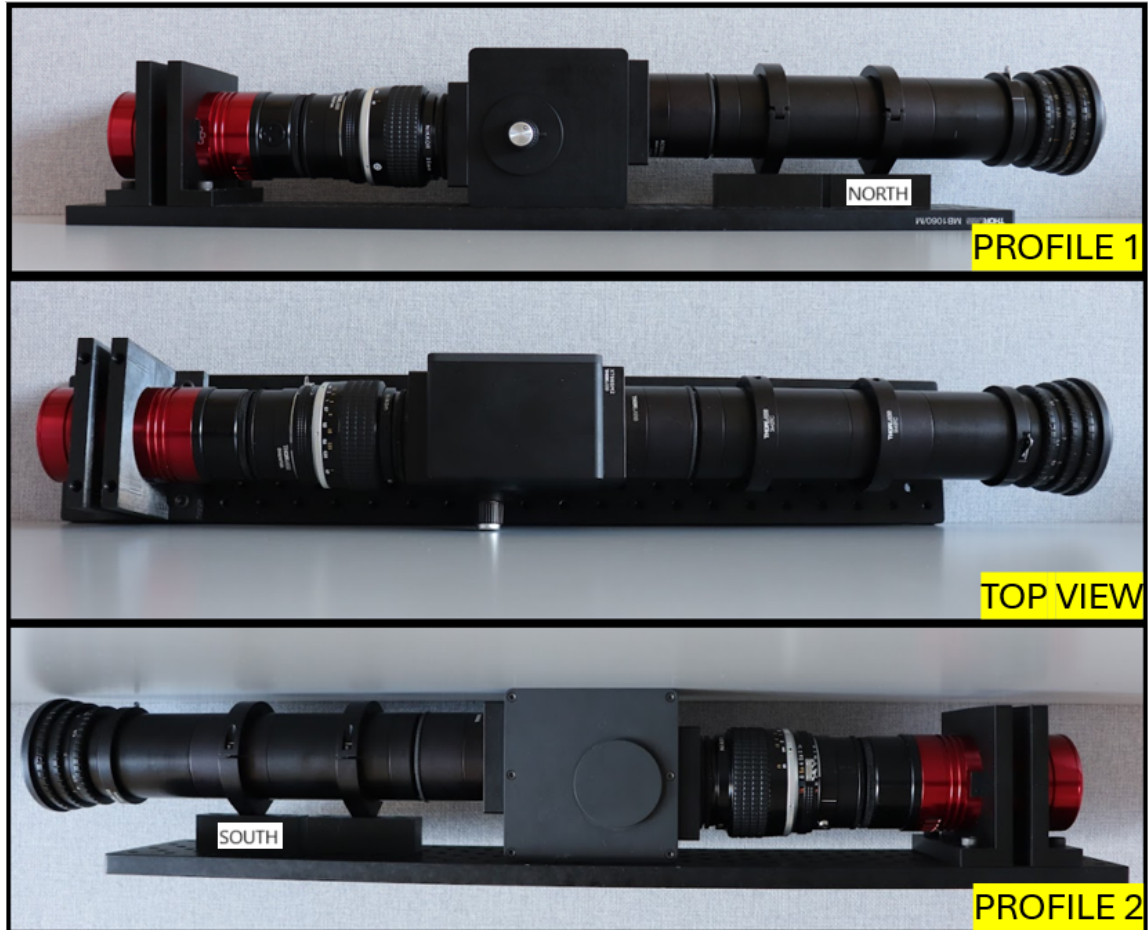


Figure 8.1: Views of MISS 2 mounted and fine-tuned (2024, UNIS)

**Appendix C, Calibration Certificate for Keo Alcor-RC
LBS s/n 10113)**



National Research Council
Canada

Measurement Science
and Standards

1200 Montreal Road, M-36
Ottawa, Canada
K1A 0R6

Conseil national de recherches
Canada

Science des mesures
et étalons

1200, chemin de Montréal, M-36
Ottawa, Canada
K1A 0R6

NRC - CNRC

NRC Calibration Report Number: PAR-2012-3049

Date of Issue: 2013-01-14

CALIBRATION REPORT

Spectral Radiance Calibration of Low Brightness Source Serial Number 10113

for

KEO SCIENTIFIC LTD.
1300 8th Street South West, Suite 404
Calgary, Alberta
Canada T2R 1B2

Attention: Dr. Trond S. Trondsen

Client order number: INMS Agreement

NRC order number: 503838

Metrologists:

Authorized by:

E. Côté, Technical Officer
Eric.Cote@nrc-cnrc.gc.ca

Dr. A.A. Gaertner, Project Leader
Arnold.Gaertner@nrc-cnrc.gc.ca
(613) 993-9344

Results in this report are traceable to the International System of Units (SI) through national measurement standards maintained at the National Research Council of Canada.

Results in this report relate only to the items being calibrated. Issuing of this report does not constitute an approval of the customer's products or procedures by the NRC.

Reports may be reproduced in whole without prior approval. However, this report may not be published in part without the written consent of the National Research Council of Canada.

© National Research Council Canada, 2013.

Les résultats dans ce rapport sont traçables au Système international d'unités (SI) par l'intermédiaire des étalons nationaux de mesure maintenus au Conseil national de recherches du Canada.

Les résultats contenus dans ce rapport ne se rapportent qu'aux objets étalonnés. L'émission de ce rapport ne signifie pas l'approbation des produits ou procédures du client par le CNRC.

Les rapports peuvent être reproduits en entier sans approbation préalable. Cependant, la reproduction de parties de ce rapport exige l'approbation écrite du Conseil national de recherches du Canada.

© Conseil national de recherches Canada, 2013.

1.0 Introduction

A Low Brightness Source (Keo Alcor-RC LBS s/n 10113) was received at NRC-M36 on 2012-November-06. The equipment was sent via FedEx Express from Devin Wyatt of KEO SCIENTIFIC LTD of Calgary, Alberta. Included in the packing box were the following items:

- i. Keo Alcor-RC LBS Lamp Controller s/n 10519
- ii. Agilent DC power supply model E3633A, s/n MY52160117
- iii. HP Pavilion Entertainment PC model dv7-2157ca, s/n CNF93315CD

The measurements and calibrations requested were

1. Spectral radiance (380 nm to 1068 nm at 4 nm intervals) of the front diffuser on the highest output level,
- ii. Horizontal uniformity scan of diffuser at the highest output level, using a smaller spot size than for item 1, and
- iii. Relative measurement of output levels for various aperture wheels.

The measurements and calibrations were carried out from 2012-December-05 to 2012-December-10.

The equipment was returned to Devin Wyatt via FedEx Ground on 2013-January-15.

2.0 Calibration Procedure

The spectral radiance measurements and calibrations were performed using a Photo-Research Model PR715 Spectroradiometer (s/n 75012201). The PR-715 was calibrated using the known spectral radiance of a pressed polytetrafluoroethylene (PTFE) diffuser illuminated by calibrated spectral irradiance source standards. The geometry used was $0^\circ/45^\circ$ (incidence/reflection). Two National Research Council spectral irradiance standards were used (FEL #91498 and #91499), each at three distances from the PTFE diffuser, to produce six different spectral radiance levels and corresponding PR-715 measurements for each of the four PR715 circular input apertures. Each PR-715 measurement was an average of three measurement integration cycles. The calibration of the PR-715 was performed on 2012-March-14 and 15 using PAR QMS procedure PAR-126v0.0.

The Keo Alcor-RC LBS was connected and operated as per KEO instructions. The Keo Alcor-RC LBS was mounted upon a transverse linear adjustment table to enable the horizontal uniformity scan of the output diffusing screen.

The spectral radiance at the LBS output diffusing screen, and normal to the plane of the output diffusing screen, of the Keo Alcor-RC LBS was measured using the PR-715. Each PR715 measurement is the average of three internal measurement cycles. The PR715 was used with the 1-degree input aperture for the measurements taken with spot sizes (diameters) of approximately 1 cm, 2 cm, 4 cm and 8 cm, centered on the LBS output diffusing screen. The LBS-to-PR715 spectroradiometer distance was adjusted to produce the different spot sizes measured at the Keo Alcor-RC LBS output diffusing screen.

The horizontal uniformity scan of the LBS output diffusing screen was performed with a spot size (diameter) of approximately 0.5 cm using the 0.5-degree input aperture on the PR715. The LBS was translated horizontally normal to the optical axis between the LBS and the PR715 for the different measurement points. Each

measurement is therefore a measurement of the spectral radiance normal to the LBS output diffusing screen, but at the different points horizontally across the face of the LBS output diffusing screen.

The measurement of the relative output levels for many of the LBS aperture positions was measured with an NRC photometer PRCKrochmann s/n 9602. The relative spectral response of the photometer is very nearly that of the CIE standard photometric observer for photopic vision. The input to the photometer was placed approximately 4.7 cm from the face of the LBS diffusing screen and centered upon the LBS diffusing screen. Consequently, these measurements will only weight the visible portion of the spectrum, and be only valid for the central area of the LBS output diffusing screen.

3.0 Results

All measurements were performed with the optical axis of the PR715 aligned normal to the face of the LBS output diffusing screen.

The spectral radiance of the LBS output diffusing screen was measured for spot sizes of 1 cm, 2 cm, 4 cm and 8 cm diameter, normal to the plane of the output diffusing screen and centered on the output diffusing screen. The LBS apertures were set to 3 of 3 and 12 of 12 for these measurements. The results are given in Table One and plotted in Figure One.

The results of the measurements of the spectral radiance from a 0.5-cm spot on the LBS at various positions horizontally across the vertical center of the LBS output diffusing screen are given in Figure Two for a representative set of wavelengths. The LBS apertures were set to 3 of 3 and 12 of 12 for these measurements. The horizontal positions are measured from the center of the LBS output diffusing screen, with positive positions to the right as viewed when looking at the front of the LBS as shown in Figure Three.

The results for the measurement of the relative output levels for the various LBS aperture positions are given in Table Two. Due to the low light output of the LBS, not all combinations of the two LBS apertures could be measured. The signal measured for each aperture combination was the average of 15 repeated measurements. The signals measured are all normalized to the signal for the largest aperture combination: the 12/12 with the 3/3.

This report (PAR-2012-3049.pdf) and data (PAR-2012-3049Data.xls) are also supplied on the accompanying CD.¹

4.0 Measurement Uncertainties

The measurement uncertainties for the calibration are a combination of the uncertainties in the calibration and use of the NRC PR715 spectroradiometer, and in the setting and use of the LBS. The estimated fractional standard deviations for the measurements are given in Table One. The column 'PR715 Calibration' is the estimated fractional standard deviation in the calibration of the PR715 for spectral radiance measurements. The column labeled 'Measurement of LBS' is derived from

¹ In case of differences between the electronic version and the printed version in this report, the official NRC report data will prevail.

the fractional standard deviation of the measurements performed upon the LBS: Each PR-715 measurement was an internal (to the PR715) average of three measurement integration cycles. Each measurement of the LBS included a set of three of these PR715 measurements. The column labeled 'Measurement of LBS' is an estimated standard deviation of these three sets of measurements. The column labeled 'Combined Quadrature Sum' is the square root of the sum of the squares of the estimated fractional standard deviations in the columns 'PR715 Calibration' and 'Measurement of LBS'.

The uncertainties given in Table Two for the measurements of the LBS apertures are the relative standard deviations of the 15 measurements made for each aperture combination. The larger uncertainties for the smaller apertures are due to the considerably smaller signals measured. Note, as indicated in Section 2 above, that the signals measured weight only the visible part of the spectrum, and were taken only from the central area of the LBS screen.

5.0 Traceability

- 5.1 The NRC values of spectral irradiance are traceable to the SI unit of spectral irradiance ($\text{watt}\cdot\text{cm}^{-2}\cdot\text{nm}^{-1}$) through several sources:
- (380 nm to 690 nm) an international comparison of spectral irradiance lamp standards, and
 - (700 nm to 1068 nm), through measurements using the NRC absolute radiometer (detector).

The NRC working standard lamps of spectral irradiance are calibrated from NRC primary standard lamps of spectral irradiance. The spectral irradiance of these primary lamp standards was determined by comparison with the lamps indicated in i) above, and by direct measurement in ii) using detectors that were calibrated using NRC room temperature absolute radiometers.

- 5.2 The nonfluorescent reflectance standard (diffuser) was pressed polytetrafluoroethylene (PTFE) powder ($1.0\pm 0.1 \text{ gm/cm}^3$) whose absolute spectral radiance factors, $\square_{45/0}(\square)$, from 380 nm to 1100 nm are traceable to the National Institute of Standards and Technology (NIST) with a relative uncertainty of 0.4% (95% confidence level).

Table One
Spectral Radiance of KEO Alcor-RC Low Brightness Source s/n 10113
Measured normal to the LBS screen from 4 different spot sizes.

LBS apertures at 3/3 and 12/12.

Unit of $W \cdot sr^{-1} \cdot m^{-2} \cdot nm^{-1}$

The uncertainty values are given as estimated relative standard (k=1) uncertainties.

Wavelength nm	Spectral Radiance $W \cdot sr^{-1} \cdot m^{-2} \cdot nm^{-1}$				Uncertainty		
	Spot diameter at center of LBS output screen				PR715 Calibration	Measurement of LBS	Combined Quadrature Sum
	1 cm	2 cm	4 cm	8 cm			
380.0	4.858E-07	4.122E-07	4.713E-07	4.431E-07	5.1%	55.8%	56.0%
384.0	5.964E-07	5.311E-07	6.322E-07	6.125E-07	4.4%	44.2%	44.4%
388.0	6.640E-07	6.293E-07	6.705E-07	6.748E-07	4.8%	31.2%	31.6%
392.0	7.167E-07	7.191E-07	7.735E-07	7.598E-07	3.3%	27.2%	27.4%
396.0	8.333E-07	8.065E-07	8.971E-07	8.301E-07	2.9%	16.7%	17.0%
400.0	9.429E-07	9.367E-07	9.550E-07	9.136E-07	2.9%	13.0%	13.4%
404.0	1.026E-06	1.037E-06	1.080E-06	1.018E-06	2.6%	12.9%	13.2%
408.0	1.148E-06	1.166E-06	1.143E-06	1.067E-06	2.4%	9.8%	10.1%
412.0	1.263E-06	1.255E-06	1.213E-06	1.161E-06	2.3%	6.5%	6.9%
416.0	1.337E-06	1.374E-06	1.319E-06	1.270E-06	2.3%	5.3%	5.8%
420.0	1.423E-06	1.450E-06	1.414E-06	1.340E-06	2.2%	5.2%	5.6%
424.0	1.538E-06	1.546E-06	1.515E-06	1.450E-06	2.2%	3.9%	4.5%
428.0	1.649E-06	1.651E-06	1.627E-06	1.570E-06	2.3%	3.9%	4.5%
432.0	1.778E-06	1.765E-06	1.731E-06	1.671E-06	2.2%	3.0%	3.8%
436.0	1.881E-06	1.904E-06	1.876E-06	1.785E-06	2.2%	4.2%	4.8%
440.0	2.012E-06	2.005E-06	1.999E-06	1.908E-06	2.3%	3.1%	3.9%
444.0	2.163E-06	2.159E-06	2.136E-06	2.025E-06	2.2%	3.3%	4.0%
448.0	2.289E-06	2.302E-06	2.284E-06	2.173E-06	2.2%	3.6%	4.3%
452.0	2.448E-06	2.461E-06	2.441E-06	2.330E-06	2.2%	2.2%	3.1%
456.0	2.586E-06	2.607E-06	2.596E-06	2.456E-06	2.2%	2.4%	3.2%
460.0	2.744E-06	2.769E-06	2.755E-06	2.598E-06	2.1%	2.3%	3.1%
464.0	2.922E-06	2.916E-06	2.904E-06	2.752E-06	2.1%	2.6%	3.3%
468.0	3.095E-06	3.071E-06	3.060E-06	2.905E-06	2.1%	2.2%	3.0%
472.0	3.251E-06	3.201E-06	3.201E-06	3.051E-06	2.1%	2.7%	3.4%
476.0	3.405E-06	3.410E-06	3.371E-06	3.189E-06	1.9%	2.7%	3.4%
480.0	3.569E-06	3.578E-06	3.527E-06	3.366E-06	1.9%	2.5%	3.2%
484.0	3.750E-06	3.750E-06	3.702E-06	3.536E-06	1.9%	2.3%	3.0%
488.0	3.914E-06	3.923E-06	3.875E-06	3.711E-06	1.8%	2.1%	2.8%
492.0	4.093E-06	4.103E-06	4.065E-06	3.881E-06	1.8%	2.1%	2.8%
496.0	4.294E-06	4.284E-06	4.247E-06	4.048E-06	1.8%	1.8%	2.5%
500.0	4.495E-06	4.488E-06	4.453E-06	4.244E-06	1.8%	1.9%	2.7%
504.0	4.681E-06	4.697E-06	4.635E-06	4.426E-06	1.8%	1.8%	2.6%
508.0	4.867E-06	4.896E-06	4.849E-06	4.608E-06	1.8%	2.0%	2.7%
512.0	5.079E-06	5.096E-06	5.053E-06	4.800E-06	1.8%	1.5%	2.3%
516.0	5.275E-06	5.281E-06	5.240E-06	4.987E-06	1.8%	1.3%	2.3%
520.0	5.484E-06	5.489E-06	5.424E-06	5.169E-06	1.8%	1.1%	2.1%
524.0	5.691E-06	5.691E-06	5.634E-06	5.363E-06	1.9%	1.3%	2.2%
528.0	5.924E-06	5.921E-06	5.881E-06	5.572E-06	1.8%	1.3%	2.2%
532.0	6.129E-06	6.136E-06	6.086E-06	5.798E-06	1.8%	1.1%	2.1%
536.0	6.348E-06	6.365E-06	6.306E-06	6.005E-06	1.8%	1.3%	2.2%
540.0	6.588E-06	6.580E-06	6.527E-06	6.222E-06	1.9%	1.1%	2.2%
544.0	6.805E-06	6.804E-06	6.750E-06	6.419E-06	1.8%	1.2%	2.2%
548.0	7.027E-06	7.023E-06	6.960E-06	6.626E-06	1.8%	1.2%	2.2%
552.0	7.259E-06	7.268E-06	7.193E-06	6.856E-06	1.8%	1.2%	2.2%

Wavelength nm	Spectral Radiance $W \cdot sr^{-1} \cdot m^{-2} \cdot nm^{-1}$				Uncertainty		
	Spot diameter at center of LBS output screen				PR715 Calibration	Measurement of LBS	Combined Quadrature Sum
	1 cm	2 cm	4 cm	8 cm			
556.0	7.506E-06	7.509E-06	7.453E-06	7.095E-06	1.8%	1.3%	2.3%
560.0	7.772E-06	7.759E-06	7.701E-06	7.340E-06	1.9%	1.1%	2.2%
564.0	7.991E-06	8.005E-06	7.915E-06	7.548E-06	1.9%	1.1%	2.2%
568.0	8.255E-06	8.251E-06	8.181E-06	7.789E-06	1.8%	1.2%	2.2%
572.0	8.492E-06	8.474E-06	8.420E-06	8.011E-06	1.8%	1.4%	2.3%
576.0	8.720E-06	8.722E-06	8.638E-06	8.220E-06	1.8%	1.0%	2.1%
580.0	9.004E-06	8.994E-06	8.926E-06	8.500E-06	1.9%	1.1%	2.2%
584.0	9.288E-06	9.289E-06	9.212E-06	8.779E-06	1.9%	1.1%	2.2%
588.0	9.509E-06	9.531E-06	9.447E-06	8.984E-06	1.9%	1.5%	2.4%
592.0	9.753E-06	9.737E-06	9.682E-06	9.204E-06	1.8%	1.2%	2.2%
596.0	9.969E-06	9.978E-06	9.889E-06	9.401E-06	1.8%	1.2%	2.1%
600.0	1.026E-05	1.026E-05	1.015E-05	9.673E-06	1.8%	1.3%	2.2%
604.0	1.051E-05	1.050E-05	1.041E-05	9.901E-06	1.8%	1.3%	2.3%
608.0	1.076E-05	1.076E-05	1.068E-05	1.016E-05	1.8%	1.2%	2.2%
612.0	1.099E-05	1.101E-05	1.090E-05	1.039E-05	1.8%	1.3%	2.2%
616.0	1.120E-05	1.120E-05	1.110E-05	1.059E-05	1.8%	1.3%	2.2%
620.0	1.147E-05	1.145E-05	1.134E-05	1.081E-05	1.8%	1.4%	2.3%
624.0	1.169E-05	1.166E-05	1.158E-05	1.105E-05	1.8%	1.2%	2.2%
628.0	1.190E-05	1.189E-05	1.180E-05	1.125E-05	1.8%	1.4%	2.3%
632.0	1.218E-05	1.220E-05	1.209E-05	1.153E-05	1.8%	1.4%	2.2%
636.0	1.241E-05	1.243E-05	1.233E-05	1.176E-05	1.8%	1.7%	2.4%
640.0	1.264E-05	1.268E-05	1.254E-05	1.197E-05	1.8%	1.4%	2.3%
644.0	1.295E-05	1.293E-05	1.281E-05	1.221E-05	1.8%	1.2%	2.1%
648.0	1.317E-05	1.318E-05	1.304E-05	1.244E-05	1.8%	1.2%	2.1%
652.0	1.341E-05	1.343E-05	1.332E-05	1.268E-05	1.8%	1.3%	2.2%
656.0	1.369E-05	1.369E-05	1.360E-05	1.293E-05	1.8%	1.3%	2.2%
660.0	1.401E-05	1.396E-05	1.386E-05	1.321E-05	1.8%	1.5%	2.3%
664.0	1.428E-05	1.423E-05	1.408E-05	1.346E-05	1.8%	1.4%	2.3%
668.0	1.455E-05	1.455E-05	1.440E-05	1.375E-05	1.8%	1.3%	2.2%
672.0	1.485E-05	1.484E-05	1.475E-05	1.403E-05	1.8%	1.4%	2.3%
676.0	1.513E-05	1.511E-05	1.500E-05	1.426E-05	1.8%	1.2%	2.2%
680.0	1.529E-05	1.529E-05	1.517E-05	1.442E-05	1.8%	1.4%	2.3%
684.0	1.554E-05	1.555E-05	1.541E-05	1.465E-05	1.8%	1.3%	2.2%
688.0	1.583E-05	1.582E-05	1.568E-05	1.490E-05	1.8%	1.6%	2.4%
692.0	1.614E-05	1.608E-05	1.595E-05	1.517E-05	1.6%	1.4%	2.1%
696.0	1.648E-05	1.647E-05	1.630E-05	1.553E-05	1.3%	1.5%	2.0%
700.0	1.676E-05	1.677E-05	1.660E-05	1.582E-05	0.9%	1.2%	1.5%
704.0	1.704E-05	1.704E-05	1.690E-05	1.608E-05	1.0%	1.3%	1.6%
708.0	1.727E-05	1.725E-05	1.712E-05	1.628E-05	1.0%	1.2%	1.5%
712.0	1.755E-05	1.751E-05	1.742E-05	1.655E-05	0.9%	1.4%	1.7%
716.0	1.772E-05	1.774E-05	1.757E-05	1.673E-05	0.9%	1.4%	1.6%
720.0	1.799E-05	1.803E-05	1.786E-05	1.696E-05	0.9%	1.6%	1.8%
724.0	1.827E-05	1.826E-05	1.812E-05	1.721E-05	0.9%	1.4%	1.7%
728.0	1.854E-05	1.850E-05	1.835E-05	1.749E-05	0.9%	1.2%	1.5%
732.0	1.884E-05	1.878E-05	1.864E-05	1.776E-05	1.0%	1.2%	1.5%
736.0	1.915E-05	1.910E-05	1.894E-05	1.805E-05	1.0%	1.4%	1.7%
740.0	1.933E-05	1.930E-05	1.913E-05	1.823E-05	0.9%	1.3%	1.6%
744.0	1.960E-05	1.956E-05	1.940E-05	1.847E-05	1.0%	1.3%	1.6%
748.0	1.999E-05	1.990E-05	1.973E-05	1.874E-05	1.1%	1.5%	1.8%
752.0	2.011E-05	2.012E-05	1.988E-05	1.895E-05	1.0%	1.3%	1.6%
756.0	2.034E-05	2.030E-05	2.014E-05	1.917E-05	0.8%	1.3%	1.5%

Wavelength nm	Spectral Radiance $W \cdot sr^{-1} \cdot m^{-2} \cdot nm^{-1}$				Uncertainty		
	Spot diameter at center of LBS output screen				PR715 Calibration	Measurement of LBS	Combined Quadrature Sum
	1 cm	2 cm	4 cm	8 cm			
760.0	2.059E-05	2.052E-05	2.038E-05	1.939E-05	0.8%	1.2%	1.5%
764.0	2.081E-05	2.080E-05	2.063E-05	1.968E-05	0.9%	1.4%	1.7%
768.0	2.100E-05	2.102E-05	2.080E-05	1.981E-05	0.9%	1.5%	1.8%
772.0	2.121E-05	2.126E-05	2.103E-05	2.001E-05	0.9%	1.3%	1.6%
776.0	2.149E-05	2.152E-05	2.126E-05	2.025E-05	0.9%	1.3%	1.6%
780.0	2.164E-05	2.161E-05	2.143E-05	2.043E-05	0.9%	1.1%	1.4%
784.0	2.183E-05	2.180E-05	2.163E-05	2.060E-05	0.9%	1.2%	1.5%
788.0	2.204E-05	2.202E-05	2.182E-05	2.079E-05	0.9%	1.3%	1.6%
792.0	2.228E-05	2.218E-05	2.198E-05	2.096E-05	0.9%	1.5%	1.7%
796.0	2.239E-05	2.232E-05	2.211E-05	2.105E-05	1.0%	1.4%	1.7%
800.0	2.263E-05	2.253E-05	2.232E-05	2.127E-05	1.0%	1.3%	1.6%
804.0	2.286E-05	2.282E-05	2.260E-05	2.153E-05	0.8%	1.2%	1.5%
808.0	2.306E-05	2.306E-05	2.280E-05	2.171E-05	0.9%	1.4%	1.7%
812.0	2.328E-05	2.327E-05	2.303E-05	2.190E-05	0.9%	1.5%	1.7%
816.0	2.354E-05	2.351E-05	2.329E-05	2.214E-05	0.9%	1.5%	1.7%
820.0	2.373E-05	2.369E-05	2.344E-05	2.228E-05	0.9%	1.5%	1.8%
824.0	2.391E-05	2.392E-05	2.365E-05	2.249E-05	0.9%	1.6%	1.8%
828.0	2.414E-05	2.409E-05	2.382E-05	2.272E-05	0.9%	1.3%	1.6%
832.0	2.424E-05	2.423E-05	2.398E-05	2.282E-05	0.9%	1.3%	1.6%
836.0	2.453E-05	2.447E-05	2.424E-05	2.307E-05	0.8%	1.5%	1.7%
840.0	2.464E-05	2.462E-05	2.435E-05	2.319E-05	0.9%	1.5%	1.7%
844.0	2.492E-05	2.489E-05	2.460E-05	2.347E-05	0.9%	1.6%	1.8%
848.0	2.515E-05	2.506E-05	2.485E-05	2.362E-05	0.9%	1.5%	1.8%
852.0	2.524E-05	2.511E-05	2.487E-05	2.364E-05	1.0%	1.5%	1.8%
856.0	2.547E-05	2.535E-05	2.504E-05	2.385E-05	0.9%	1.8%	2.0%
860.0	2.566E-05	2.552E-05	2.522E-05	2.404E-05	0.9%	1.5%	1.8%
864.0	2.581E-05	2.575E-05	2.544E-05	2.421E-05	0.9%	1.6%	1.8%
868.0	2.605E-05	2.594E-05	2.568E-05	2.444E-05	0.9%	1.7%	1.9%
872.0	2.631E-05	2.625E-05	2.591E-05	2.459E-05	0.9%	1.6%	1.8%
876.0	2.654E-05	2.645E-05	2.611E-05	2.482E-05	0.9%	1.4%	1.7%
880.0	2.677E-05	2.667E-05	2.628E-05	2.503E-05	1.0%	1.6%	1.9%
884.0	2.686E-05	2.685E-05	2.648E-05	2.513E-05	0.9%	1.6%	1.8%
888.0	2.727E-05	2.718E-05	2.673E-05	2.538E-05	1.0%	1.7%	1.9%
892.0	2.732E-05	2.729E-05	2.676E-05	2.548E-05	0.9%	2.0%	2.2%
896.0	2.757E-05	2.744E-05	2.698E-05	2.566E-05	0.9%	1.6%	1.8%
900.0	2.784E-05	2.763E-05	2.722E-05	2.585E-05	0.9%	1.6%	1.8%
904.0	2.806E-05	2.782E-05	2.739E-05	2.597E-05	0.9%	2.1%	2.3%
908.0	2.827E-05	2.796E-05	2.753E-05	2.611E-05	0.9%	2.2%	2.4%
912.0	2.842E-05	2.820E-05	2.771E-05	2.636E-05	0.9%	1.9%	2.1%
916.0	2.860E-05	2.848E-05	2.792E-05	2.646E-05	0.9%	2.3%	2.4%
920.0	2.896E-05	2.871E-05	2.818E-05	2.675E-05	0.9%	2.3%	2.5%
924.0	2.921E-05	2.892E-05	2.823E-05	2.696E-05	1.0%	2.4%	2.6%
928.0	2.938E-05	2.912E-05	2.840E-05	2.709E-05	1.1%	2.3%	2.5%
932.0	2.935E-05	2.913E-05	2.862E-05	2.715E-05	1.0%	3.6%	3.7%
936.0	2.982E-05	2.927E-05	2.875E-05	2.709E-05	1.0%	2.0%	2.2%
940.0	3.015E-05	2.961E-05	2.899E-05	2.740E-05	1.0%	2.1%	2.3%
944.0	3.026E-05	2.993E-05	2.917E-05	2.751E-05	0.9%	2.2%	2.4%
948.0	3.058E-05	3.016E-05	2.935E-05	2.765E-05	1.0%	2.1%	2.3%
952.0	3.086E-05	3.022E-05	2.958E-05	2.790E-05	0.9%	2.4%	2.6%
956.0	3.076E-05	2.995E-05	2.947E-05	2.790E-05	1.1%	2.2%	2.5%
960.0	3.085E-05	3.050E-05	2.976E-05	2.797E-05	1.0%	3.1%	3.3%

Wavelength nm	Spectral Radiance $W \cdot sr^{-1} \cdot m^{-2} \cdot nm^{-1}$				Uncertainty		
	Spot diameter at center of LBS output screen				PR715 Calibration	Measurement of LBS	Combined Quadrature Sum
	1 cm	2 cm	4 cm	8 cm			
964.0	3.101E-05	3.055E-05	2.961E-05	2.810E-05	1.0%	3.3%	3.5%
968.0	3.163E-05	3.107E-05	2.994E-05	2.848E-05	1.1%	3.4%	3.6%
972.0	3.192E-05	3.115E-05	2.998E-05	2.842E-05	1.0%	3.6%	3.8%
976.0	3.196E-05	3.137E-05	2.987E-05	2.823E-05	1.1%	4.0%	4.2%
980.0	3.199E-05	3.094E-05	2.988E-05	2.809E-05	1.1%	4.1%	4.2%
984.0	3.245E-05	3.146E-05	3.023E-05	2.844E-05	1.2%	3.3%	3.5%
988.0	3.271E-05	3.149E-05	3.012E-05	2.871E-05	1.3%	2.6%	2.9%
992.0	3.290E-05	3.147E-05	3.052E-05	2.892E-05	1.3%	3.7%	3.9%
996.0	3.301E-05	3.156E-05	3.015E-05	2.881E-05	1.4%	5.8%	5.9%
1000.0	3.329E-05	3.206E-05	3.042E-05	2.961E-05	1.4%	6.1%	6.2%
1004.0	3.323E-05	3.216E-05	3.059E-05	2.900E-05	1.7%	4.3%	4.7%
1008.0	3.393E-05	3.212E-05	3.100E-05	2.919E-05	1.6%	4.3%	4.6%
1012.0	3.356E-05	3.221E-05	3.045E-05	2.891E-05	1.7%	5.1%	5.4%
1016.0	3.406E-05	3.233E-05	3.063E-05	2.920E-05	1.6%	6.8%	7.0%
1020.0	3.354E-05	3.246E-05	3.079E-05	2.909E-05	1.8%	6.9%	7.2%
1024.0	3.345E-05	3.175E-05	3.030E-05	2.839E-05	2.2%	5.0%	5.5%
1028.0	3.372E-05	3.225E-05	3.041E-05	2.756E-05	2.1%	9.1%	9.3%
1032.0	3.316E-05	3.189E-05	3.033E-05	2.731E-05	1.9%	11.2%	11.4%
1036.0	3.354E-05	3.241E-05	3.102E-05	2.788E-05	2.1%	10.9%	11.1%
1040.0	3.368E-05	3.166E-05	3.035E-05	2.757E-05	2.4%	8.4%	8.7%
1044.0	3.410E-05	3.121E-05	3.047E-05	2.799E-05	2.3%	10.1%	10.4%
1048.0	3.278E-05	3.118E-05	2.944E-05	2.664E-05	2.8%	13.2%	13.5%
1052.0	3.387E-05	3.315E-05	3.030E-05	2.803E-05	3.3%	13.2%	13.6%
1056.0	3.308E-05	2.930E-05	2.850E-05	2.619E-05	2.8%	16.0%	16.2%
1060.0	3.115E-05	2.864E-05	2.631E-05	2.521E-05	7.0%	14.5%	16.2%
1064.0	3.355E-05	3.074E-05	2.662E-05	2.644E-05	4.3%	17.6%	18.1%
1068.0	3.408E-05	3.050E-05	2.700E-05	2.696E-05	4.0%	18.7%	19.1%

Figure One
 Spectral Radiance of KEO Alcor-RC Low Brightness Source s/n 10113
 Measured normal to the LBS screen from 4 different spot sizes.
 LBS apertures at 3/3 and 12/12.
 Unit of $W \cdot sr^{-1} \cdot m^{-2} \cdot nm^{-1}$

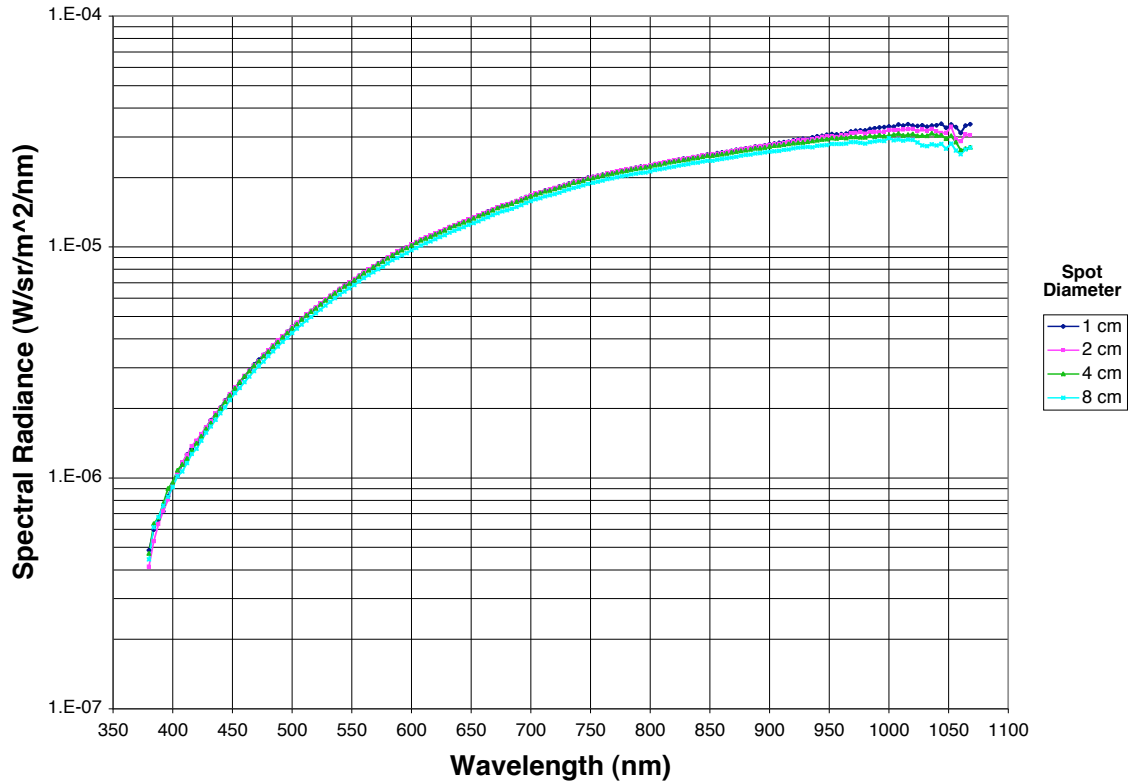


Figure Two
 Spectral Radiance of KEO Alcor-RC Low Brightness Source s/n 10113
 Measured normal to the LBS screen from 0.5-cm diameter spot
 LBS apertures at 3/3 and 12/12.
 Unit of $W \cdot sr^{-1} \cdot m^{-2} \cdot nm^{-1}$
 Position origin is the center of the LBS output diffusing screen

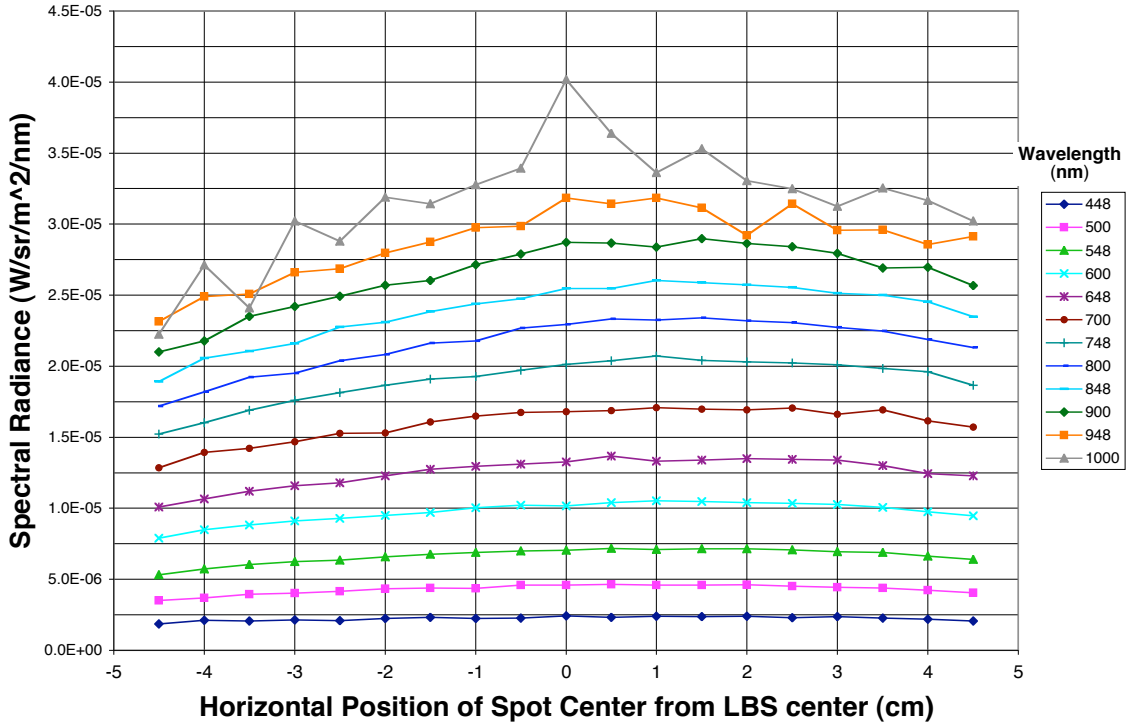


Figure Three
 Geometry for Horizontal Uniformity Measurements of Figure Two

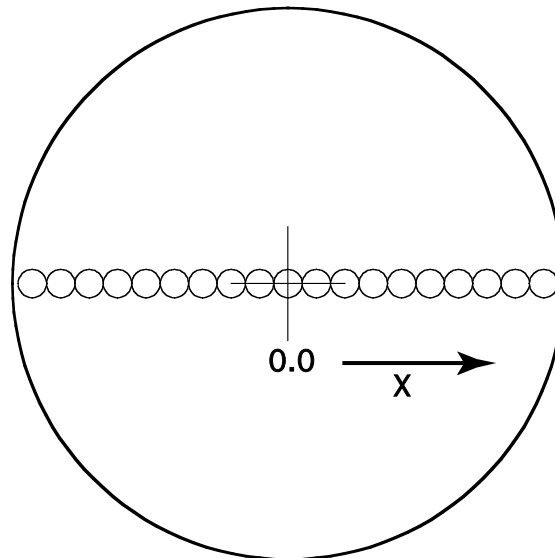


Table Two

Signal ratios for KEO Alcor-RC Low Brightness Source s/n 10113 Apertures.
 Measured normal to the LBS at the center of the LBS output diffusing screen.
 The uncertainty values are given as estimated relative standard (k=1) uncertainties.

Aperture x/12	Aperture 3/3		Aperture 2/3		Aperture 1/3	
	Ratio	Uncertainty	Ratio	Uncertainty	Ratio	Uncertainty
12	1.00	0.00%	1.91E-01	0.01%	2.05E-02	0.02%
11	5.09E-01	0.01%	1.01E-01	0.01%	1.08E-02	0.08%
10	2.59E-01	0.01%	5.24E-02	0.05%	5.66E-03	0.15%
9	1.30E-01	0.01%	2.67E-02	0.06%	2.84E-03	0.27%
8	6.62E-02	0.01%	1.36E-02	0.07%	1.43E-03	0.35%
7	3.26E-02	0.02%	6.74E-03	0.21%	6.21E-04	5.42%
6	1.70E-02	0.04%	3.53E-03	0.22%	3.70E-04	1.26%
5	8.48E-03	0.12%	1.76E-03	0.51%	2.51E-04	1.29%
4	4.60E-03	0.48%	9.30E-04	1.08%	9.90E-05	8.44%
3	1.88E-03	0.34%	4.08E-04	2.71%	1.27E-05	39.16%
2	8.97E-04	0.65%	1.91E-04	3.17%		